TRANSPORT AND WORKS ACT 1992

TRANSPORT AND WORKS (INQUIRIES PROCEDURES) RULES 2004

NETWORK RAIL (CAMBRIDGE SOUTH INFRASTRUCTURE ENHANCEMENTS) ORDER

MAIN PROOF OF EVIDENCE ON MATTERS OF RESEARCH AND THE UNIVERSITY

KARL WILSON ON BEHALF OF THE UNIVERSITY OF CAMBRIDGE

Inquiry Document Reference	**[TBC]/OBJ8**
Author	**Karl Wilson**
Date	**6 January 2022**

Contents

1 QUALIFICATION AND EXPERIENCE

1.1 I am Karl Wilson. I have a BA (Hons) in Business with Law from the University of Brighton (2003) and I am qualified as an accountant. I am a Fellow of the Association of Certified Chartered Accountants.

1.2 On qualification I was employed by the University of Cambridge ("**University**") as an accountant and in 2007 I helped to author national guidance (RCUK) on costs recovery in relation to animal research programmes. In 2009, I was employed as an Operations Manager responsible for the administration of the University's biomedical support services department.

1.3 In 2014 I was part of the team responsible for the design and development of the Anne McLaren Building ("**AMB**") as part of the University's restructuring programme.

1.4 In 2016, the University finalised the restructuring of its research operations following an external governance review and I became Operations Director for a new combined department known as University Biomedical Services. Since then, I have remained in this position. From 2021 I have also provided external consultancy services in relation to building and facility design.

1.5 I am based full time at the AMB and am primarily responsible for leading the operations there to further the work of the University's biomedical and clinical medicine departments. These departments support over 1000 individual license holders, 200 project licence holders and 180 direct staff. I am responsible for day-to-day compliance with the requirements of the Home Office establishment license for the AMB.

2 INTRODUCTION

2.1 The purpose of my evidence is twofold.

2.2 First, I describe the research and imaging work undertaken within the AMB and its importance, both to the University and globally.

2.3 Secondly, I explain the significant concerns held by the University about the potential effect of the proposed scheme ("**Scheme**") pursuant to the Network Rail (Cambridge South Infrastructure Enhancements) Order ("**Order**") on that work, which in my view Network Rail has not sufficiently understood when applying for the Order. Much of the work in the AMB has the potential to be affected by noise and vibration. These effects could cause inaccuracies or inconsistencies of results, damaging, potentially years of research and incurring significant financial and reputational loss to the University.

2.4 My evidence is to be read with the other expert evidence submitted by the University, in particular that relating to noise and vibration, prepared by Rupert Thornely-Taylor.

2.5 The land interests of the University in the Cambridge Biomedical Campus ("**CBC**") are addressed in the evidence of Paul Milliner. I do not repeat that detail here but focus on the AMB in particular.

3 THE UNIVERSITY AND THE IMPORTANCE OF THE CBC AND THE AMB

The University and the CBC

3.1 The University has been at the heart of Cambridge for generations. Having been founded in 1209, it is the second oldest university in the English-speaking world and one of the most prestigious academic institutions in the world. The University's core activities are world class academic teaching and research and its ability to provide an environment in which these activities can successfully flourish is a vital component of its historical and ongoing success. The Life Sciences Department, including the School of Clinical Medicine, is one of the UK's leading faculties.

3.2 Cambridge is a top-ranked Russell Group University and was globally ranked 3rd in the recently published 2022 QS World University Rankings. The 2020 Research Excellence Framework results place 99% of the University's research activity to be "world leading", "internationally excellent" or "internationally recognised", with the University being recognised as excellent in disciplines which span the full range of research. In the 2014 Research Excellence Framework Review, Cambridge was ranked second in the country for clinical medicine.

3.3 The CBC is the largest centre of medical research and health science in Europe. Locating world-leading academic and industry scientists on the same site as the teaching hospitals of the University creates the optimum environment for the rapid and effective translation of research into routine clinical practice.

3.4 The School of Clinical Medicine is housed in multiple buildings across the CBC. The School comprises twelve academic departments, four research institutes and five Medical Research Council units: the Medical Research Council Laboratory of Molecular Biology; Cancer Research UK; the Cambridge Institute; the Heart and Lung Research Institute; and Addenbrooke's Centre for Clinical Investigation.

3.5 In addition, the CBC accommodates the University's School of Biomedical Science, various NHS and education facilities and centres and global biomedical and pharmaceutical companies such as Astra Zeneca and ABCAM.

3.6 The School of Clinical Medicine aspires to change the practice of medicine and improve biological understanding in a wide range of clinical specialties and scientific disciplines. Collaborative research, both within biomedicine and crossing the boundaries to the mathematical, physical and social sciences, is key to our approach.

The School also supports key enabling technologies and facilities in imaging, bioinformatics and biological systems. There are very few facilities worldwide which offer this range and quality of work and facilities. The main areas of research interest are:

- Cancer Research
- Cardio-Respiratory Medicine
- Cellular mechanisms of disease
- Diabetes, Endocrinology and Metabolism
- Epidemiology, Public Health and Primary Care
- Genetics and Genetic Medicine
- Haematological and Transplantation Medicine
- Infection and Immunity
- Neurosciences and Mental Health
- Stem Cells and Regenerative Medicine

3.7 All of these areas are supported by the work in the AMB.

The AMB and its Importance

3.8 The AMB was named after Dame Anne McLaren, who was one of the world's leading specialists in reproductive medicine. The AMB was built to replace three other research facilities used by the School in order to provide a modern, world class facility to promote the expertise of the University in biomedicine.

3.9 The biomedical research facility at the AMB represents a major investment in UK scientific research and is a one-of-a-kind facility within the CBC. The AMB was opened in October 2019 as a new biomedical research facility to help further our understanding of how diseases occur and in the development of new treatments for conditions including cancer, dementia and diabetes. It supports globally important research activities across the CBC, including pioneering research into Covid-19. This includes: the use of imaging equipment to test the flow of dyes that is then adopted for

wider imaging purposes in medical treatment (including nuclear medicine); the modelling of disease including through the use of genetic modification to develop cures; and the replication of organs in vitro to aid drug development and organ replacement technology.

3.10 Scoping for the AMB started in 2011 when the University undertook an extensive review of its biomedical research strategies and requirements. A recommendation of that review was for a single new biomedical research facility to be built on the CBC, funded by University endowment, replacing three aging sites that would support the CBC and key university departments from across Cambridge. A further four years of design and planning was then undertaken before work began through archaeological investigations which started on site August 2016. I explain the design of the AMB further below. The AMB facility is rare. Neither the University, nor wider operators within the University's Estate, have access to an equivalent facility should the AMB be unable to operate within its core design parameters.

3.11 University researchers at the AMB use Magnetic Resonance Imaging ("**MRI**") equipment for testing disease treatments, and to acquire sub-millimetre images in lab specimen and animals. The University's research studies include imaging abdominal and brain cancers, brain aneurysms, thrombectomies (an innovative surgical procedure used to remove blood clots from arteries and veins); human cadaveric specimens, and cardiac and respiratory diseases. Work is performed with the University and Addenbrooke's Hospital researchers and with pharmaceutical companies, including AstraZeneca. High resolution imaging with limited noise and vibration interruptions are vital to ensure that these studies run efficiently and with limited disruptions to ensure the highest clinical impact.

3.12 As is common in biomedicine, research at the AMB involves the use of rodents (mice and, to a lesser extent, rats) ("**rodents**") and fish. This necessitates a Home Office licence ("**Licence**") to be held to which Establishment Licence Conditions attach. I explain this further below. The Licence conditions require, but in any event the University and other occupiers of the AMB aim to meet, the highest standards of animal welfare, underpinned by the principles of the "**3Rs**" of animal research (Reduction, Refinement & Replacement).

3.13 Imaging work takes place predominantly on floor 0 of the AMB, with some additional imaging work on floor 2. Research involving the use of rodents takes place on floors 0, 2 & 4. Research involving the use of fish takes place on floor 0. There is a specialist

breeding facility on floor 4 with highly protected access to ensure the high health status ("specified opportunist pathogen free" or "SOPF") of the rodents on that floor. In total, the AMB houses over 25,000 rodents (excluding the animal research use of Astra Zeneca, who occupy part of floor 2) and several thousand fish. Photographs showing examples of the operations within the AMB are included at **Appendix 1.**

3.14 Whilst delays due to COVID-19 mean that the AMB is still currently expanding its operational capacity, the AMB is nonetheless currently hosting 119 individual research grants (it has hosted others to date). The AMB recovers circa £3m of grant funding directly from researchers in receipt of grant funding, but its work overall supports a total of circa £41.5m per annum of research grants. In 2020/2021 these grants overall accounted for £34.8m relating to research activity in the School of Clinical Medicine (12% of that activity) and £6.7m relating to the School of Biological Sciences (5.5% of that activity). The individual research grants are used by the holders of project licenses to meet the costs of receiving services and occupying research space within the AMB. Services provided within the AMB include a range of important services relating to animal welfare and the carrying out of scientific procedures to support research work.

3.15 This research is funded from a host of sources including charities, government, UK Research and Innovation (UKRI), the EU and industry. The grants themselves will fund PhD students, post-doctoral research and a host of other researchers at various stages of their careers. Other than the 80+ staff who work permanently in the building over 650 researchers and support staff have daily access.

3.16 The AMB itself provides unique service and support space not found anywhere else within the CBC. Because of the highly regulated nature of these spaces, they have to be designated with specific environmental conditions so are not easily created or replicated. This means that the AMB researchers, from both the University and collaborative partners, use it as a specialist hub, whilst maintaining their own labs elsewhere on the CBC, often taking samples and work back and forth in support of a range of academic research goals. This supports the University's aim to translate research and clinical excellence into practical human health benefits, such as new therapeutics, devices, diagnostics or other interventions.[1] Examples of recent papers

[1] Examples of recent papers and publications from the types of work carried out in the building include: M. Zaeem Cader et al *"FAMIN Is a Multifunctional Purine Enzyme Enabling the Purine Nucleotide Cycle*". Cell: Volume 180, Issue 2, 23 January 2020, Pages 278-295.e23 and Galvin et al "*The human and mouse islet peptidome: effects of obesity and type 2 diabetes, and assessment of intra-islet production of glucagon-like peptide-*1", *J. Proteome Res. 2021, 20, 4507−4517 (**see Appendix 2**)*

and publications from the types of work carried out in the AMB are included at **Appendix 2**.

3.17 Given the breadth of research activities and the specialist nature of the work undertaken, the AMB has specialist working requirements in respect of environmental laboratory conditions, with an extremely narrow tolerance range beyond which research outcomes would be rendered unreliable. I explain the design of the AMB below after providing further details on the Licence.

4 HOME OFFICE LICENCE

4.1 All regulated work in the AMB is performed under the requirements of the Animals (Scientific Procedures) Act 1986 (as amended[2]) ("**ASPA**"), pursuant to the issue of an Establishment Licence by the Secretary of State[3].

4.2 Under ASPA, the Secretary of State is required to issue codes of practice as to the care of protected animals and their use for regulated procedures under an Establishment Licence[4]. The "Code of Practice for the Housing and Care of Animals Bred, Supplied or Used for Scientific Purposes 2014" ("**Code of Practice**") was issued under section 21 of ASPA and applies to the work at the AMB since it is an establishment licensed for using animals under section 2C of ASPA. As such, the AMB must abide by the mandatory standards within Sections 1 and 2 of the Code of Practice for all species held at the AMB that will be, are being or have been used for a licensed purpose. Section 3 to the Code of Practice also provides advice in areas that are not covered in Sections 1 or 2, advice for protected species absent from those sections and additional information about how Section 1 or 2 standards of the Code of Practice might be met.

4.3 The purpose of the Code of Practice is "*to ensure that the design, construction and function of the installations and equipment of licensed establishments – along with their staffing, care and practices – allow procedures to be carried out as effectively as possible in order to obtain reliable results using the minimum number of animals and causing the minimum degree of pain, suffering, distress or lasting harm*"[5].

4.4 Section 1 and 2 of the Code of Practice is used to assess whether the care and accommodation provided by an establishment carrying on regulated activities meet the requirements of ASPA and standard condition 4 of its Establishment Licence. Failure to meet the legal minimum standards set out in Sections 1 and 2 is likely to result in non-compliance action being taken.

4.5 The key outcomes driven by the Code of Practice are:

4.5.1 to promote good animal welfare through the provision of consistent, high quality care and accommodation;

---

[2] By the Animals (Scientific Procedures) Act 1986 Amendment Regulations 2012.

[3] See section 6 of ASPA.

[4] See section 21 of ASPA.

[5] See para 2 of the Code of Practice, page 3

4.5.2 to support the generation of high quality, reliable scientific results through the reduction of environmental variables;

4.5.3 to implement the principles of the 3Rs through using the minimum number of animals and causing the minimum degree of pain, suffering, distress or lasting harm.

4.6 The advice given in Section 3 of the Code of Practice is based on Commission Recommendation 2007/526/EC[6] adapted to ensure the information provided is appropriate (specific and clear) in the context of the UK. Section 3 encourages licensed establishments such as the AMB to continually improve their standards of care and accommodation in line with the principles of the '3Rs', striving to achieve better welfare outcomes where practicable and applicable. Section 3 Chapter 1 states for all animals that:

"Noise can be a disturbing factor for animals. High noise levels and sudden noises can cause stress which, in addition to the welfare consequences for the animal, may influence experimental data….Due consideration should be given to controlling noise levels within the hearing ranges of animals, including in some cases ultrasound (sound above the hearing range of the human being, conventionally taken to be sounds exceeding 20 kHz), particularly during their resting phase"[7];

"Animals such as rodents, amphibians and fish are very sensitive to vibration. Vibration can have a negative effect on reproductive efficiency and can have an influence on experimental results. It is therefore important to minimise vibration in the animal facility"[8].

"Vibration is more likely to be an issue in animal facilities located in an upper level of a building rather than at ground level because of structural considerations. However, animals in ground floor and basement facilities may be affected by vibration arising from major structural project"[9].

4.7 Specifically for fish Section 3 Chapter 10 states as follows:

[6] Itself based on Appendix A to the European Convention for the protection of vertebrate animals used for experimental and other scientific purposes.

[7] See paragraph 2.6 of Section 3, Chapter 1 of the Code of Practice

[8] See paragraph 2.7 of Section 3, Chapter 1 of the Code of Practice

[9] See paragraph 2.7 of Section 3, Chapter 1 of the Code of Practice

"Fish can be acutely sensitive to sounds and vibrations, even at very low levels. Fish reared in a particular environment will adapt to the stimuli presented there and may become stressed if moved to unfamiliar surroundings. It is advisable to take reasonable steps to avoid sudden noise and vibration. It is advisable to situate plant in a separate room to tanks wherever possible."[10]

4.8 The University's responsibility as a licence holder is extremely important to it and the University is required to put the health of the animals at the forefront of what it does. We place good welfare at the centre of all our animal research and aim to meet the highest standards: good animal welfare and good science go hand-in-hand. We take the position that compliance with the law and associated Code of Practice relating to animal welfare is the minimum operating standard. The extracts from the Code of Practice set out above demonstrate the potential issues that are recognised to occur in relation to noise and vibration in particular and confirm the general requirement for facilities to be designed and operated in a manner which creates a suitable environment for species to be kept, having regard to their physiological and ethological needs.

4.9 It therefore followed that the University considered noise and vibration very carefully when designing the AMB. I explain this further below.

[10] See paragraph 2.5 of Section 3, Chapter 10 of the Code of Practice

5 THE DESIGN OF THE AMB

Introduction

5.1 The AMB was designed as a Home Office secure facility, with fixed vibration criteria as part of the embedded design built to withstand vibration impact from the existing operational railway. Although there was no formal regulatory criterion of acceptable noise and vibration, the University took into account the broader regulatory framework outlined above looked at what others recommended as good practice, as well as our own experience.

5.2 This included our experience from the three facilities we were closing on the CBC which were operating at a vibration criterion known as VC-A (see the evidence of Rupert Thornely-Taylor for an explanation of vibration). From this we knew there was a good record of breeding and animal welfare. It also meant that if this level of operation could be matched that it would avoid or minimise the potential for this to operate as a harmful variable for the research work being carried on.

5.3 In addition, the US National Institutes of Health Design Requirements Manual (2016) sets out vibration limits (Table 5.2.2) for animal research as follows: animal research facility: 100 μm/s; rodent behavioural and holding rooms 50 μm/s (see again the evidence of Rupert Thornely-Taylor for an explanation of vibration).

5.4 In March 2014 Ramboll were appointed to carry out an initial assessment of the ambient vibration characteristics for the planned site for the AMB to confirm our intended criteria could be met, despite the proximity to the railway.

5.5 Two principal criteria were set in the design: 50μm/s for sensitive areas on levels 0, 2 and 4 (interpreted as similar to VC-A, but with a constant vibration limit of 50μm/s between 1 and 80Hz).

5.6 For the MRI installation we adopted a building design specification, prior to the selection of specific equipment of VC-C, based upon our adoption of guidance contained in the American Society for Heating, Refrigeration and Airconditioning Engineers HVAC application handbook.

5.7 The expected vibration levels of the building were checked twice more, once in 2015 and again in 2016 against the planned construction methodology. At all times adherence to VC-A (and VC-C where relevant) was expected.

5.8 Ramboll were then appointed in November 2017 to carry out a vibration survey at the under-construction building to validate the vibration performance of the building in relation to the design performance criteria. The outcome of that work, in so far as is relevant, can be summarised as follows:

5.8.1 The VC-C criterion for the MRI room was exceeded occasionally for 1s Root Mean Squared Amplitude ("**RMS**") levels (see further explanation in the evidence of Rupert Thornely-Taylor). Over the measurement period, only 6 such exceedances were observed. These were isolated events of relative short duration, during the night, with peaks lasting only a second in some cases. This did not cause concern at the time given that MRI equipment was not to be used during the night. Typically, vibration levels were below VC-C.

5.8.2 Vibration levels in the building generally tended to be lower than was measured externally. At all locations, the vibration magnitudes were lower than VC-B. This means that the (less demanding) VC-A criterion was achieved with some margin.

Table 1: Summary of measured vibration level

Metric	Measurement location			
	External	Level 0	Level 2	Level 4
Maximum 1s RMS	Vertical direction VC-C typically Horizontal direction Worst: VC-A Typical: VC-B	VC-B at all locations. This achieves the VC-A criterion at locations 1 and 2, but exceeds the VC-C criterion at location 3 in a small number of cases.	VC-B at all locations	VC-B at all locations
99.9th percentile 1s RMS	VC-D typically in all directions	VC-E at two locations typically and VC-D at the other. Marginal exceedances of both criteria occur at some isolated frequencies.	VC-D at two locations and VC-E at the other	N/A
1hour Average RMS	VC-E in all directions	VC-F at all locations	VC-F at all locations	VC-F at all locations typically

5.9 A final report was commissioned in February 2019 as part of the handover when the building plant was running to ensure we had not exceeded the criteria. The survey results showed levels below the maximum permissible limits in all cases.

5.10 The MRI equipment that was installed in the building, once operational, has manufacturer's stated limits (again, see the evidence of Rupert Thornely-Taylor). In summary these require operations at no more than a RMS (1 second) value of 12.5 μm/s in any third octave band centred on frequencies between 1Hz and 20kHz.

5.11 I have dealt so far with the issues of noise and vibration when designing the AMB. A survey was also carried out to determine the existing electromagnetic environment on what were then known as Plots 8 and 9, with Plot 8 eventually accommodating the AMB. In general, field levels were recorded at below general public health and technological requirements. The recommendation in the survey was that the survey results should be compared with any specific requirements of the use of the building. It was reported, for example, that magnetic field values found at the site could be incompatible with sensitive laboratory equipment, such as MRI scanners. Following installation of the MRI equipment within the AMB, during commissioning and initial operations there have been no concerns relating to the performance of the equipment. So far, the published requirements for the MRI are well within the levels measured in the initial survey and its suitability has been confirmed. Appropriate assessments and monitoring will need to take place for any equipment procured in future.

6 IMPACTS OF THE SCHEME ON THE AMB AND RESEARCH

Introduction

6.1 As set out above, the research undertaken within the AMB requires specialist working requirements and laboratory conditions in respect of both the sensitivity of equipment being used and the sensitivity of animal receptors within the AMB (comprising rodents and fish).

6.2 My concerns raised by the noise and vibration effects of the proposed Scheme on the AMB break down into three main categories:

6.2.1 effects of noise and vibration on highly sensitive research equipment;

6.2.2 effects of noise and vibration on animal welfare where rodents and fish are used; and

6.2.3 effects of noise and vibration on research outputs where rodents and fish are used.

6.3 I have significant concerns with the extent to which the proposals, including the supporting material in the Environmental Statement prepared for the Scheme ("**ES**") have attempted to properly understand the specialised nature of the important work carried on within the AMB in these respects. I explain these below, along with their potential implications, drawing on the background that I set out above. I also have concerns regarding electromagnetic interference ("**EMI**") in relation to imaging equipment however this will be addressed separately in evidence prepared by John McAuley.

Effects of noise and vibration on highly sensitive equipment

6.4 The AMB houses (across five experimental zones) many high tech and industry leading pieces of specialised equipment which require specialist working environments. It operates 24 hours a day, 365 days a year, and is highly sensitive to both external noise and vibration factors. High-resolution imaging equipment is acutely sensitive to vibration and noise. This includes several pieces of extremely valuable and specialist equipment, including a circa £1m "3T MRI" machine and two Two-Photon Microscopes.

6.5 MRI equipment in the AMB is in high demand and is used by researchers at the University throughout the week and, although the equipment is not currently used on the weekend, increasing demand may be such that use may need to extend into weekends in future. Scanning sessions take several hours at a time.

6.6 As explained by Rupert Thornely-Taylor, adherence to specified vibration criteria is imperative for the successful use of MRI and other imaging equipment housed within the AMB, alongside providing for stable laboratory conditions. The AMB has been designed to accommodate normal use of the building and the railway in its current operation (i.e. trains passing by between Cambridge Central Station and the signals before Shelford Branch points where the line splits to either Kings Cross or Liverpool Street). It did not anticipate the effects of any major construction activity or trains / passengers at a station in close proximity to the AMB beyond the existing operational railway line.

6.7 The major concern of the University is the potential for further construction activity or operational effects of railway-associated development to affect this work.

6.8 Increased ground vibrations risk causing image artefacts (i.e. abnormalities in the images) which in turn would render certain vital pieces of research useless. It is critical that this is avoided in order for ongoing research and experiments to be continued.

6.9 Because these scans are done on biological models under a procedure licenced by the Home Office it is often not possible to repeat the scan should an image artefact invalidate it.

6.10 As well as the cost of the failed scan this could significantly delay the research and also presents animal welfare and ethical concerns for the University.

6.11 In addition, in the imaging area of the AMB there is currently space for future equipment that will need to be procured via bids to research funding bodies. If our imaging area no longer performs as per the original design specification for the AMB this could materially affect our ability to win future bids.

Effects of noise and vibration on animal welfare and research where rodents and fish are used

6.12 The AMB has specialist working requirements in respect of environmental laboratory conditions, with an extremely narrow tolerance range beyond which research outcomes would be rendered unreliable. As mentioned above, VC-A was adopted

as a design specification of the building based on the successful operation of the previous research facilities. The University did not anticipate further railway-related development. The major concern of the University is the potential for impacts at both construction and operational phases to impact on the welfare of the animals but also the outcomes of the research work.

6.13 Further, whilst there remains no definitive study or regulation that prescribes a specific vibration criterion or the exact quantifiable effect which causes harm to animals or experiments, noise and vibration in a laboratory animal facility are cited in research as factors that can induce stress in animals and alter research results. This research reinforces the University's decision to adopt a limit of VC-A for areas that could be used for animal work based on the mixture of past experience and recommended good practice as described above.

6.14 Thus laboratories have described[11] (please see **Appendix 3** for relevant extracts) construction-associated research effects caused by vibration, noise, or both, including alteration of energy balance, decreased food consumption and body weight, increased stillbirths and pup mortality and a marked stress response resulting in elevation of plasma ACTH,[12] corticosterone,[13] and aldosterone.[14]

6.15 A further study in 2015 (please see **Appendix 3** for relevant extracts) looked at the effects on breeding of mice in a building with close proximity to a train line. It concluded as follows:

"Analysis of the fecal samples revealed that vibrations similar to those produced by a passing train can increase the levels of fecal corticosterone metabolites in female mice. These increases warrant attention to the effects of vibration on mice and, consequently, on reproduction and experimental outcomes";

"The preliminary data we gathered indicate that vibrations from passing trains create significant increases in the FCM levels of female mice. Fluctuations in stress may be

[11] See "Factors That Can Influence Animal Research", David G. Baker, DVM, PhD, MS, MPA, DACLAMa *(referring to Dallman et al., 1999; Raff et al., 2011; Rasmussen et al., 2009).*

[12] ACTH is "adrenocorticotropic hormone". It is made by the pituitary gland at the base of the brain and controls the production of another hormone, cortisol, which plays an important role in eg stress response and fighting infection.

[13] A steroid hormone involved in the regulation of energy, immune reactions and stress responses.

[14] A steroid hormone which regulates salt and water in the body, thus having an effect on blood pressure.

disruptive to research studies and breeding colonies. Elevated corticosterone levels can induce a variety of negative effects in rodents".[15]

6.16 The paper correctly highlights that a number of variables need to be factored into this analysis and that more work is needed, however it helps establish the basis for my concern from both a welfare and research perspective.

6.17 Excessive noise is well known to impair rodent health. A 2009 report published in the Journal of the American Association for Laboratory Animal Science[16] looking at the effects of constant construction noise 70-90db found that:

"groups of mice with litters were exposed to noise at 70, 80, or 90 dBA for 1 h daily during the first week after parturition. Litter size, birth weight, incidence of stillborn pups, and rate of neonatal weight gain were analyzed. Noise decreased reproductive efficiency by decreasing live birth rates and increasing the number of stillborn pups."[17]

6.18 A further paper in 2011[18] suggested a link between noise and vibration and adverse effects on research results (see **Appendix 3** for relevant extract). Further a paper in 2007 found that:

"because faculty are the least aware of noise as a potential problem but are primarily responsible for designing experiments, research involving animals may be confounded by noise as an unknown variable. This effect may lead to unnecessary numbers of animals being required to achieve statistical significance and possibly to erroneous interpretation of results".[19]

6.19 Noise and vibration are, therefore, known stressors and can produce a number of changes in mice, some of which will be more detectable than others over both a long-

---

[15] *"Characterization of Train-Induced Vibration and its Effect on Fecal Corticosterone Metabolites in Mice",* Nicholas A Atanasov,1 Jennifer L Sargent,2 John P Parmigiani,1 Rupert Palme,3 and Helen E Diggs2,* Journal of the American Association for Laboratory Animal Science Vol 54, No 6 November 2015 Pages 737–744

[16] "Construction Noise Decreases Reproductive Efficiency in Mice Skye Rasmussen", Gary Glickman, Rada Norinsky, Fred W Quimby, and Ravi J Tolwani, Journal of the American Association for Laboratory Animal Science Vol 48, No 4 July 2009 Pages 363–370

[17] "Construction Noise Decreases Reproductive Efficiency in Mice Skye Rasmussen", Journal of the American Association for Laboratory Animal Science Vol 48, No 4 July 2009 Pages 363-70.

[18] "Comparative Vibration Levels Perceived Among Species in a Laboratory Animal Facility", Journal of the American Association for Laboratory Animal Science , Sept 2011

[19] "Are investigators aware of environmental noise in animal facilities and that this noise may affect experimental data?" J Am Assoc Lab Anim Sci. 2007 Jan; 46(1): 45-51.

and short-term duration[20]. Elevated levels of noise and vibration are associated with a number of adverse physiological and behavioural changes in rodents and fish.

6.20 In the case of mice, the successful breeding of which is essential, the effect of excessive noise and vibration would be behavioural disturbance and interference with reproduction, including infertility, abortion, mismothering or cannibalism of pups. The most commonly recorded consequence of elevated vibration levels is an increase in stress hormones with breeding animals being most sensitive. Intermittent or persistent noise levels also have the potential to affect studies and the breeding potential of the rodents within the AMB. Whilst sudden loud noises can have a more easily recordable and sudden affect, constant noise can also be a factor.

6.21 Moreover, some strains of rodents used at the AMB are also sensitive to stress which would result in poor breeding performance. Not only could there be increased litter losses, but larger numbers of rodents would need to be used in breeding, with the additional consequence of increased costs for the research. In addition, different strains and individual mice can act differently to stressors meaning mild difference that may affect one strain may not have any effect on another.

6.22 In relation to fish, the potential effects are behavioural disturbance and hearing damage. In particular, exposure to noise and vibration causes stress response behaviour, increased susceptibility to disease and reduced survival.

6.23 A particular issue is that it is absolutely vital to establish a consistency in the environment for the rodents and fish and minimise vibration stressors. A lack of reproducibility is a significant problem in biomedical science and with significant levels of interference caused by noise and vibration impacts are likely to cause issues with result validation.

6.24 Therefore, if not properly assessed and mitigated, my concern is that the stress and anxiety caused by noise and vibration from the proposed scheme could cause significant impact to research with these species, by substantially disrupting and invalidating research results. All this may call into question results and damage the impact of research outcomes and reporting during peer review process, by which papers are scrutinised by other academics in the field to test research results.

[20] See further evidence relating to research papers as described in the evidence of Rupert Thornely-Taylor

6.25 Even “short-term” disruption could turn into long-term disruption for many researchers at the AMB. Whilst some effects could be easily detectable other impacts could take years to recognise as more comparative data is produced. It is this unknown which, as well as causing an animal welfare concern, puts our research and reputation at risk. In the absence of a firm regulatory criterion or standard based on evidence of harm to animals or fish (or of clearly identified thresholds for changes in their behaviour), a major concern is not only of impacts which are identifiable beyond what the AMB has been designed for, but also impacts arising from new development that could affect research results in a way that might not be immediately obvious until years of more comparable data is collected.

6.26 The potential effect on research is also a significant welfare concern. The University is committed to the principles of the 3Rs. If disruption to research work requires repetition of experiments and/or the increased use of animals, this would raise concerns regarding adherence to these principles. Any of the negative effects I have identified could affect their welfare which would be unethical and damage the University’s reputation. This highly emotive subject could then damage the Universities reputation and lead to increased objections to the work carried out by the University.

6.27 The concerns I summarise above are supported by those held by groups working in the AMB. Relevant correspondence is in **Appendix 4** and I set out extracts below.

6.28 The Institute of Metabolic Science (“**IMS**”) performs a considerable number of studies involving mice at the AMB which may be impacted by low intermittent noise and vibrations, resulting in potential stress-related effects and behaviours in the mice. Correspondence from the IMS which highlights the following:

“Short term concerns: The results of many procedures performed are sensitive to the animals stress levels. For example, investigators routinely measure acute stress-sensitive parameters such as blood glucose and insulin. Eating behaviour is also affected by stress, which is of concern when food intake is a key parameter in many studies. Finally, IMS performs behavioural studies on mice, especially those that have previously undergone surgical interventions, and acute noise and vibration interference could impact the outcome of these sensitive experiments. We also perform continuous monitoring of mouse vital signs through telemetry, such that low intermittent noise and vibrations may introduce errors and variability in the data. Stress-sensitive parameters would need larger numbers of experimental animals to derive significance, since the variability of the data would increase, or in

extreme cases make the data completely unusable if the external interference was large enough..

Longer term concerns: Many of the readouts that IMS researchers examine are the result of long-term or ageing experiments. Chronic release of stress hormones affect these parameters and whole body metabolic status more generally. This alters many of the parameters which are primary readouts from experiments that IMS performs, such as body weight changes, glucose tolerance and insulin sensitivity. The net result of this is two-fold. Data generated during these conditions could lead to the same variability issues as mentioned above, requiring larger group sizes as well as increased cost in animals and caging. Secondly, the data becomes less comparable to that in other facilities, and with previously generated datasets in AMB. A lack of reproducibility is a significant problem in biomedical science and depending on the level of interference, noise and vibration may cause issues with result validation. It is also worth noting that some strains we work with are also sensitive to stress that results in poor breeding performance. Not only could we see increased litter losses, but we would need larger numbers of animals to be used in breed, with the consequence of increased costs for the investigation"

6.29 The University of Cambridge Named Veterinary Surgeons have raised concerns as follows:

"Elevated levels of noise is associated with a number of physiological and behavioural changes in mice and other laboratory animals. The cardiovascular, hormonal, reproductive and sleep systems all have reported changes after exposure to noise. These include increased heart rate, blood pressure, decreased fertility rates and milk production, elevated stress hormones, slower wound healing and poorer cognitive development. The reported cut-off point at which sound pressure levels start to effect change are at 70 db. Intermittent or persistent noise levels above this point would affect studies and the breeding potential of the mice";

"The most commonly recorded consequence of elevated vibration levels is an increase in stress hormones with breeding animals being most sensitive".

6.30 The potential implications of inadequately controlled operations would be significant. The volume of the work undertaken at the AMB, its interdependency with the rest of the CBC, as well as the elongated time period of the disruption at the AMB because of

the proposed scheme, means that vital research could be paused for years or lost altogether.

6.31 The ARRIVE Guidelines (Animal Research: Reporting of In Vivo Experiments) are a checklist of recommendations to improve the reporting of research involving animals – maximising the quality and reliability of published research and enabling others to better scrutinise evaluate and reproduce it. Under the ARRIVE Guidelines the University may need to state clearly on research papers a change in the housing environment of the animals:

"The environment determines the health and wellbeing of the animals and every aspect of it can potentially affect their behavioural and physiological responses, thereby affecting research outcomes. Different studies may be sensitive to different environmental factors, and particular aspects of the environment necessary to report may depend on the type of study"[21]

6.32 In the worst case of interruptions, experiments would need to be delayed or cancelled. This would not simply amount to increased costs, as it would lead to associated delays to the completion of research (or an inability to complete it), publication of results and students and researchers failing to complete work by the end of grant deadlines. This would lead to the loss of both direct research grant income to the University but also have a devastating impact upon the vital research activities that rely upon the AMB, possibly preventing these from proceeding for a number of years or at all. This would in turn have a detrimental impact on a number of careers, including those of PhD students.

6.33 Each research grant is for a period of five years on average. Even assuming that to address temporary effects from construction, the University were only to repeat the grants of the preceding two years to maintain consistency of results, this would amount to a very substantial cost to replace ineffective grant funding (see the evidence of Colin Smith – and my reference above to the £41.5m of annual grant funding supported by work at the AMB). But the longer-term implications, of any such interruption or other operational effects, are unknown. If the AMB could not be relied upon to serve its function of providing a world class, reliable facility to conduct research, its potential future may be called into question, with extremely serious effects on the University, its work and its reputation.

[21] Section 15: Housing and Husbandry of the ARRIVE Guidelines

7 NETWORK RAIL PREPARATION AND PROMOTION OF THE ORDER SCHEME

7.1 Other witnesses have addressed the technical aspects of the assessment work undertaken by Network Rail to support the draft Order. The conclusion that I draw from their evidence is that the material submitted by Network Rail has failed to properly understand, assess or mitigate the particular effects that would arise on such a specialist and sensitive facility as the AMB. This confirms my own impression from reading the chapters in the ES which addressed noise and vibration in particular. The preparation of my own evidence has been difficult given the lack of specific and clear information on potential impacts on identified receptors, including rodents and fish, without any clear assessment of the steps that could be taken to prevent those impacts from arising, based on identifiable or agreed criteria relating to noise and vibration in particular (but also EMI).

7.2 Other witnesses also comment on the extent of discussions (or lack of them) which have taken place with Network Rail since the University submitted its Statement of Case. At the time of writing those discussions are continuing, but with no agreement. I consider that the only responsible course as Operations Director is to support the ongoing objection to the Order unless and until satisfied that the position of the University, in particular its interest in the AMB, can be properly protected.

7.3 As matters stand the University has sought through its evidence to explain why further detailed information is necessary to understand the potential effects on the AMB and any detailed mitigation strategy that might be required to ensure the operations can continue effectively there. In the absence of that information, it has sought to identify key criteria which would avoid disturbance and impacts on the effective operation of AMB. However, until measures can be secured that properly protect the work carried on within the AMB, I am unable to conclude that the scheme would avoid huge potential risks to its operation. I will comment further as necessary in rebuttal evidence as and if the position changes.

8 SUMMARY AND CONCLUSIONS

8.1 The biomedical research facility at the AMB represents a major investment in UK scientific research and is a one-of-a-kind facility within the CBC. The AMB was opened in October 2019 as a new biomedical research facility to help further our understanding of how diseases occur and in the development of new treatments for conditions including cancer, dementia and diabetes. It supports globally important research activities across the CBC, including pioneering research into Covid-19. This includes: the use of imaging equipment to test the flow of dyes that is then adopted for wider imaging purposes in medical treatment (including nuclear medicine); the modelling of disease including through the use of genetic modification to develop cures; and the replication of organs in vitro to aid drug development and organ replacement technology.

8.2 University researchers at the AMB use MRI equipment for testing disease treatments, and to acquire sub-millimetre images in lab specimen and animals. The University's research studies include imaging abdominal and brain cancers, brain aneurysms, thrombectomies human cadaveric specimens, and cardiac and respiratory diseases. Work is performed with the University and Addenbrooke's Hospital researchers and with pharmaceutical companies, including AstraZeneca. High resolution imaging with limited noise and vibration interruptions are vital to ensure that these studies run efficiently and with limited disruptions to ensure the highest clinical impact.

8.3 As is common in biomedicine, research at the AMB involves the use of rodents and fish. This necessitates a Home Office Licence to be held to which Establishment Licence Conditions attach. The Licence conditions require, but in any event the University and other occupiers of the AMB aim to meet, the highest standards of animal welfare, underpinned by the principles of the '3Rs' of animal research. In total, the AMB houses over 25,000 rodents (excluding the animal research use of Astra Zeneca, who occupy part of floor 2) and several thousand fish.

8.4 Whilst delays due to COVID-19 mean that the AMB is still currently expanding its operational capacity, the AMB is nonetheless currently hosting 119 individual research grants (it has hosted others to date). The AMB recovers circa £3m of grant funding directly from researchers in receipt of grant funding, but its work overall supports a total of circa £41.5m per annum of research grants. In 2020/2021 these grants overall accounted for £34.8m relating to research activity in the School of Clinical Medicine (12% of that activity) and £6.7m relating to the School of Biological Sciences (5.5% of

that activity). The individual research grants are used by the holders of project licenses to meet the costs of receiving services and occupying research space within the AMB. Services provided within the AMB include a range of important services relating to animal welfare and the carrying out of scientific procedures to support research work. Other than the 80+ staff who work permanently in the building over 650 researchers and support staff have daily access.

8.5 The AMB itself provides unique service and support space not found anywhere else within the CBC. Because of the highly regulated nature of these spaces they have to be designated with specific environmental conditions so are not easily created or replicated. This means that the AMB researchers, from both the University and collaborative partners, use it as a specialist hub, whilst maintaining their own labs elsewhere on the CBC, often taking samples and work back and forth in support of a range of academic research goals. This supports the University's aim to translate research and clinical excellence into practical human health benefits, such as new therapeutics, devices, diagnostics or other interventions.

8.6 Given the breadth of research activities and the specialist nature of the work undertaken, the AMB has specialist working requirements in respect of environmental laboratory conditions, with an extremely narrow tolerance range beyond which research outcomes would be rendered unreliable.

8.7 High-resolution imaging equipment is acutely sensitive to vibration and noise. The major concern of the University is the potential for further construction activity or operational effects of railway-associated development to affect this work. Increased ground vibrations risk causing image artefacts (i.e. abnormalities in the images) which in turn would render certain vital pieces of research useless. It is critical that this is avoided in order for on-going research and experiments to be continued.

8.8 The AMB also has specialist working requirements in respect of environmental laboratory conditions, with an extremely narrow tolerance range beyond which research outcomes would be rendered unreliable. In the case of mice, the successful breeding of which is essential, the effect of excessive noise and vibration would be behavioural disturbance and interference with reproduction, including infertility, abortion, mismothering or cannibalism of pups. The most commonly recorded consequence of elevated vibration levels is an increase in stress hormones with breeding animals being most sensitive. Intermittent or persistent noise levels also have the potential to affect studies and the breeding potential of the rodents within the AMB.

8.9 In relation to fish, the potential effects are behavioural disturbance and hearing damage. In particular, exposure to noise and vibration causes stress response behaviour, increased susceptibility to disease and reduced survival.

8.10 If not properly assessed and mitigated, my concern is that the stress and anxiety caused by noise and vibration from the proposed scheme could cause significant impact to research with these species, by substantially disrupting and invalidating research results. All this may call into question results and damage the impact of research outcomes, with serious implications for the work of the AMB and the wider research activity and reputation of the University.

8.11 Other witnesses have addressed the technical aspects of the assessment work undertaken by Network Rail to support the draft Order. The conclusion that I draw from their evidence is that the material submitted by Network Rail has failed to properly understand, assess or mitigate the particular effects that would arise on such a specialist and sensitive facility as the AMB. This confirms my own impression from reading the chapters in the ES which addressed noise and vibration in particular. The preparation of my own evidence has been difficult given the lack of specific and clear information on potential impacts on identified receptors, including rodents and fish, without any clear assessment of the steps that could be taken to prevent those impacts from arising, based on identifiable or agreed criteria relating to noise and vibration in particular (but also EMI).

8.12 As matters stand the University has sought through its evidence to explain why further detailed information is necessary to understand the potential effects on the AMB and any detailed mitigation strategy that might be required to ensure the operations can continue effectively there. In the absence of that information, it has sought to identify key criteria which would avoid disturbance and impacts on the effective operation of AMB. However, until measures can be secured that properly protect the work carried on within the AMB, I am unable to conclude that the scheme would avoid huge potential risks to its operation. I will comment further as necessary in rebuttal evidence as and if the position changes.

9 WITNESS DECLARATION

I hereby declare as follows:

9.1 This proof of evidence includes all facts which I regard as being relevant to the opinions that I have expressed and that the inquiry's attention has been drawn to any matter which would affect the validity of that opinion.

9.2 I believe the facts that I have stated in this proof of evidence are true and that the opinions expressed are correct.

9.3 I understand my duty to the inquiry to help it with matters within my expertise and have complied with that duty.

Karl Wilson

University of Cambridge

APPENDIX 1

AMB IMAGES

LEVEL 0 EASTERN CORNER OF AMB

1.1 MRI

1.2 MRI Control Room

LEVEL 0 APPROXIMATELY CENTRE OF THE FLOOR PLATE

1.3 Aquatics Holding Room

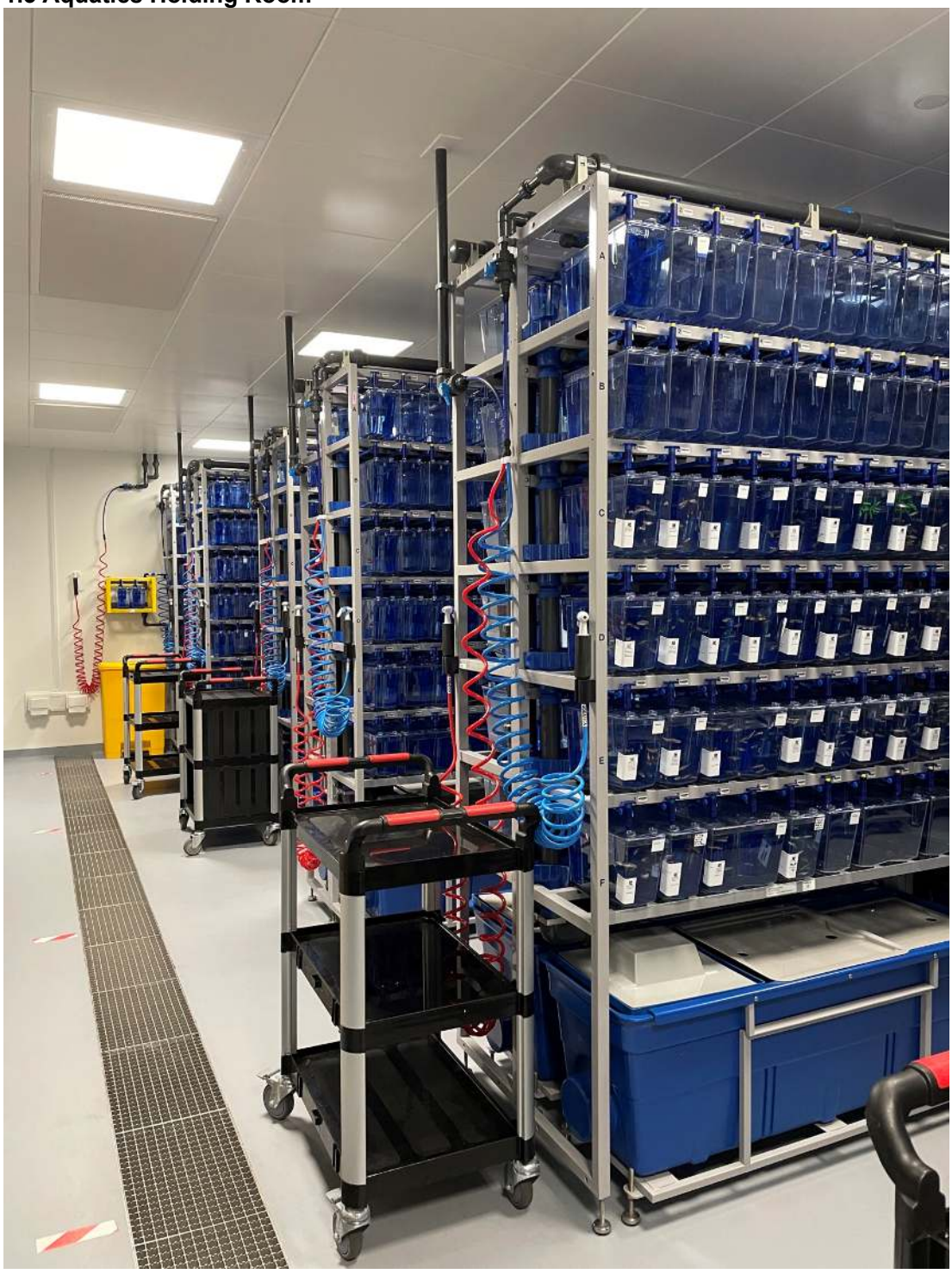

1.4 Example Rodent Holding Areas

APPENDIX 2

EXAMPLES OF RECENT PUBLICATIONS ON THE TYPES OF WORK CARRIED OUT IN THE AMB

1. M. Zaeem Cader et al ***"FAMIN Is a Multifunctional Purine Enzyme Enabling the Purine Nucleotide Cycle".*** Cell: Volume 180, Issue 2, 23 January 2020, Pages 278-295.e23

2. Galvin et al "***The human and mouse islet peptidome: effects of obesity and type 2 diabetes, and assessment of intra-islet production of glucagon-like peptide-1***", *J. Proteome Res. 2021, 20, 4507−4517*

Article

Cell

FAMIN Is a Multifunctional Purine Enzyme Enabling the Purine Nucleotide Cycle

Graphical Abstract

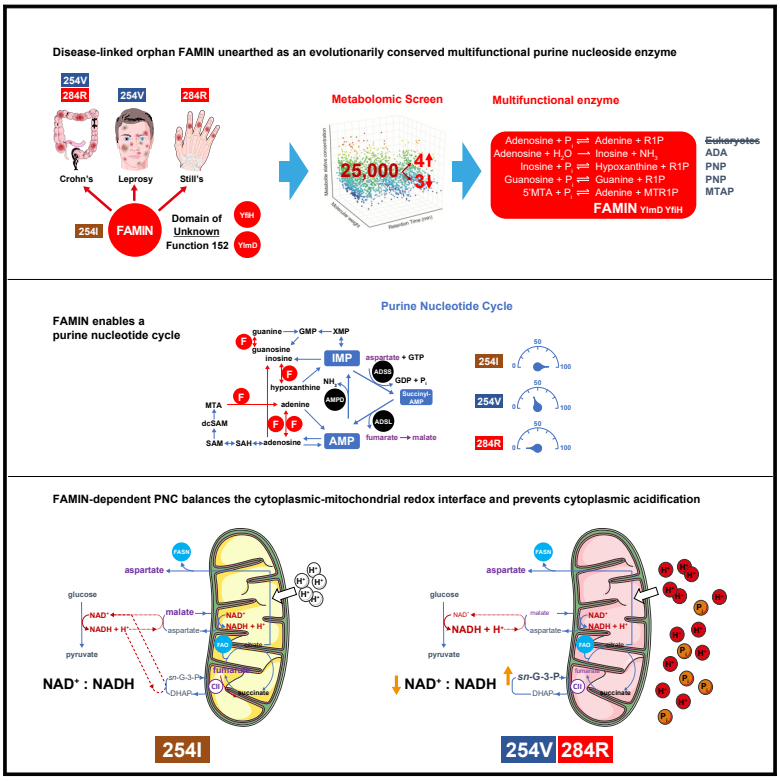

Highlights

- An unbiased LC-MS screen reveals FAMIN as a purine nucleoside enzyme
- FAMIN combines adenosine phosphorylase with ADA-, PNP-, and MTAP-like activities
- FAMIN enables a purine nucleotide cycle (PNC) preventing cytoplasmic acidification
- The FAMIN-dependent PNC balances the glycolysis-mitochondrial redox interface

Authors

M. Zaeem Cader,
Rodrigo Pereira de Almeida Rodrigues,
James A. West, ..., Yorgo Modis,
Julian L. Griffin, Arthur Kaser

Correspondence

ak729@cam.ac.uk

In Brief

Disease-linked, orphan FAMIN is an evolutionarily conserved, multifunctional purine nucleoside enzyme, with not only ADA-, PNP-, and MTAP-like activities but also adenosine phosphorylase activity. FAMIN enables a purine nucleotide cycle that balances the cytoplasmic-mitochondrial redox interface and prevents cytoplasmic acidification.

Cader et al., 2020, Cell *180*, 278–295
January 23, 2020
https://doi.org/10.1016/j.cell.2019.12.017

CellPress

Cell

Article

FAMIN Is a Multifunctional Purine Enzyme Enabling the Purine Nucleotide Cycle

M. Zaeem Cader,[1,2,8] Rodrigo Pereira de Almeida Rodrigues,[1,2,8] James A. West,[1,2,3,8] Gavin W. Sewell,[1,2] Muhammad N. Md-Ibrahim,[1,2] Stephanie Reikine,[1,4] Giuseppe Sirago,[1,2] Lukas W. Unger,[1,2] Ana Belén Iglesias-Romero,[1,2] Katharina Ramshorn,[1,2] Lea-Maxie Haag,[1,2] Svetlana Saveljeva,[1,2] Jana-Fabienne Ebel,[5] Philip Rosenstiel,[5] Nicole C. Kaneider,[1,2] James C. Lee,[1,2] Trevor D. Lawley,[6] Allan Bradley,[1,6] Gordon Dougan,[1,7] Yorgo Modis,[1,4] Julian L. Griffin,[3] and Arthur Kaser[1,2,9,*]

[1]Cambridge Institute of Therapeutic Immunology and Infectious Disease, Jeffrey Cheah Biomedical Centre, University of Cambridge, Cambridge CB2 0AW, UK

[2]Division of Gastroenterology and Hepatology, Department of Medicine, University of Cambridge, Addenbrooke's Hospital, Cambridge CB2 0QQ, UK

[3]Department of Biochemistry and Cambridge Systems Biology Centre, University of Cambridge, Cambridge CB2 1GA, UK

[4]Molecular Immunity Unit, Department of Medicine, University of Cambridge, MRC Laboratory of Molecular Biology, Cambridge CB2 0QH, UK

[5]Institute of Clinical Molecular Biology, Christian Albrechts University, Campus Kiel, 24105 Kiel, Germany

[6]Wellcome Trust Sanger Institute, Hinxton CB10 1SA, UK

[7]Division of Infectious Diseases, Department of Medicine, University of Cambridge, Cambridge CB2 0QQ, UK

[8]These authors contributed equally

[9]Lead Contact

*Correspondence: ak729@cam.ac.uk

https://doi.org/10.1016/j.cell.2019.12.017

SUMMARY

Mutations in FAMIN cause arthritis and inflammatory bowel disease in early childhood, and a common genetic variant increases the risk for Crohn's disease and leprosy. We developed an unbiased liquid chromatography-mass spectrometry screen for enzymatic activity of this orphan protein. We report that FAMIN phosphorolytically cleaves adenosine into adenine and ribose-1-phosphate. Such activity was considered absent from eukaryotic metabolism. FAMIN and its prokaryotic orthologs additionally have adenosine deaminase, purine nucleoside phosphorylase, and *S*-methyl-5′-thioadenosine phosphorylase activity, hence, combine activities of the namesake enzymes of central purine metabolism. FAMIN enables in macrophages a purine nucleotide cycle (PNC) between adenosine and inosine monophosphate and adenylosuccinate, which consumes aspartate and releases fumarate in a manner involving fatty acid oxidation and ATP-citrate lyase activity. This macrophage PNC synchronizes mitochondrial activity with glycolysis by balancing electron transfer to mitochondria, thereby supporting glycolytic activity and promoting oxidative phosphorylation and mitochondrial H^+ and phosphate recycling.

INTRODUCTION

FAMIN (Fatty Acid Metabolism-Immunity Nexus; *LACC1*, C13orf31) is strongly linked to human disease (Table S1). Highly penetrant mutations, such as C284R, cause juvenile idiopathic arthritis (JIA), Still's disease (a fever with rash followed by arthritis), or early-onset inflammatory bowel disease (IBD). A common coding polymorphism (I254V) increases risk for Crohn's disease (CD; an IBD) and leprosy, an infection with *Mycobacterium leprae*.

Mice with germline deletion (*Famin*$^{-/-}$) or engineered to express human non-risk, risk, and monogenic disease FAMIN variants (*Famin*$^{p.254I}$, *Famin*$^{p.254V}$, and *Famin*$^{p.284R}$, respectively) revealed that reduced or absent FAMIN activity increases the severity of experimental sepsis and arthritis (Cader et al., 2016; Skon-Hegg et al., 2019). Mitochondrial and NOX2-dependent reactive oxygen species (ROS) generation, bacterial killing, NOD2- and Toll-like receptor (TLR)-dependent signaling, inflammasome activation, and cytokine secretion are compromised with impaired FAMIN and linked to perturbed mitochondrial function (Cader et al., 2016; Lahiri et al., 2017). Oxidative phosphorylation (OXPHOS) and glycolysis are compromised and total cellular adenosine triphosphate (ATP) reduced in *Famin* mutant macrophages. Impaired FAMIN compromises both classically activated "M1" macrophages and alternatively activated "M2" macrophages (Cader et al., 2016; O'Neill and Pearce, 2016). FAMIN tethers to the cytosolic surface of peroxisomes in a complex with fatty acid synthase (FASN) (Assadi et al., 2016; Cader et al., 2016; Hillebrand et al., 2012). The flux of glucose carbon into fatty acid synthesis and fatty acid oxidation (FAO) is curtailed in *Famin* mutant macrophages (Cader et al., 2016). How FAMIN, which shares homology with bacterial orthologs (Pfam motif Domain of Unknown Function [DUF] 152), exerts such profound immunometabolic control had remained enigmatic.

Here, we report an unbiased metabolomic screen for enzyme activity that unearthed FAMIN as a conserved multi-functional purine nucleoside metabolizing enzyme with activities that challenge fundamental principles of purine metabolism.

RESULTS

Unbiased High-Complexity Metabolomic Screen

Identifying biochemical functions of orphan proteins is a formidable challenge (Prosser et al., 2014). We devised an unbiased screen for enzyme activity against an extensive library of metabolites without *a priori* assumptions on putative function. From transiently transfected HEK293T cells, we purified chromatographically monomeric recombinant human FAMIN (referred to as "FAMIN^{254I}" for the fully active variant), which exhibited stable properties in solution consistent with correct folding and lack of aggregation (Figures S1A–S1C). We generated a metabolite library from the human hepatocellular carcinoma cell line HepG2 transfected with *FAMIN* small interfering RNA (siRNA), which proliferated less and exhibited reduced glycolysis and OXPHOS (Figures S1D and S1E). Hence, FAMIN performed a non-redundant role, letting us expect that extracts would contain all cofactors and substrates required for its activity.

We adopted quantitative, high-sensitivity and high-resolution orthogonal liquid chromatography-mass spectrometry (LC-MS) to resolve a wide range of highly diverse metabolites. We identified >25,000 unique quantifiable LC-MS features in freeze-dried aqueous extracts of *FAMIN*-silenced HepG2 cells across chromatography modalities and ionization modes (Figure 1A). We incubated 10 μg recombinant human FAMIN^{254I} or an equivalent volume of protein buffer, with the metabolite library resuspended in phosphate-buffered saline (PBS) (pH 7.4) for 1 h at 37°C. Samples were then re-extracted and analyzed. Within this vast library, 3 LC-MS features significantly decreased and 4 increased in abundance in the FAMIN^{254I} compared to the mock reaction (Figures 1B and 1C).

The *m/z* values of the 3 LC-MS features with reduced abundance (a–c in Figures 1B and 1C) matched exactly those of purine nucleosides. Molecular formula determination, using accurate mass and supported by isotopic mass distribution, also indicated compounds a–c were purine nucleosides. Molecular formula and *m/z* could not unambiguously discriminate their identity. Comparing chromatography characteristics of a–c against authentic standards demonstrated that the retention times exactly matched adenosine, inosine, and guanosine (Figures 1D, 1E, S1F, and S1G), suggesting FAMIN catabolizes the major cellular purine nucleosides. Consistent with this, the *m/z* values of LC-MS features d–f (Figures 1B and 1C), whose levels increased in the presence of FAMIN^{254I}, matched hypoxanthine, guanine, and a pentose-phosphate, respectively (Figures 1E and S1G). LC-MS feature g corresponded to xanthine, although levels were extremely low. Modified chromatography unambiguously separated isomeric pentose-phosphates and identified feature f as ribose-1-phosphate (R1P; Figure S1H). Recombinant FAMIN^{254I} did not affect any other nucleosides or nucleotides also present in our library (Figure S1I). Adenosine, inosine, and guanosine consumption increased with the amount of recombinant FAMIN^{254I} in the reaction (Figures 1F and S1I). This suggested FAMIN may be an enzyme acting on purine nucleosides to generate nucleobases and R1P.

FAMIN Combines Adenosine Deaminase, Purine Nucleoside Phosphorylase, and *S*-Methyl-5′-Thioadenosine Phosphorylase Activities

To unambiguously validate results from the library screen, we examined enzyme activity in a fully reductionist system using pure substrate. FAMIN^{254I} consumed adenosine and generated inosine, hypoxanthine, and R1P, which was confirmed by authentic standards (Figures 2A, 2B, and S1J). No spontaneous degradation of adenosine or formation of products occurred in the absence of FAMIN^{254I} or adenosine (Figures 2A and 2B), nor with an unrelated enzyme, cholesterol oxidase (Figure S2A). Because our LC methods did not resolve adenosine and adenine well and because adenosine can undergo source fragmentation to adenine, we applied further chromatography methods to separate them. This demonstrated that FAMIN^{254I} converted adenosine to adenine (Figure 2C), whereby ~85% of consumed adenosine yielded adenine and ~15% inosine (Figure 2D). FAMIN-catalyzed activities were further confirmed by tracing [$^{15}N_5$ $^{13}C_{10}$] adenosine-derived stable isotopes into reaction products (Table S2). Incubating FAMIN^{254I} with adenine and R1P yielded adenosine, demonstrating the reverse reaction (Figure 2E) and corroborating identities of the products of the forward reaction. No other adenosine products were detected, and heat-denaturing inactivated FAMIN^{254I} (Figure S2B). Consistent with orthophosphate (P_i) required for phosphorolysis, the reaction progressed only to inosine when performed in non-phosphate buffer (Figure S2B). Hence, FAMIN exhibited activities as adenosine deaminase and purine nucleoside phosphorylase, and reactions proceeded independently from each other (Figure 2F).

FAMIN^{254I} also metabolized pure inosine and guanosine into R1P and their respective nucleobases hypoxanthine and guanine (Figures 2G, 2H, S2C, and S2D), whereas no activity toward cytidine was detected (Figure 2G). FAMIN^{254I} also metabolized 2′-deoxy-adenosine, producing adenine, 2′-deoxy-inosine, hypoxanthine, and 2′-deoxy-R1P (Figures 2G and S2E–S2I). 5′-Deoxy-adenosine, a by-product of radical *S*-adenosylmethionine (SAM) enzymes (Landgraf et al., 2016), was also a substrate of FAMIN^{254I} (Figure S2J and S2K). FAMIN^{254I} further metabolized *S*-methyl-5′-thioadenosine (MTA) into adenine and *S*-methyl-5′-thioribose-1-phosphate (Figures 2H and 2I), while not affecting SAM (Figure 2G). Revisiting the library screen, we noticed a 50% reduction of MTA with 100 μg FAMIN^{254I} (Figure S2L). This added a third activity of FAMIN as a MTA phosphorylase (Figure 2J).

FAMIN's Purine Nucleoside Enzymatic Activities Are Conserved

Orthologs containing the C-terminal portion of FAMIN are widely distributed across prokaryotes but are confined to metazoans in eukaryotes (Figure S2M). An *Escherichia coli*-expressed, maltose-binding protein (MBP) fusion protein of truncated FAMIN containing the DUF152 homology domain only (FAMIN$^{\Delta176}$) exhibited all three enzymatic activities, similar to MBP-tagged full-length FAMIN (Figure S2N). Consistent with DUF152 containing all enzymatic activity, recombinantly expressed DUF152 bacterial proteins YlmD and YfiH metabolized adenosine to inosine and adenine, MTA to adenine, and

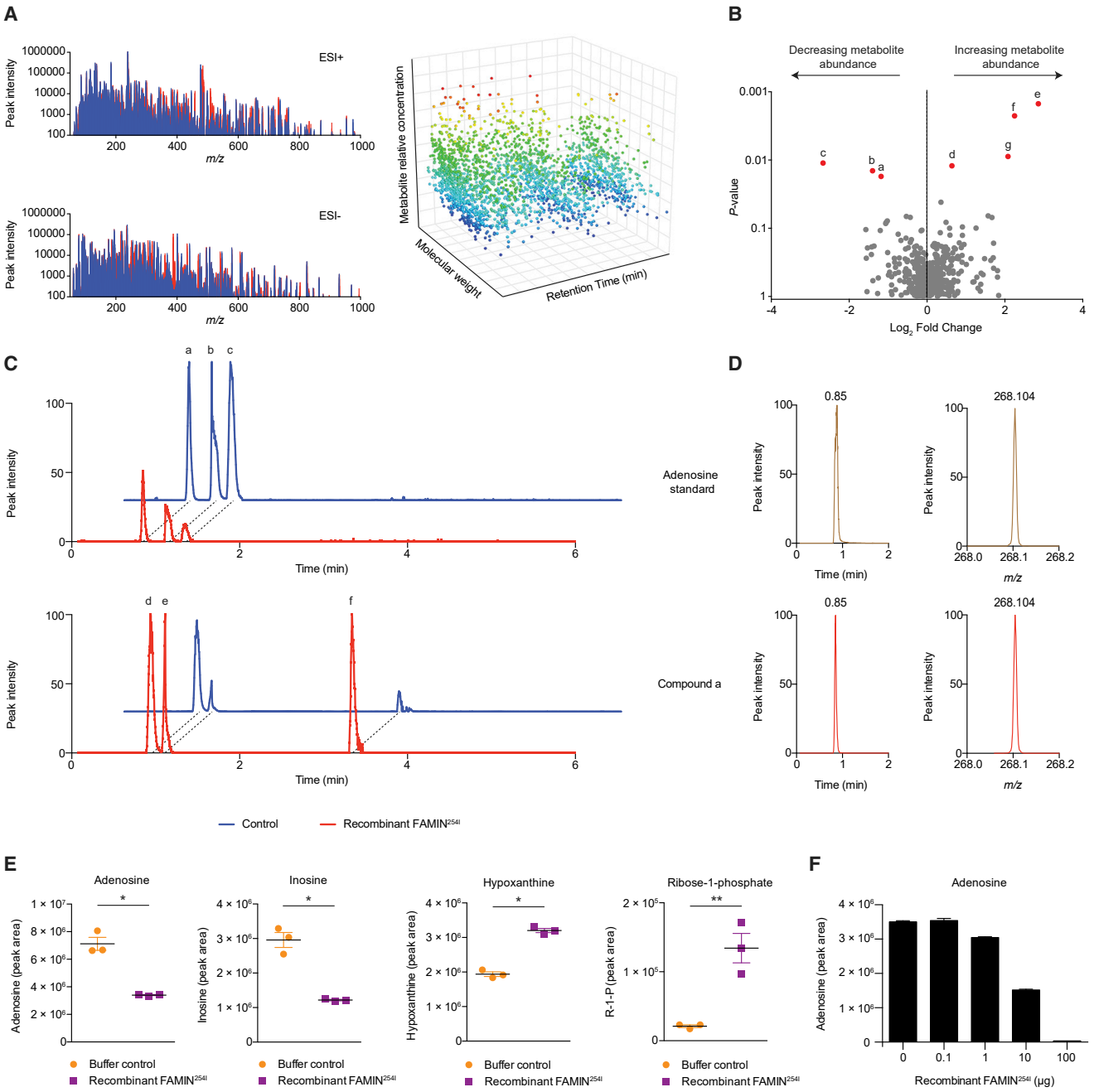

Figure 1. FAMIN Is a Purine-Nucleoside-Metabolizing Enzyme

(A) Metabolomic library of HepG2 cells after transfection with *FAMIN* siRNA. Representative total mass spectra (left) separated by molecular weight (*m/z*), chromatography retention time, and relative levels (right).

(B) Change in relative metabolite levels in the library after incubation with recombinant FAMIN^{254I} or protein buffer control, depicted as volcano plot with unadjusted p values. Red dots, candidate substrates and products whose abundance decreased (a–c) or increased (d–f; n = 3 independent reactions).

(C) Representative extracted chromatograms for candidate substrates (top) and products (bottom) by using normalized peak intensity for each given *m/z* value.

(D) Representative mass spectra and extracted chromatograms for compound a and corresponding authentic standard.

(E) Levels of adenosine, inosine, hypoxanthine, and ribose-1-phosphate (R1P) within the metabolomic library incubated with FAMIN^{254I} or protein buffer control (n = 3, mean ± SEM).

(F) Levels of adenosine within the metabolomic library incubated with 0.1–100 μg of FAMIN^{254I} or protein buffer control (n = 3, mean ± SEM).

Data representative of at least 3 independent experiments. *p < 0.05 and **p < 0.01 (unpaired, two-tailed Student's t test).

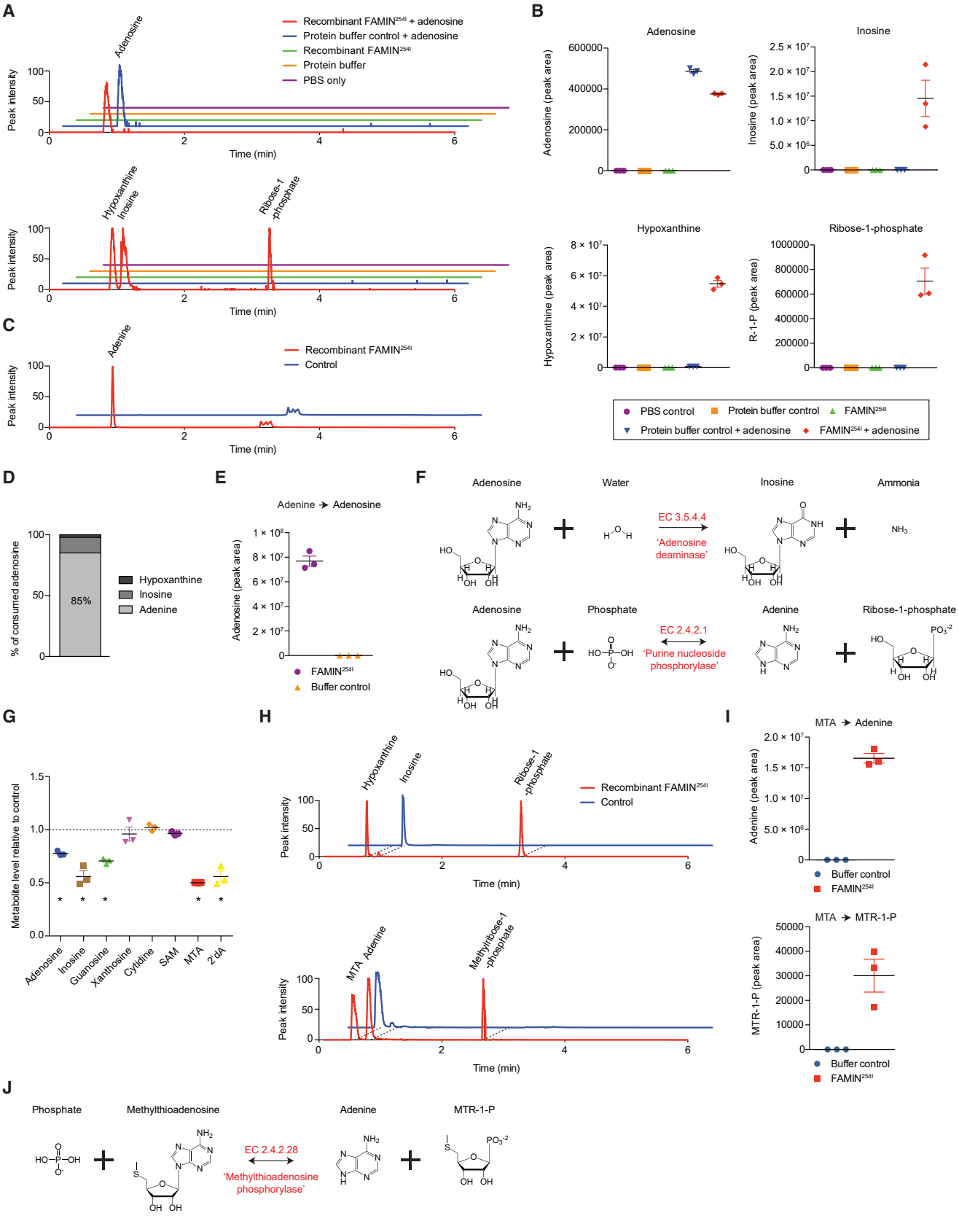

(legend on next page)

inosine to hypoxanthine (Figure 3A). Crystal structures of several bacterial DUF152 proteins have been determined and revealed a monomeric $\alpha/\beta/\alpha$ fold (Kim et al., 2006). To identify the binding pocket, we soaked YlmD crystals with inosine. Inosine-soaked crystals diffracted to 1.2-Å resolution and contained additional electron density not present in native YlmD crystals, unambiguously identifying the purine ring of a bound inosine molecule (Figure 3B; Table S3). The structure contained weaker additional density of a partially hydrolyzed or disordered ribose moiety (Figures 3C–3E). The hypoxanthine moiety forms a hydrogen bond with the side chain of Arg^{59}. The ribose moiety is coordinated by the side chains of Cys^{125}, His^{80}, and His^{142}, a triad conserved in YfiH and previously predicted as active site (Kim et al., 2006). In contrast to inosine-bound YlmD, in an apo-YlmD crystal that diffracted to 1.2 Å, the His^{47} side chain was found inserted into the purine-binding pocket (Figure 3C), consistent with a previously deposited apo structure (protein data bank [PDB]: 1T8H). The His^{47} side chain may act as a gatekeeper of the active site that rotates outward when the substrate binds. FAMIN has several aromatic residues in the corresponding loop that could function analogously to His^{47}. Atypical laccase activity has been ascribed to some bacterial DUF152 proteins based on a spectrophotometric method that monitors the oxidation of proxy substrates (Beloqui et al., 2006). In this method, YlmD, YfiH, and $FAMIN^{254I}$, in contrast to a conventional laccase, elicited only minuscule signals (Figure S3A). In a sensitive LC-MS method (Perna et al., 2018), laccase end-products were only detected with a conventional laccase but not with YlmD, YfiH, or $FAMIN^{254I}$ (Figure 3F). We conclude that FAMIN is a prototype of a new, evolutionarily conserved family of multifunctional purine-nucleoside-metabolizing enzymes.

FAMIN Combines Adenosine Phosphorylase with ADA-, PNP-, and MTAP-like Activities

Eukaryotic cells have been considered devoid of an enzyme that phosphorolytically converts adenosine to adenine (Friedkin and Kalckar, 1961; Maynes et al., 1999; Zimmerman et al., 1971). FAMIN adds such adenosine phosphorylase activity to mammalian metabolism and combines within one single enzyme three essential, non-redundant activities that supply purine nucleotide salvage. These latter activities had been thought to be due to single, ubiquitously expressed genes: adenosine deaminase (*ADA*; secreted ADA2 is expressed from a separate gene), purine nucleoside phosphorylase (*PNP*), and *S*-methyl-5′-thioadenosine phosphorylase (*MTAP*) (Ashihara et al., 2018; Murray, 1971). Loss of ADA or PNP activity causes severe combined immunodeficiency (Giblett et al., 1972, 1975), whereas *MTAP* is frequently deleted in cancers (Kryukov et al., 2016). ADA, PNP, and MTAP activities are critically important because adenosine, inosine, and guanosine and their nucleobases adenine, hypoxanthine, and guanine are neither precursors nor intermediates of *de novo* purine synthesis but are generated by the reactions that supply purine nucleotide salvage; salvage then proceeds by hypoxanthine guanine phosphoribosyl transferase (HPRT) and adenine phosphoribosyl transferase (APRT) (Camici et al., 2018).

I254V Switches Activity from Adenosine Phosphorolysis to Deamination

FAMIN's apparent K_ms for its main substrates were similar to those reported for ADA, PNP, and MTAP (Figure 3G; Table S4; Bzowska et al., 2000; Della Ragione et al., 1996; Lindley and Pisoni, 1993), although the corresponding V_{max}s were low (Table S4). We next addressed how I254V affected activity. Adenosine consumption was approximately halved with $FAMIN^{254V}$ compared to $FAMIN^{254I}$ (Figure 3H), with conversion to adenine and R1P 10-fold lower (Figure 3I), mirrored in the reverse reaction (Figure S3B). In contrast, the production of inosine and hypoxanthine by $FAMIN^{254V}$ was slightly higher and similar, respectively, compared to $FAMIN^{254I}$ (Figures 3I and S3C). Thus, $FAMIN^{254V}$ converted only ~20%, rather than $FAMIN^{254I}$'s 85%, of consumed adenosine to adenine, instead diverting it to inosine and thence hypoxanthine (Figure 3J). Phosphorolysis activities toward inosine and MTA were also lower in $FAMIN^{254V}$ than in $FAMIN^{254I}$ (Figures S3D and S3E). Hence, $FAMIN^{254I}$ and $FAMIN^{254V}$ activities differed quantitatively and qualitatively, favoring adenosine phosphorolysis and adenosine deamination, respectively.

FAMIN Controls Cellular Purine Levels

To address whether FAMIN affected cellular purine levels, we transiently transfected FAMIN expression vectors into HEK293T cells. $FAMIN^{254I}$ and $FAMIN^{254V}$ proteins express equally high, and $FAMIN^{284R}$ expression is negligible (Cader et al., 2016). Hypoxanthine, guanine, and inosine monophosphate (IMP) levels were higher 24 h after transfecting $FAMIN^{254I}$

Figure 2. FAMIN Has Adenosine Deaminase, Purine Nucleoside Phosphorylase, and *S*-Methyl-5′-Thioadenosine (MTA) Phosphorylase Activities

(A) Representative extracted chromatograms, using normalized peak intensity, for adenosine (top chromatogram); and inosine, hypoxanthine, and R1P (bottom chromatogram) following incubation of $FAMIN^{254I}$ or control with 100 μM adenosine.

(B) Adenosine, inosine, hypoxanthine, and R1P levels following incubation of recombinant $FAMIN^{254I}$ or control as per (A) (n = 3).

(C) Representative extracted chromatograms for adenine using a modified CSH-C18 method.

(D) Fractional conversion of adenosine into its products following incubation of Strep-tagged $FAMIN^{254I}$ with 100 μM adenosine (n = 3, mean).

(E) Adenosine levels in reactions of adenine and R1P in the presence of Strep-tagged $FAMIN^{254I}$ or control (n = 3).

(F) FAMIN-catalyzed enzymatic reactions.

(G) FAMIN activity toward purine and pyrimidine nucleosides, measured as substrate (each added at 100 μM) consumption (SAM; *S*-adenosylmethionine; 2′-dA, 2′-deoxyadenosine; n = 3).

(H) Representative extracted chromatograms for inosine, hypoxanthine, and R1P (top chromatogram); and MTA, adenine, and methylthioribose-1-phosphate (bottom chromatogram) upon incubation of inosine and MTA, respectively, with recombinant $FAMIN^{254I}$.

(I) Adenine and methylthioribose-1-phosphate levels upon incubation of MTA with $FAMIN^{254I}$ or buffer control (n = 3).

(J) Further FAMIN-catalyzed enzymatic reaction.

Data represented as mean ± SEM. *$p < 0.05$ (unpaired, two-tailed Student's t test).

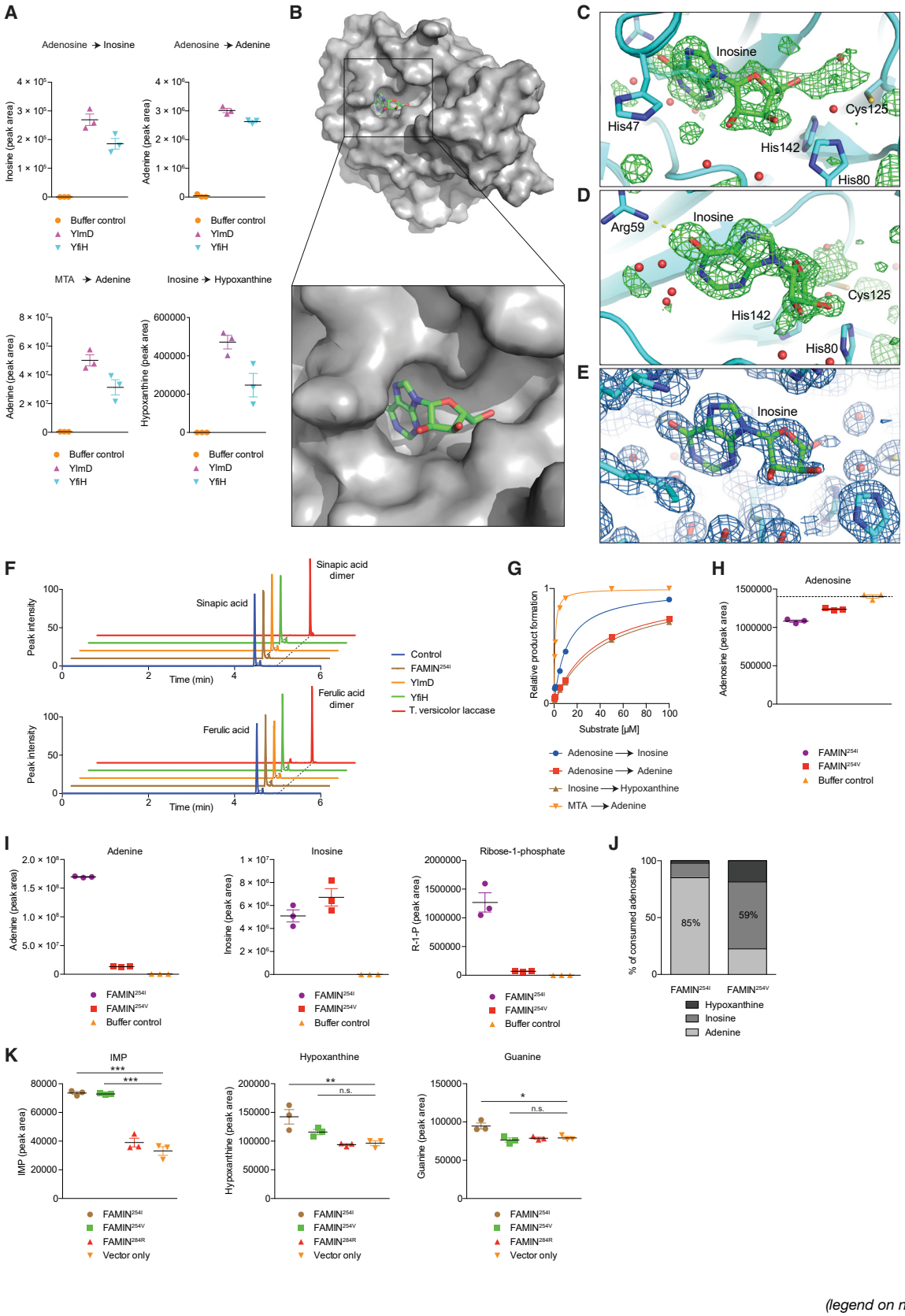

(legend on next page)

than in controls (Figure 3K). The doubling in levels of IMP, the obligatory intermediate of purine salvage and *de novo* synthesis (Camici et al., 2018), extended to FAMIN^{254V} transfectants, whereas the increase in hypoxanthine was moderate compared to FAMIN^{254I} (Figure 3K). Other purine nucleosides were not affected (Table S5). Conversely, IMP levels halved in HepG2 cells 24 h after transfecting *FAMIN* siRNA (Figure 4A), which, compared to control siRNA, boosted inosine, guanosine, and MTA and reduced hypoxanthine levels (Figures 4B and S3F). Hence, FAMIN impacted on the levels of central purines despite preserved ADA, PNP, and MTAP expression (Figure S3G), prompting us to compare proliferation and energy metabolism upon their knockdown. Although *MTAP* siRNA reduced proliferation (Figure S3H) and basal respiration similar to *FAMIN* siRNA, *MTAP*-silenced cells did not exhibit the steep decline in respiration of *FAMIN*-silenced HepG2 cells after eliciting spare respiratory capacity (SRC) (Figure S3I). Changes in cell shape were distinct between *MTAP* and *FAMIN* siRNA transfection (Figure S3J), whereas *ADA* and *PNP* siRNA affected proliferation and respiration overall differently from *FAMIN* siRNA (Figures S3H and S3I). Hence, FAMIN and the monofunctional enzymes did not cross-compensate for their individual absence.

FAMIN Affects Routing through Core Purine Metabolism

We next turned to murine bone marrow (BM)-derived M1 macrophages, in which disease-linked *Famin* variants cause immunometabolic compromise (Cader et al., 2016). In contrast to HepG2 cells, macrophages only use purine nucleotide salvage and hardly any *de novo* synthesis (Figures S3K–S3O). ADA, PNP, and MTAP expression is not affected by *Famin* genotype (Figure S3P). Cellular levels of adenine, adenosine, and ATP were lowest in *Famin*$^{p.284R}$, intermediate in *Famin*$^{p.254V}$, and highest in *Famin*$^{p.254I}$ macrophages (Figures 4C and 4D). MTA followed a similar pattern (Figure S4A). Hence, FAMIN increased the availability of adenyl groups, from nucleobase to nucleotide triphosphate. After a 3-h pulse with [$^{13}C_{10}{}^{15}N_5$] adenosine, 14% of cellular adenosine was of the [$^{13}C_{10}{}^{15}N_5$] isotopomer, irrespective of *Famin* genotype (Figure 4E). An even larger fraction of adenine, AMP, SAM cycle, and purine salvage metabolites had label incorporated (Figure 4E). They featured adenyl groups that had undergone deamination (i.e., $^{15}N_5 \rightarrow {}^{15}N_4$) and/or phosphorolysis (i.e., $^{13}C_{10} \rightarrow {}^{13}C_5$) (Figure 4E). Fractional incorporation of ^{13}C and ^{15}N into inosine, adenine, and hypoxanthine exhibited significant, although modest, differences across *Famin* genotypes (Figure S4B; Table S6). By tracing a 3-h [$^{15}N_5$] adenine pulse, we found that less than 6% of cellular adenine remained unlabeled (Figure S4C) and 12% of adenosine was of the [$^{15}N_5$] isotopomer, exhibiting genotype-specific differences (Figures S4C–S4E; and Table S6). After pulsing with either adenosine or adenine, one-fourth to one-third of AMP and ATP had label incorporated (Figures 4E and S4C). This high adenyl turnover extended to cofactors, i.e., coenzyme A (CoA), SAM, NAD^+, NADP, and flavin adenine dinucleotide (FAD) (Figures S4F and S5A), again with *Famin* genotype-specific differences (Table S6). Adenyl metabolism is highly interconnected including fast substrate cycles (Boison, 2013). Exogenous adenosine or adenine would not directly contact FAMIN without prior metabolization, potentially obscuring the extent of FAMIN's contribution. We, therefore, traced [$^{13}C_1{}^{15}N_2$] guanosine, which has fewer metabolic fates. After a 3-h pulse, fractional incorporation of [$^{13}C_1{}^{15}N_2$] increased from 19.5% ± 1.6% in *Famin*$^{p.284R}$ to 31.9% ± 1.3% in *Famin*$^{p.254I}$ macrophages (Figure 4F), driven by unlabeled guanosine accumulating in *Famin*$^{p.284R}$ cells (Figure S5B; Table S6). Similarly, the fraction of [$^{13}C_1{}^{15}N_2$]-labeled guanine increased from 30.9% ± 3% in *Famin*$^{p.284R}$ to 46.8% ± 2.6% in *Famin*$^{p.254I}$ macrophages (Figure 4G), whereas total levels of guanine remained constant across genotypes (Figure S5B). Fractional labeling of guanosine triphosphate (GTP) was also higher in *Famin*$^{p.254I}$ than in *Famin*$^{p.254V}$ and *Famin*$^{p.284R}$ macrophages (Figure 4H). Hence, FAMIN activity accounted for >50% higher fractional guanosine and guanine and >30% higher GTP labeling compared to cells without FAMIN activity. This demonstrated that FAMIN profoundly affected purine metabolism.

FAMIN Prevents Cytoplasmic Acidification

How does purine metabolism by FAMIN control glycolysis and OXPHOS? Unbiased high-resolution LC-MS of M1 macrophage

Figure 3. FAMIN Activities Are Evolutionarily Conserved and Adenosine Phosphorolysis Compromised in I254V

(A) Enzyme activities of YlmD and YfiH as measured by inosine, adenine, and hypoxanthine production (n = 3).

(B) Crystal structure of YlmD determined in the presence of inosine and phosphate, shown in molecular surface representation with a bound inosine as ball-and-stick.

(C and D) Substrate binding site of YlmD, polder *Fo-Fc* electron density map calculated at 1.5-Å resolution with inosine and bulk solvent omitted. Maps contoured at +3.5 σ (green mesh). (C) Cys^{125}-His^{80}-His^{142} located near inosine's ribose moiety. The His^{47} side chain inserted into the purine-binding pocket in apo-YlmD (semi-transparent representation). (D) View rotated 45° around the y axis. The hypoxanthine moiety forms a hydrogen bond with the Arg^{59} side chain (dashed line). Selected ordered water molecules (red spheres).

(E) 2*Fo-Fc* electron density map near the bound inosine calculated after refinement with diffraction data to 1.2-Å resolution and contoured at +1.2 σ (blue mesh). Viewing orientation between those in (C) and (D).

(F) Representative extracted chromatograms demonstrating oxidation of laccase substrates sinapic and ferulic acid into dimer products after incubation with YlmD, YfiH, Strep-tagged FAMIN^{254I}, laccase from *Trametes versicolor*, or appropriate control.

(G) Michaelis-Menten kinetics of FAMIN activities for indicated substrates.

(H and I) Consumption of adenosine (H) and production of adenine, inosine, and R1P (I) following incubation of Strep-tagged FAMIN^{254I}, FAMIN^{254V}, or buffer control with 100 μM adenosine (n = 3).

(J) Fractional conversion of adenosine into adenine versus inosine versus hypoxanthine following incubation of adenosine with Strep-tagged FAMIN^{254I} or FAMIN^{254V} (n = 3, mean).

(K) Inosine monophosphate (IMP), hypoxanthine, and guanine levels in HEK293T cells after transient transfection with FAMIN expression vectors or empty vector (n = 3).

Data represented as mean ± SEM. *p < 0.05, **p < 0.01, and ***p < 0.001 (unpaired, two-tailed Student's t test).

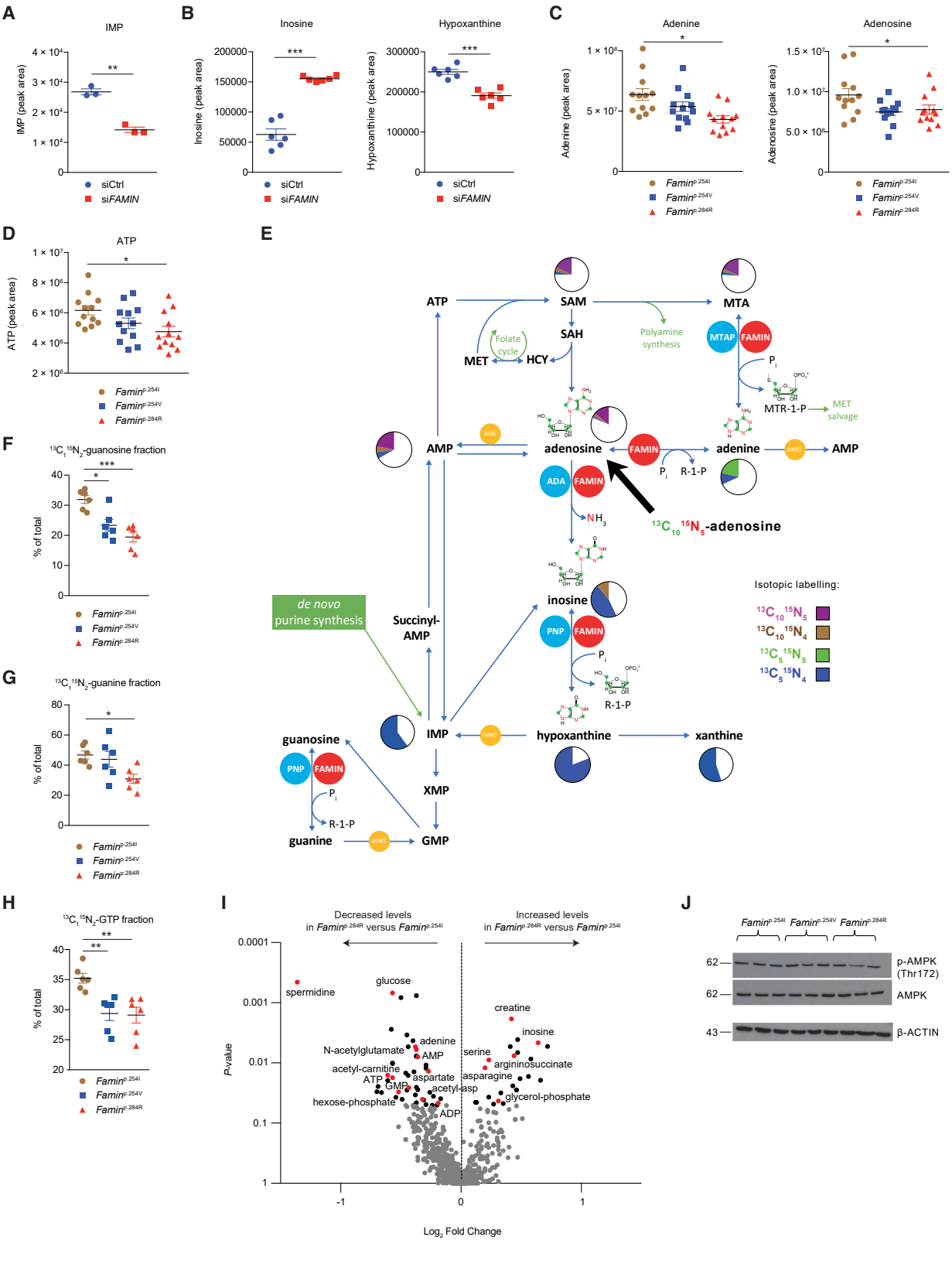

(legend on next page)

aqueous extracts revealed 67 LC-MS features of differential abundance between *Famin*$^{p.254I}$ and *Famin*$^{p.284R}$ and 157 between *Famin*$^{p.254I}$ and *Famin*$^{p.254V}$ cells after false discovery rate (FDR) correction (Figures 4I and S5C). Reassuringly, top dysregulated metabolites were adenine, inosine, hypoxanthine, ADP, AMP, and guanosine monophosphate (GMP) (Figures 4I and S5C). Key metabolites of glycolysis, FAO, amino acid and polyamine metabolism, and the urea cycle were among non-purines dysregulated by FAMIN variants (Figures 4I and S5C). The energetic compromise (Figure 4D; Cader et al., 2016) did not lead to increased phosphorylation of AMP-activated protein kinase (AMPK), a key energy sensor (Lin and Hardie, 2018), in *Famin*$^{p.284R}$ compared to *Famin*$^{p.254I}$ macrophages (Figure 4J), consistent with AMP being reduced in parallel with ATP (Figure 4I). Massively parallel RNA sequencing of M0, M1, and M2 macrophages revealed only *Slc9a9*, *Mid1*, and *Rap1gap* as differentially expressed in *Famin*$^{p.254V}$ compared to *Famin*$^{p.254I}$, and only a further 32 transcripts as different between *Famin*$^{p.284R}$ and *Famin*$^{p.254I}$ (Figure 5A; Table S7). The near-absence of a transcriptional response to the cells' immunometabolic compromise pointed to a bona fide biochemical mechanism. *Slc9a9*, which encodes the Na^+-H^+ transporter 9 (NHE9) (Slepkov et al., 2007), provided an important clue. Na^+-H^+ transporters dynamically protect against cytoplasmic acidification stemming from the generation of protons (H^+) by metabolic reactions, primarily the hydrolysis of ATP into ADP, P_i, and H^+ (Casey et al., 2010; Ipata and Pesi, 2018; Robergs et al., 2004). The Gene Ontology set ''pH regulation'' was duly enriched in *Famin*$^{p.284R}$ compared to *Famin*$^{p.254I}$ macrophages (Figure 5B). Measuring cytoplasmic pH (pH_c) revealed a more acidic cytoplasm in *Famin*$^{p.254V}$ and *Famin*$^{p.284R}$ than in *Famin*$^{p.254I}$ M0 and M1 macrophages (Figures 5C and S5D). Acidification was confirmed by a dual-excitation ratiometric pH_c indicator that internally controls for probe uptake (Figure S5E) and extended to *FAMIN*- compared to control-silenced HepG2 cells (Figure S5F).

A Purine Nucleotide Cycle Is Active in Macrophages

Cytoplasmic acidosis in *Famin*$^{p.254V}$ and *Famin*$^{p.284R}$ compared to *Famin*$^{p.254I}$ M1 macrophages was accompanied by elevated levels of cellular P_i (Figure 5D). *Famin*$^{-/-}$ macrophages are also depleted of phosphocreatine (Cader et al., 2016), a phosphoryl group carrier for near-immediate ADP rephosphorylation. Cytoplasmic acidosis, P_i accumulation, dwindling ATP levels, and depletion of phosphocreatine are hallmarks of exhaustive muscle exercise (Ipata and Pesi, 2018; Robergs et al., 2004). They occur when the rate of ATP hydrolysis is higher than fast-paced ADP rephosphorylation by glycolysis and phosphocreatine, hence, when the capacity to recycle H^+ by creatine kinase, lactate dehydrogenase (LDH), and (slow) mitochondrial uptake is exceeded. When immediate rephosphorylation is impossible, the myokinase reaction (adenylate kinase, AK1) converts two molecules of ADP into one ATP and one AMP (Figure 5E; Ipata et al., 2011). In muscle cells, AMP enters the cytoplasmic purine nucleotide cycle (PNC) consisting of AMP deaminase (AMPD), adenylosuccinate synthase (ADSS), and adenylosuccinate lyase (ADSL) (Ipata and Pesi, 2018; Lowenstein and Tornheim, 1971; Lowenstein, 1990). AMPD releases NH_4^+ and generates IMP; ADSS synthesizes succinyl-AMP from IMP and aspartate at the expense of GTP; and ADSL regenerates AMP by releasing fumarate, which after conversion to malate enters mitochondria (Figure 5E). A reduction of IMP and an increase in aspartate were among few early (24 h; Figure S5G) changes and a decrease in fumarate and malate among later (48 h; Figure S6A) changes after *FAMIN* siRNA transfection into HepG2 cells. Murine primary macrophages express *Ampd2*, *Ampd3*, *Adss*, and *Adsl* (Figure S6B). Knockdown of *Adss* or *Adsl* in *Famin*$^{p.254I}$ M0 macrophages reduced baseline oxygen consumption rate (OCR) compared to controls (Figure 5F). Uncoupling respiration from mitochondrial ATP synthesis by carbonyl cyanide-4-phenylhydrazone (FCCP; i.e., eliciting SRC) revealed an even larger difference in OCR between *Adss* and *Adsl* compared to controls (Figure 5F). *L*-Alanosine is a potent inhibitor of ADSS, the rate limiting step of the PNC (Tyagi and Cooney, 1980, 1984). It dose-dependently reduced baseline OCR and SRC in *Famin*$^{p.254I}$ M0 macrophages (Figure 5G), without affecting non-mitochondrial respiration after antimycin A and rotenone inhibition of the electron transport chain (ETC) (Figure 5G). *L*-Alanosine also reduced baseline and oligomycin-elicited extracellular acidification rate (ECAR) in M0 macrophages (Figure 5G). Such reduction was also observed upon silencing *Adss*, *Adsl*, or the *Ampd*s (Figure S6C). *L*-Alanosine dose-dependently reduced OCR, SRC, and ECAR in HepG2 cells as well (Figure S6D). This coordinated reduction in OCR and ECAR demonstrated that the PNC was active in macrophages and HepG2 cells and controlled OXPHOS and glycolytic activity.

Figure 4. FAMIN Variants Impact on Central Purine Routing

(A) IMP levels in control and *FAMIN*-silenced HepG2 cells 24 h after transfection (n = 3).

(B) Inosine and hypoxanthine levels in control and *FAMIN*-silenced HepG2 cells 48 h after transfection (n = 6).

(C and D) Adenine, adenosine, (C) and ATP levels (D) in *Famin*$^{p.254I}$, *Famin*$^{p.254V}$, and *Famin*$^{p.284R}$ M1 macrophages (n = 12).

(E) Metabolic fate of [$^{13}C_{10}{}^{15}N_5$] adenosine after a 3-h pulse of M1 macrophages (n = 6; mean). Schematic representation of central purine metabolism. Adenosine deamination into inosine releases ^{15}N as ammonia, generating a [$^{13}C_{10}{}^{15}N_4$] isotopomer (brown). Phosphorolytic cleavage of inosine into hypoxanthine and [$^{13}C_5$] R1P, yielding the [$^{13}C_5{}^{15}N_4$] isotopomer (blue). Adenosine conversion to AMP without loss of label (purple). Phosphorolytic cleavage of fully labeled MTA generates [$^{13}C_5{}^{15}N_5$] adenine (green) and [$^{13}C_5$] 5′-methylthioribose-1-phosphate. Fractions of differently labeled states (averaged across *Famin*$^{p.254I}$, *Famin*$^{p.254V}$, and *Famin*$^{p.284R}$ genotypes) depicted as pie charts. ADA, adenosine deaminase; ADK, adenosine kinase; APRT, adenine phosphoribosyl transferase; HPRT, hypoxanthine-guanine phosphoribosyl transferase; MTAP, MTA phosphorylase; PNP, purine nucleoside phosphorlyase.

(F–H) Fraction of guanosine (F), guanine (G), or GTP (H) labeled as the indicated isotopomer in M1 macrophages after a [$^{13}C_1{}^{15}N_2$] guanosine pulse (n = 6).

(I) Metabolite levels (gray dots) in *Famin*$^{p.254I}$ versus *Famin*$^{p.284R}$ M1 macrophages depicted as volcano plot. False discovery rate (FDR)-controlled LC-MS features (black dots), select metabolites in red (n = 6).

(J) Immunoblots (IBs) with indicated antibodies in M1 macrophages (n = 3).

Data represented as mean ± SEM. *p < 0.05, **p < 0.01, and ***p < 0.001 (unpaired, two-tailed Student's t test or one-way ANOVA).

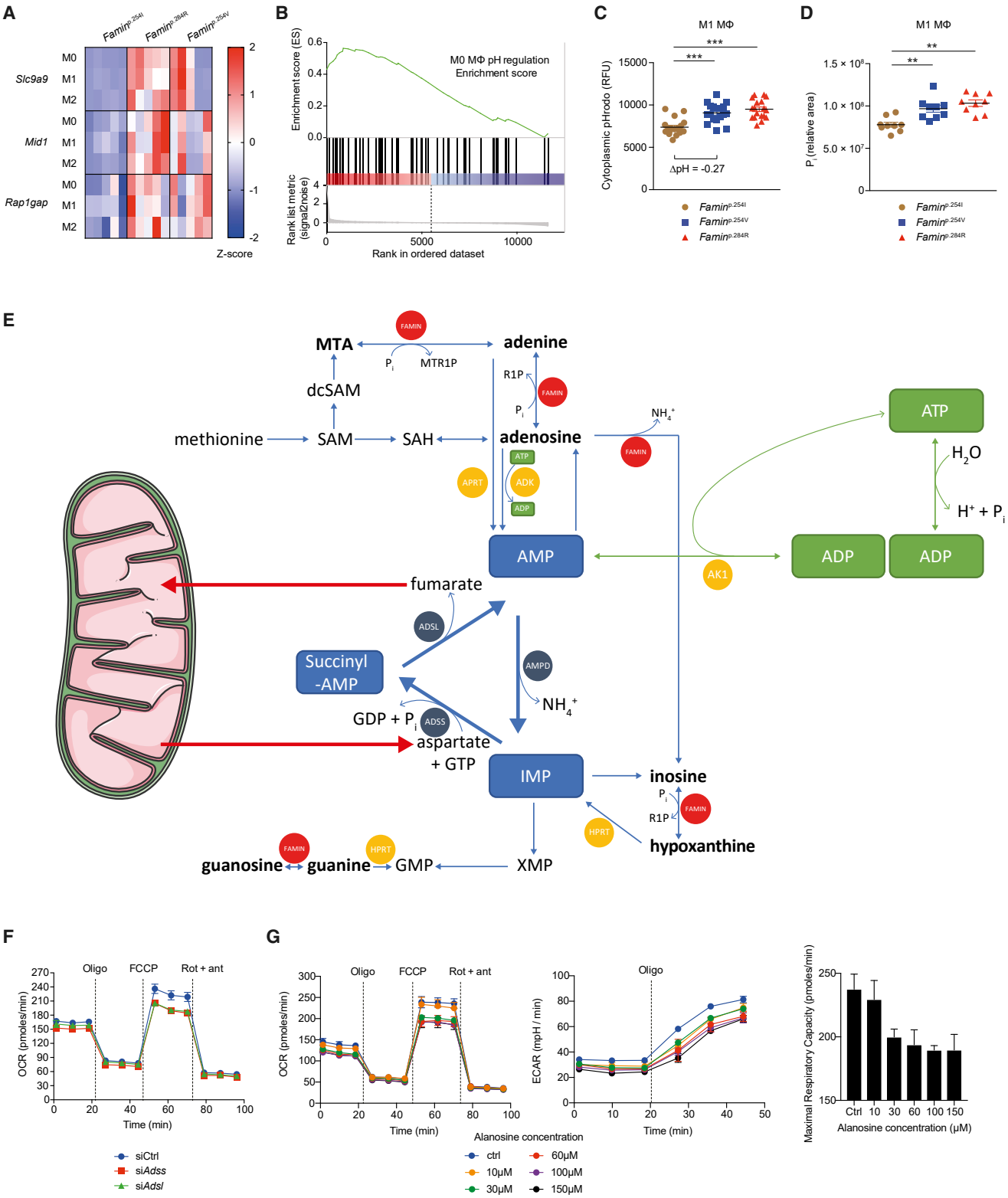

Figure 5. FAMIN Activity Controls Cellular pH and Enables a Purine Nucleotide Cycle

(A) Heatmap of differentially expressed genes by *Famin* genotype in M0, M1, and M2 macrophages (n = 5).

(B) Gene set enrichment analysis in *Famin*$^{p.254I}$ compared to *Famin*$^{p.284R}$ M0 macrophage transcriptomes; Gene Ontology pH regulation gene set (n = 5).

(legend continued on next page)

Flux through the Purine Nucleotide Cycle Requires FAMIN

During exhaustive muscle contraction, a fraction of IMP generated in the PNC may enter an "oxypurine" cycle through dephosphorylation to inosine (Figures 5E and 6A; Ipata and Pesi, 2018). By the oxypurine cycle, the purine ring may re-enter the PNC after salvage by PNP and HPRT, which is thought to retain the purine ring pool as nucleosides and nucleobases could efflux. FAMIN could support such a substrate cycle for inosine and additionally provide an entry point for AMP-derived adenosine with salvage routes by HPRT or directly by APRT (Figures 5E and 6A) and, thereby, promote flux through the PNC. As reported (Cader et al., 2016), baseline OCR, SRC, and ECAR were highest in *Famin*$^{p.254I}$, intermediate in *Famin*$^{p.254V}$, and lowest in *Famin*$^{p.284R}$ M0 macrophages (Figure 6B). *L*-Alanosine reduced levels of OCR, SRC, and ECAR in *Famin*$^{p.254I}$ and *Famin*$^{p.254V}$ M0 macrophages to levels in *Famin*$^{p.284R}$ cells, while not further reducing them in the latter (Figure 6B). *L*-Alanosine also curtailed ECAR in M1 macrophages, again only in those with active FAMIN (Figure 6C). Despite reducing glycolysis, *L*-alanosine acidified the cytoplasm in *Famin*$^{p.254I}$ and *Famin*$^{p.254V}$ M1 macrophages to the level of *Famin*$^{p.284R}$ cells, where *L*-alanosine did not further lower the pH_c (Figure 6D). Hence, FAMIN activity was essential for a PNC to ensue, which, in turn, controlled rates of OXPHOS and glycolysis and set the pH_c.

FAO and ACLY Facilitate the FAMIN-Dependent PNC in Macrophages

We next studied the aspartate supplying the PNC (Figure 6A). Uptake of [$^{15}N_2$] aspartate into M1 macrophages was negligible (data not shown), consistent with most cultured cells' reliance on *de novo* synthesis (Birsoy et al., 2015). Aspartate derives its carbons from oxaloacetate and its nitrogen from glutamate. Oxaloacetate can be generated from (1) malate by cytosolic or mitochondrial malate dehydrogenase, (2) pyruvate by mitochondrial pyruvate carboxylase, and (3) citrate by cytosolic ATP citrate lyase (ACLY) (Birsoy et al., 2015). A portion of cellular ACLY and FASN, with which FAMIN interacts (Cader et al., 2016), tethers to peroxisomes (Hillebrand et al., 2012). Higher OXPHOS and glycolytic activity in *Famin*$^{+/+}$ than *Famin*$^{-/-}$ macrophages required FAO and fatty acid synthesis (Cader et al., 2016). FAO-derived acetyl-CoA provides two carbons that combine with oxaloacetate to mitochondrial citrate, while ACLY cleaves citrate exported to the cytoplasm into oxaloacetate and acetyl-CoA that supplies fatty acid synthesis (Figure 6A). After a 3-h [$^{13}C_{16}$] palmitate pulse, 20%–30% of citrate was of the [$^{13}C_2$] isotopomer in M0 and M1 macrophages (Figure S7A), confirming both oxidise fatty acids. [$^{13}C_{16}$] Palmitate-pulsed M0 cells also exhibited isotopomers with >2 carbons labeled (Figure S7B), i.e., citrate that had undergone at least one full oxidation cycle. This allowed tracing the oxaloacetate carbons (Figure 6A). Fractional incorporation into aspartate after the [$^{13}C_{16}$] palmitate pulse was substantial (~30%) and higher in *Famin*$^{p.254I}$ and *Famin*$^{p.254V}$ than in *Famin*$^{p.284R}$ M0 macrophages (Figure 6E; Table S6). It was also higher into fumarate in *Famin*$^{p.254I}$ than in *Famin*$^{p.254V}$ and *Famin*$^{p.284R}$ M0 macrophages (Figure 6F; Table S6), with the fumarate:aspartate fractional labeling ratio highest in *Famin*$^{p.254I}$ cells (Figure S7C). SB-204990, a selective ACLY inhibitor (Granchi, 2018), indeed lowered OCR and ECAR most markedly in *Famin*$^{p.254I}$ and *Famin*$^{p.254V}$ M0 macrophages (Figure 6G). No citrate isotopomers beyond [$^{13}C_2$] were observed in M1 macrophages (Figure S7D), consistent with a tricarboxylic acid (TCA) cycle break after citrate (Jha et al., 2015), and accordingly, no [^{13}C] incorporation into aspartate and fumarate was detected (Figure S7D). Total citrate levels, however, were ~2-fold higher in *Famin*$^{p.254I}$ than in *Famin*$^{p.254V}$ and *Famin*$^{p.284R}$ M1 macrophages (Figure S7E). Altogether, these findings suggested that a seemingly futile cycle of FAO and fatty acid synthesis, also observed in other contexts (Yao et al., 2016), was involved in pulling TCA cycle oxaloacetate via ACLY into aspartate and through the PNC into fumarate.

Glucose was not a major carbon source for aspartate in M1 macrophages, with 1-h and 3-h [$^{13}C_6$] glucose pulses resulting in ~1.5% [$^{13}C_3$] aspartate (Figure S7F; Table S6). Glutamine, by glutamate (Birsoy et al., 2015; Sullivan et al., 2015), was an important source of *de novo* aspartate carbon, but with [^{13}C] aspartate after a 3-h [$^{13}C_5{}^{15}N_2$] glutamine pulse trending lower in *Famin*$^{p.254I}$ than *Famin*$^{p.284R}$ cells (Figure S7G; Table S6), it was unlikely to supply the PNC.

Fumarate Rescues an Impaired PNC

We finally asked whether the metabolic compromise due to impaired FAMIN can be rescued. Fumarate and malate, which can be taken up by plasma membrane transporters (Pajor, 2014), increased baseline OCR and SRC in HepG2 cells with *L*-alanosine-blocked PNC (Figure 7A). Fumarate and malate partially rescued baseline OCR and SRC in *FAMIN*- but not control-silenced HepG2 cells (Figure 7B). Exogenous fumarate partially rescued OCR and SRC in *Famin*$^{p.254V}$ and *Famin*$^{p.284R}$ M0 macrophages but did not augment respiration in *Famin*$^{p.254I}$ cells (Figure 7C). OXPHOS requires H^+ and P_i import into the mitochondrial matrix. Fumarate and malate completely rescued cytoplasmic acidification in *Famin*$^{p.254V}$ and *Famin*$^{p.284R}$ M0 macrophages; they attained a pH_c equivalent to untreated *Famin*$^{p.254I}$ cells, in which fumarate and malate did not affect

(C) Cytoplasmic pH measured by pHrodo in M1 macrophages (n = 18).
(D) Inorganic phosphate levels in M1 macrophages (n = 9).
(E) Schematic of the purine nucleotide cycle (PNC; blue boxes and circles) with phosphorolysis, deamination, and salvage routes involving FAMIN. AMPD, AMP deaminase; ADSS, adenylosuccinate synthase; ADSL, adenylosuccinate lyase; AK1, adenylate kinase.
(F) Oxygen consumption rate (OCR) of *Famin*$^{p.254I}$ M0 macrophages silenced for *Adsl* or *Adss* or transfected with siRNA control. Basal OCR followed by (dotted vertical lines) oligomycin A (Oligo), FCCP, and rotenone plus antimycin A (Rot + ant) (n = 3).
(G) OCR (left), extracellular acidification rate (ECAR) (middle), and maximal respiratory capacity (right) of *Famin*$^{p.254I}$ M0 macrophages treated with *L*-alanosine. (n = 3).
Data represented as mean ± SEM. *p < 0.05, **p < 0.01, and ***p < 0.001 (one-way ANOVA).

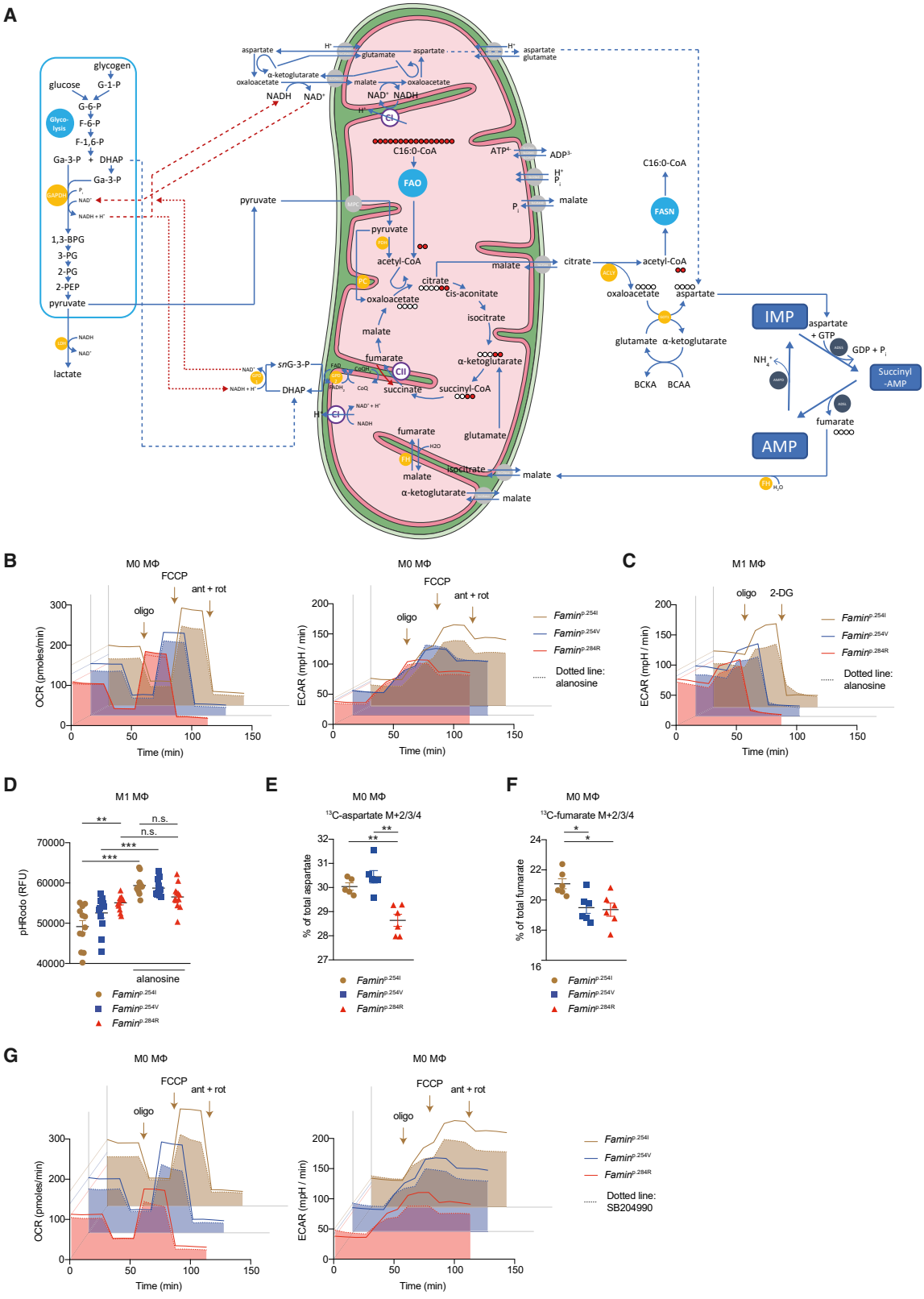

(legend on next page)

pH_c (Figures 7D and S7H). Fumarate and malate similarly rescued the acidic pH_c in *L*-alanosine-treated HepG2 cells (Figure S7I) and, remarkably, also in *Famin*$^{p.284R}$ M1 macrophages (Figure 7E), which are thought not to pursue OXPHOS (Mills et al., 2016). The mitochondrial ROS (mtROS) defect in *Famin*$^{p.254V}$ and *Famin*$^{p.284R}$ compared to *Famin*$^{p.254I}$ M1 macrophages, present despite unaltered mitochondrial biomass and membrane potential ($\Delta\Psi_m$) (Figures S7J and S7K), was also fully rescued by exogenous fumarate, whereas fumarate did not augment mtROS production in *Famin*$^{p.254I}$ cells (Figure 7F). Importantly, fumarate also rescued the glycolysis defect of *Famin*$^{p.254V}$ and *Famin*$^{p.284R}$ M0 macrophages, as revealed by increased baseline and oligomycin-elicited ECAR but did not augment ECAR in *Famin*$^{p.254I}$ cells (Figure 7C). Altogether, this was consistent with a FAMIN-dependent PNC sparking OXPHOS, increasing H^+ uptake into mitochondria, and promoting glycolysis.

A 3-h [$^{13}C_2$] fumarate pulse, at the concentration that rescued the metabolic compromise, labeled ~60% and ~30% of cellular fumarate in M0 and M1 cells, respectively, resulting in ~15% and ~30% of cellular malate labeled (Figures S7L and S7M). Notably, [^{13}C] did not incorporate into citrate in M0 and only labeled ~2% of citrate in M1 macrophages (Figure 7G), excluding direct anaplerosis. We detected, however, [$^{13}C_2$] succinate in M1 and, surprisingly, also in M0 cells (Figures 7H and S7N) and [$^{13}C_2$] aspartate also in both macrophage types (Figures 7I and S7O). We confirmed the generation of [$^{13}C_4$] succinate from fully labeled [$^{13}C_4$] fumarate in both M1 and M0 macrophages after a 24-h pulse (Figures 7J and 7K). This implied fumarate accepted electrons from coenzyme Q ($CoQH_2$) by a reverse succinate dehydrogenase (SDH; complex II) reaction, while conceivably increasing the capacity of the malate/aspartate shuttle (MAS). Reducing equivalents from glycolysis are imported into mitochondria by the MAS and the glycerol-3-phosphate shuttle (G3PS), thereby regenerating NAD^+ required for the glyceraldehyde 3-phosphate dehydrogenase (GAPDH) reaction (Figure 6A; Robergs et al., 2004). The MAS transfers electrons to mitochondrial NAD^+ before they enter the ETC, whereas the G3PS transfers them directly to CoQ (Mráček et al., 2013). The total cellular NAD^+/NADH ratio was gradually diminished from *Famin*$^{p.254I}$ by *Famin*$^{p.254V}$ to *Famin*$^{p.284R}$ M1 macrophages (Figure 7L). A 1-h [$^{13}C_6$] glucose pulse resulted in ~90% of hexose-6-phosphate present as the [$^{13}C_6$] isotopomer in *Famin*$^{p.254I}$ M1 macrophages, and this fraction was lower in *Famin*$^{p.254V}$ and *Famin*$^{p.284R}$ cells (Figure S7P), consistent with reduced glycolytic flux. At the same time, however, 55% of *sn*-glycerol-3-phosphate (*sn*G3P) exhibited [$^{13}C_3$] labeling in *Famin*$^{p.254I}$ cells, and this was strikingly ~10%–15% higher in *Famin*$^{p.254V}$ and *Famin*$^{p.284R}$ M1 macrophages (Figure 7M), which is indicative of a stalled GAPDH. *sn*G3P is the reduced form of the glycolysis intermediate dihydroxyacetone phosphate (DHAP) (Figure 6A), with which it forms the redox pair of the G3PS. *sn*G3P was among the top dysregulated metabolites in the unbiased survey (Figure 4I), with cellular levels higher in *Famin*$^{p.284R}$ cells than the genotypes with active FAMIN (Figure S7Q). Altogether, this demonstrated that the FAMIN-enabled PNC balances the redox interface between glycolysis and the mitochondrial ETC by the fumarate it generates.

DISCUSSION

Here, we report FAMIN as a prototype of a new family of multifunctional purine enzymes conserved from bacteria to man. FAMIN combines adenosine phosphorylase activity, previously thought to be absent from eukaryotic metabolism, with activities analogous to ADA, PNP, and MTAP. The latter three enzymes had been considered the sole routes supplying purine nucleotide salvage, ADA and adenosine kinase (ADK) the only routes of adenosine conversion, and MTAP the sole route of adenine generation (Albers, 2009; Boison, 2013; Camici et al., 2018; Kamatani and Carson, 1981). FAMIN enables a PNC that controls pH_c and redox state and sets the pace of mitochondrial and glycolytic activity.

Adenine and ribose are considered primordial metabolites from which life emerged from prebiotic chemistry (Ralser, 2018). The combination of key activities of adenyl metabolism in one single enzyme is intriguing. FAMIN's low catalytic rates appear disproportionate to its huge impact on cellular metabolism, possibly hinting to cofactors not present in our assays. Our YlmD structure identifies a single nucleoside-binding site, with the Cys^{125}-His^{80}-His^{142} triad, which is conserved across DUF152 proteins and FAMIN (residues Cys^{284}, His^{250}, and His^{301}), coordinating the ribose moiety of inosine. The structures

Figure 6. A FAMIN-Dependent PNC Controls Energy Metabolism

(A) Schematic of cellular energy metabolism in context of the PNC. PNC enzymes (blue circles), other enzymes (yellow circles), and transporters (gray circles) with gene names. Electron transfer from glycolysis to mitochondria by the glycerol-3-phosphate (G3PS; connected with red dotted lines) and malate-aspartate shuttle (MAS; connected with red dashed lines). Filled red circles depict fate of [$^{13}C_{16}$] palmitic acid (C16:0)-derived carbons through fatty acid oxidation (FAO) into tricarboxylic acid (TCA) cycle citrate and by ATP citrate lyase (ACLY) into fatty acid synthesis (FASN); empty circles depict route of carbons from TCA oxaloacetate; labeling of α-ketoglutarate and succinyl-CoA depicted for M0 macrophages with intact TCA cycle. Complex II (CII) forward and reverse activity, blue and red arrowed arcs, respectively. CoQ, coenzyme Q; CI, complex I; branched chain amino and keto acids (BCAA, BCKA); DHAP, dihydroxyacetone phosphate; G-6-P, glucose-6-phosphate; F-6-P, fructose-6-phosphate; F-1,6-P, fructose-1,6-bisphosphate; Ga-3-P, glyceraldehyde-3-phosphate; 1,3-BPG, 1,3-bis-phosphoglycerate; 3-PG, 3-phosphoglycerate; 2-PG, 2-phosphoglycerate; 2-PEP, 2-phosphoenolpyruvate.

(B) OCR (left) and ECAR (right) of M0 macrophages treated (dotted line + fill) with *L*-alanosine for 3 h or vehicle (solid line). Basal OCR and ECAR followed by (arrows) oligomycin A (Oligo), FCCP, and rotenone plus antimycin A (Rot + ant) (n = 3).

(C) ECAR of M1 macrophages treated (dotted line + fill) with *L*-alanosine or vehicle (solid line). Basal ECAR followed by (arrows) Oligo and 2-deoxyglucose (2-DG) (n = 3).

(D) Cytoplasmic pH (pH_c) measured using pHrodo in M1 macrophages treated with *L*-alanosine or vehicle (n = 12 from 3 mice per genotype).

(E and F) Fraction of aspartate (E) or fumarate (F) labeled as the indicated isotopomer in M0 macrophages after a [$^{13}C_{16}$] palmitate pulse (n = 6). (G) OCR (left) and ECAR (right) of M0 macrophages treated (dotted line + fill) with SB204990 (ACLY inhibitor) or vehicle (solid line). (n = 3).

Data represented as mean ± SEM. *p < 0.05, **p < 0.01, and ***p < 0.001 (one-way ANOVA).

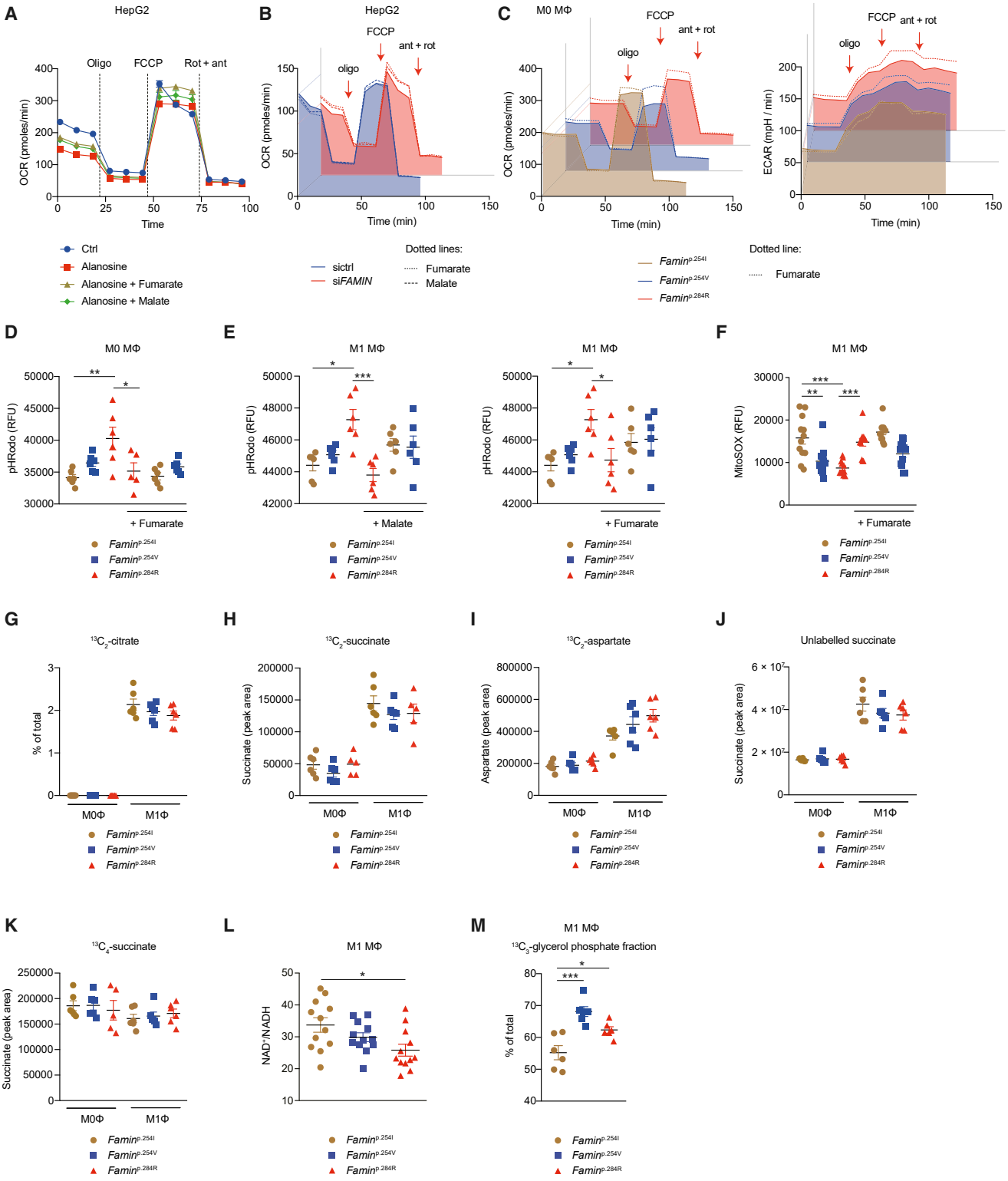

Figure 7. Fumarate Rescues the Impaired FAMIN-Dependent PNC

(A) OCR of HepG2 cells treated with *L*-alanosine or vehicle and supplemented with fumarate or malate. Basal OCR followed by (dotted lines) Oligo, FCCP, and Rot + ant (n = 6).

(B) OCR of control and *FAMIN*-silenced HepG2 cells treated with fumarate (dotted line), malate (dashed line), or vehicle control (solid line + fill). (n = 6).

(legend continued on next page)

of DUF152 proteins suggest one single active site (Kim et al., 2006). The fold and active site architecture of YlmD and DUF152 are unrelated to those of purine and pyrimidine amidohydrolases, such as ADA, and of phosphorolytic enzymes (Appleby et al., 1999; Ealick et al., 1990; Kim et al., 2006; Wilson et al., 1991). A select few examples of enzymes have been described that catalyze at a single active site chemically distinct, physiologically utilized reactions. They were mostly discovered in bacteria with reduced genomes and may be reminiscent of long-extinct early cellular life that was likely much simpler, with few low activity enzymes performing multiple functions (Ferla et al., 2017; Say and Fuchs, 2010; Seelig, 2017). It is tempting to speculate that FAMIN and its antecedents may offer a glimpse into the ancient past, with its control over metabolic pace by redox state and pH. The pattern of FAMIN orthologs across species may suggest horizontal gene transfer. Orthologs are restricted to chordates within eukaryotes and to prokaryotic phyla typically present in the intestinal microbiota, an ecological niche of minuscule oxygen tension. The I254V variation is also an important difference between human and mouse, with C57BL/6 mice expressing *Famin*$^{p.254V}$.

A PNC has not previously been reported in cells of the immune system. Lowenstein and colleagues first demonstrated a PNC, geared to stabilize an exercising muscle cell's "energy charge" and releasing ammonia proportionate to work (Embden and Wassermeyer, 1928; Lowenstein and Tornheim, 1971; Lowenstein, 1972, 1990; van Waarde, 1988). Inhibiting ADSS prevented the increase in TCA cycle intermediates during exercise, while not affecting levels at rest (Aragón and Lowenstein, 1980; Lowenstein, 1990; van Waarde, 1988). By funneling their amino nitrogen into the PNC, e.g., branched chain amino acids (BCAAs) become accessible to oxidation and carboxylation and, thereby, contribute to muscle anaplerosis (Arinze, 2005; Lowenstein, 1972, 1990). The promotion of glycolysis has also been linked to the muscle PNC, albeit the mechanism remained unclear (Lowenstein, 1972; Sugden and Newsholme, 1975; van Waarde, 1988). A PNC in macrophages ensues only when FAMIN is active, as ADSS inhibition reduced OXPHOS, glycolysis, and pH_c to levels identical to those in FAMIN-deficient cells and no further in them. Interestingly, fumarate (and malate) rescued the acidic pH_c and the depressed mtROS production of FAMIN-deficient cells completely but the compromised OXPHOS and glycolysis only partially. No augmentation by exogenous fumarate occurred in cells with fully active FAMIN. Exogenous fumarate might not rescue processes feeding into aspartate entering the PNC, as exemplified by BCAA contributing to anaplerosis in muscle. The fumarate rescue itself entails substantial complexity, with mitochondrial import after hydration to malate by electroneutral transporters that exchange malate for α-ketoglutarate (part of the MAS), citrate (supplying ACLY), or phosphate (Palmieri, 2004, 2013) and electrogenic exchange of aspartate$^-$ for glutamate$^-$ + H^+ (as part of the MAS). Mitochondrial H^+ import occurs by the MAS and the G3PS, P_i/H^+ symport and cation exchange mechanisms (Robergs et al., 2004), hence, rectifying an imbalance in mitochondrial electron import by exogenous fumarate may directly rescue cytoplasmic acidosis.

Our data indeed suggest that PNC-supplied fumarate synchronizes mitochondrial activity with glycolysis by balancing electron transfer into mitochondria between the G3PS and MAS. Although both shuttles are likely affected, we favor a model where the primary redox perturbation in FAMIN-impaired macrophages arises from the G3PS. Specifically, glycolysis-derived electrons transferred by the G3PS to CoQ may be accepted by PNC-derived fumarate to form succinate (Figure 6A). In the absence of fumarate as (terminal) electron acceptor, mitochondrial superoxide production collapses, *sn*G3P accumulates, NADH is not recycled to NAD^+, and GAPDH stalls. GPD2, the ETC *sn*G3P dehydrogenase, which is the rate-limiting enzyme of the G3PS, can generate high levels of mtROS (Mráček et al., 2013, 2014), although mtROS could also arise from complex II or I (Chouchani et al., 2016; Langston et al., 2019; Mills et al., 2016). Such a model is particularly pertinent for M1 macrophages, which engage little OXPHOS with low (though not absent) oxygen consumption (Jha et al., 2015; Mills et al., 2016). Reverse SDH/complex II activity with succinate accumulation occurs in ischemic murine heart (Chouchani et al., 2014) and has been invoked for mtROS production in M1 macrophages (Mills et al., 2016), which is dependent on electron import by GPD2 (Langston et al., 2019). Succinate, complex II, and GPD2 are critical for interleukin-1β (IL-1β) secretion from M1 macrophages (Langston et al., 2019; Mills et al., 2016; Tannahill et al., 2013), a cytokine important in both CD and Still's disease (Ruperto et al., 2012; Uhlig and Powrie, 2018). Observing [$^{13}C_4$] succinate in [$^{13}C_4$] fumarate-pulsed M0 macrophages was surprising and controversially points toward a (small) fraction of SDH/complex II operating in reverse in parallel with its forward reaction in the TCA and ETC. Supporting fumarate respiration, present in many microaerophiles and anaerobes (Cook et al., 2014; Kröger et al., 1992), might be the evolutionary context of DUF152 proteins. It will be interesting to explore whether such parallel reverse SDH activity exists in mammalian cells and what the spatial basis is.

In summary, FAMIN and its orthologs rewrite core purine metabolism by revealing a surprising new layer of adenyl

(C) OCR (left) and ECAR (right) of M0 macrophages treated with fumarate (dotted line) or vehicle (solid line + fill) for 8 h. (n = 3).
(D and E) pH_c measured using pHrodo in M0 (D) or M1 macrophages (E) treated with malate, fumarate, or vehicle. Right and left panel of (E) share same control group (n = 6).
(F) Mitochondrial superoxide measured using mitoSOX in M1 macrophages treated with fumarate or vehicle (n = 12).
(G–J) Labeling of citrate (G), succinate (H, J, and K), and aspartate (I) in M0 and M1 macrophages after a [$^{13}C_2$] fumarate (G–I) or [$^{13}C_4$] fumarate pulse (J and K) (n = 6).
(L) NAD^+/NADH ratio in M1 macrophages (n = 12).
(M) Fractional labeling of *sn*G-3-P in M1 macrophages after a [$^{13}C_6$] glucose pulse (n = 6).
Data represented as mean ± SEM. *p < 0.05, **p < 0.01, and ***p < 0.001 (one-way ANOVA).

turnover. Even prior to this discovery, adenyl metabolism had been considered the most highly interconnected and exquisitely tuned metabolic circuitry in prokaryotes and eukaryotes.

STAR★METHODS

Detailed methods are provided in the online version of this paper and include the following:

- KEY RESOURCES TABLE
- LEAD CONTACT AND MATERIALS AVAILABILITY
- EXPERIMENTAL MODEL AND SUBJECT DETAILS
  - Mice
  - Cell lines
  - Murine bone marrow-derived macrophage
- METHOD DETAILS
  - Plasmids
  - Mammalian expression and purification of FAMIN
  - Prokaryotic expression and purification of MBP-FAMIN fusion proteins
  - Expression and Purification of YlmD and YfiH
  - Crystallization and crystallographic structure determination of YlmD
  - Extraction of aqueous metabolites
  - LC-MS sample preparation
  - LC-MS analysis of aqueous metabolites
  - LC-MS data processing
  - Enzyme assays
  - Laccase assay
  - Intracellular pH assay
  - Oxygen consumption rate and extracellular acidification rate
  - Transfection of siRNA into HepG2 cells
  - RNA extraction and sequencing
  - Phylogenetic analysis of FAMIN orthologs
  - Immunoblot
  - Mitochondrial ROS
  - Mitochondrial membrane potential and biomass
  - Cell proliferation assay
- QUANTIFICATION AND STATISTICAL ANALYSIS
- DATA AND CODE AVAILABILITY

SUPPLEMENTAL INFORMATION

Supplemental Information can be found online at https://doi.org/10.1016/j.cell.2019.12.017.

ACKNOWLEDGMENTS

We thank R.S. Blumberg and K.J. Patel for discussions and L.M. Holland, O.S. Ojo, and N. Kumar for experimental support. This work was supported by the Wellcome Trust (106260/Z/14/Z, A.K.; 101908/Z/13/Z and 217191/Z/19/Z, Y.M.; 103077/Z/13/Z, N.C.K.; and 105920/Z/14/Z, J.C.L.), the European Research Council (grants 648889 and 260961, A.K.), the Academy of Medical Sciences (SGL018\1119, M.Z.C.), the Medical Research Council (MRC; MR/P011705/1, MC_UP_A090_1006, and MR/P01836X/1, J.L.G.), the National Council for Scientific and Technological Development, Brazil (201664/2014-3, R.P.d.A.R.), the Malaysian Ministry of Higher Education Scholarship Programme (MARA330408277134, M.N.M.-I.), the German Research Foundation (HA 7731/1-1, L.-M.H.; ExC Precision Medicine in Chronic Inflammation and CRC1182, P.R.), and the European Union (H2020 SYSCID 733100, P.R.). Crystallographic data were collected on beamlines I04 and I03 at Diamond Light Source (DLS), with access (proposal MX15916) supported by the Wellcome Trust, MRC, and BBSRC. We thank the NIHR Cambridge BRC for infrastructural support.

AUTHOR CONTRIBUTIONS

M.Z.C., R.P.d.A.R., and J.A.W., together with G.W.S., S.R., K.R., L.-M.H., S.S., and N.C.K., performed experiments; M.Z.C., M.N.M.-I., S.R., G.S., L.W.U., A.B.I.-R., and Y.M. designed constructs and purified recombinant protein; J.A.W. and J.L.G. provided LC-MS and method development; S.R. and Y.M. determined and analyzed crystal structures; T.D.L. provided phylogenetic analysis and, together with G.D. and A.B., helped generate genetic tools; L.-M.H., J.-F.E., P.R., and J.C.L. performed RNA-seq; and A.K. devised the study and, together with M.Z.C. and input from all authors, coordinated the project, designed experiments, analyzed and interpreted data, and wrote the manuscript.

DECLARATION OF INTERESTS

The University of Cambridge has filed patent applications relating to this work. The authors declare no other competing financial interests.

Received: February 11, 2019
Revised: November 18, 2019
Accepted: December 12, 2019
Published: January 23, 2020; corrected online: February 5, 2020

REFERENCES

Adams, P.D., Afonine, P.V., Bunkóczi, G., Chen, V.B., Davis, I.W., Echols, N., Headd, J.J., Hung, L.W., Kapral, G.J., Grosse-Kunstleve, R.W., et al. (2010). PHENIX: a comprehensive Python-based system for macromolecular structure solution. Acta Crystallogr. D Biol. Crystallogr. *66*, 213–221.

Albers, E. (2009). Metabolic characteristics and importance of the universal methionine salvage pathway recycling methionine from 5′-methylthioadenosine. IUBMB Life *61*, 1132–1142.

Appleby, T.C., Erion, M.D., and Ealick, S.E. (1999). The structure of human 5′-deoxy-5′-methylthioadenosine phosphorylase at 1.7 A resolution provides insights into substrate binding and catalysis. Structure *7*, 629–641.

Aragón, J.J., and Lowenstein, J.M. (1980). The purine-nucleotide cycle. Comparison of the levels of citric acid cycle intermediates with the operation of the purine nucleotide cycle in rat skeletal muscle during exercise and recovery from exercise. Eur. J. Biochem. *110*, 371–377.

Arinze, I.J. (2005). Facilitating understanding of the purine nucleotide cycle and the one-carbon pool: Part I: The purine nucleotide cycle. Biochem. Mol. Biol. Educ. *33*, 165–168.

Ashihara, H., Stasolla, C., Fujimura, T., and Crozier, A. (2018). Purine salvage in plants. Phytochemistry *147*, 89–124.

Assadi, G., Vesterlund, L., Bonfiglio, F., Mazzurana, L., Cordeddu, L., Schepis, D., Mjösberg, J., Ruhrmann, S., Fabbri, A., Vukojevic, V., et al. (2016). Functional Analyses of the Crohn's Disease Risk Gene LACC1. PLoS One *11*, e0168276.

Beloqui, A., Pita, M., Polaina, J., Martínez-Arias, A., Golyshina, O.V., Zumárraga, M., Yakimov, M.M., García-Arellano, H., Alcalde, M., Fernández, V.M., et al. (2006). Novel polyphenol oxidase mined from a metagenome expression library of bovine rumen: biochemical properties, structural analysis, and phylogenetic relationships. J. Biol. Chem. *281*, 22933–22942.

Birsoy, K., Wang, T., Chen, W.W., Freinkman, E., Abu-Remaileh, M., and Sabatini, D.M. (2015). An Essential Role of the Mitochondrial Electron Transport Chain in Cell Proliferation Is to Enable Aspartate Synthesis. Cell *162*, 540–551.

Boison, D. (2013). Adenosine kinase: exploitation for therapeutic gain. Pharmacol. Rev. *65*, 906–943.

Bzowska, A., Kulikowska, E., and Shugar, D. (2000). Purine nucleoside phosphorylases: properties, functions, and clinical aspects. Pharmacol. Ther. *88*, 349–425.

Cader, M.Z., Boroviak, K., Zhang, Q., Assadi, G., Kempster, S.L., Sewell, G.W., Saveljeva, S., Ashcroft, J.W., Clare, S., Mukhopadhyay, S., et al. (2016). C13orf31 (FAMIN) is a central regulator of immunometabolic function. Nat. Immunol. *17*, 1046–1056.

Camici, M., Allegrini, S., and Tozzi, M.G. (2018). Interplay between adenylate metabolizing enzymes and AMP-activated protein kinase. FEBS J. *285*, 3337–3352.

Casey, J.R., Grinstein, S., and Orlowski, J. (2010). Sensors and regulators of intracellular pH. Nat. Rev. Mol. Cell Biol. *11*, 50–61.

Chen, V.B., Arendall, W.B., III, Headd, J.J., Keedy, D.A., Immormino, R.M., Kapral, G.J., Murray, L.W., Richardson, J.S., and Richardson, D.C. (2010). MolProbity: all-atom structure validation for macromolecular crystallography. Acta Crystallogr. D Biol. Crystallogr. *66*, 12–21.

Chouchani, E.T., Pell, V.R., Gaude, E., Aksentijević, D., Sundier, S.Y., Robb, E.L., Logan, A., Nadtochiy, S.M., Ord, E.N.J., Smith, A.C., et al. (2014). Ischaemic accumulation of succinate controls reperfusion injury through mitochondrial ROS. Nature *515*, 431–435.

Chouchani, E.T., Pell, V.R., James, A.M., Work, L.M., Saeb-Parsy, K., Frezza, C., Krieg, T., and Murphy, M.P. (2016). A Unifying Mechanism for Mitochondrial Superoxide Production during Ischemia-Reperfusion Injury. Cell Metab. *23*, 254–263.

Cook, G.M., Greening, C., Hards, K., and Berney, M. (2014). Energetics of pathogenic bacteria and opportunities for drug development. Adv. Microb. Physiol. *65*, 1–62.

Della Ragione, F., Takabayashi, K., Mastropietro, S., Mercurio, C., Oliva, A., Russo, G.L., Della Pietra, V., Borriello, A., Nobori, T., Carson, D.A., and Zappia, V. (1996). Purification and characterization of recombinant human 5′-methylthioadenosine phosphorylase: definite identification of coding cDNA. Biochem. Biophys. Res. Commun. *223*, 514–519.

Ealick, S.E., Rule, S.A., Carter, D.C., Greenhough, T.J., Babu, Y.S., Cook, W.J., Habash, J., Helliwell, J.R., Stoeckler, J.D., Parks, R.E., Jr., et al. (1990). Three-dimensional structure of human erythrocytic purine nucleoside phosphorylase at 3.2 A resolution. J. Biol. Chem. *265*, 1812–1820.

Embden, G., and Wassermeyer, H. (1928). Über die Bedeutung der Adenylsäure für die Muskelfunktion. 5. Die Quelle des bei der Kontraktion gebildeten Ammoniaks. Hoppe Seylers Z. Physiol. Chem. *179*, 226–237.

Emsley, P., and Cowtan, K. (2004). Coot: model-building tools for molecular graphics. Acta Crystallogr. D Biol. Crystallogr. *60*, 2126–2132.

Ferla, M.P., Brewster, J.L., Hall, K.R., Evans, G.B., and Patrick, W.M. (2017). Primordial-like enzymes from bacteria with reduced genomes. Mol. Microbiol. *105*, 508–524.

Folch, J., Lees, M., and Sloane Stanley, G.H. (1957). A simple method for the isolation and purification of total lipides from animal tissues. J. Biol. Chem. *226*, 497–509.

Friedkin, M., and Kalckar, H.M. (1961). The Enzymes (Academic Press), p. 245.

Giblett, E.R., Anderson, J.E., Cohen, F., Pollara, B., and Meuwissen, H.J. (1972). Adenosine-deaminase deficiency in two patients with severely impaired cellular immunity. Lancet *2*, 1067–1069.

Giblett, E.R., Ammann, A.J., Wara, D.W., Sandman, R., and Diamond, L.K. (1975). Nucleoside-phosphorylase deficiency in a child with severely defective T-cell immunity and normal B-cell immunity. Lancet *1*, 1010–1013.

Gorshkov, V., Tarasova, N., Gogoleva, N., Osipova, E., Petrova, O., Kovtunov, E., and Gogolev, Y. (2017). Polyphenol oxidase from *Pectobacterium atrosepticum*: identification and cloning of gene and characteristics of the enzyme. J. Basic Microbiol. *57*, 998–1009.

Granchi, C. (2018). ATP citrate lyase (ACLY) inhibitors: An anti-cancer strategy at the crossroads of glucose and lipid metabolism. Eur. J. Med. Chem. *157*, 1276–1291.

Hillebrand, M., Gersting, S.W., Lotz-Havla, A.S., Schäfer, A., Rosewich, H., Valerius, O., Muntau, A.C., and Gärtner, J. (2012). Identification of a new fatty acid synthesis-transport machinery at the peroxisomal membrane. J. Biol. Chem. *287*, 210–221.

Ipata, P.L., and Pesi, R. (2018). Metabolic interaction between purine nucleotide cycle and oxypurine cycle during skeletal muscle contraction of different intensities: a biochemical reappraisal. Metabolomics *14*, 42.

Ipata, P.L., Camici, M., Micheli, V., and Tozz, M.G. (2011). Metabolic network of nucleosides in the brain. Curr. Top. Med. Chem. *11*, 909–922.

Jha, A.K., Huang, S.C., Sergushichev, A., Lampropoulou, V., Ivanova, Y., Loginicheva, E., Chmielewski, K., Stewart, K.M., Ashall, J., Everts, B., et al. (2015). Network integration of parallel metabolic and transcriptional data reveals metabolic modules that regulate macrophage polarization. Immunity *42*, 419–430.

Kamatani, N., and Carson, D.A. (1981). Dependence of adenine production upon polyamine synthesis in cultured human lymphoblasts. Biochim. Biophys. Acta *675*, 344–350.

Kim, Y., Maltseva, N., Dementieva, I., Collart, F., Holzle, D., and Joachimiak, A. (2006). Crystal structure of hypothetical protein YfiH from Shigella flexneri at 2 A resolution. Proteins *63*, 1097–1101.

Kim, D., Langmead, B., and Salzberg, S.L. (2015). HISAT: a fast spliced aligner with low memory requirements. Nat. Methods *12*, 357–360.

Kröger, A., Geisler, V., Lemma, E., Theis, F., and Lenger, R. (1992). Bacterial fumarate respiration. Arch. Microbiol. *158*, 311–314.

Kryukov, G.V., Wilson, F.H., Ruth, J.R., Paulk, J., Tsherniak, A., Marlow, S.E., Vazquez, F., Weir, B.A., Fitzgerald, M.E., Tanaka, M., et al. (2016). MTAP deletion confers enhanced dependency on the PRMT5 arginine methyltransferase in cancer cells. Science *351*, 1214–1218.

Lahiri, A., Hedl, M., Yan, J., and Abraham, C. (2017). Human LACC1 increases innate receptor-induced responses and a LACC1 disease-risk variant modulates these outcomes. Nat. Commun. *8*, 15614.

Landgraf, B.J., McCarthy, E.L., and Booker, S.J. (2016). Radical S-Adenosylmethionine Enzymes in Human Health and Disease. Annu. Rev. Biochem. *85*, 485–514.

Langston, P.K., Nambu, A., Jung, J., Shibata, M., Aksoylar, H.I., Lei, J., Xu, P., Doan, M.T., Jiang, H., MacArthur, M.R., et al. (2019). Glycerol phosphate shuttle enzyme GPD2 regulates macrophage inflammatory responses. Nat. Immunol. *20*, 1186–1195.

Lin, S.C., and Hardie, D.G. (2018). AMPK: Sensing Glucose as well as Cellular Energy Status. Cell Metab. *27*, 299–313.

Lindley, E.R., and Pisoni, R.L. (1993). Demonstration of adenosine deaminase activity in human fibroblast lysosomes. Biochem. J. *290*, 457–462.

Lowenstein, J.M. (1972). Ammonia production in muscle and other tissues: the purine nucleotide cycle. Physiol. Rev. *52*, 382–414.

Lowenstein, J.M. (1990). The purine nucleotide cycle revisited [corrected]. Int. J. Sports Med. *11*, S37–S46.

Lowenstein, J., and Tornheim, K. (1971). Ammonia production in muscle: the purine nucleotide cycle. Science *171*, 397–400.

Maynes, J.T., Yam, W., Jenuth, J.P., Gang Yuan, R., Litster, S.A., Phipps, B.M., and Snyder, F.F. (1999). Design of an adenosine phosphorylase by active-site modification of murine purine nucleoside phosphorylase. Enzyme kinetics and molecular dynamics simulation of Asn-243 and Lys-244 substitutions of purine nucleoside phosphorylase. Biochem. J. *344*, 585–592.

McCoy, A.J., Grosse-Kunstleve, R.W., Adams, P.D., Winn, M.D., Storoni, L.C., and Read, R.J. (2007). Phaser crystallographic software. J. Appl. Cryst. *40*, 658–674.

Mills, E.L., Kelly, B., Logan, A., Costa, A.S.H., Varma, M., Bryant, C.E., Tourlomousis, P., Dabritz, J.H.M., Gottlieb, E., Latorre, I., et al. (2016). Succinate Dehydrogenase Supports Metabolic Repurposing of Mitochondria to Drive Inflammatory Macrophages. Cell *167*, 457–470.e413.

Mráček, T., Drahota, Z., and Houštěk, J. (2013). The function and the role of the mitochondrial glycerol-3-phosphate dehydrogenase in mammalian tissues. Biochim. Biophys. Acta *1827*, 401–410.

Mráček, T., Holzerová, E., Drahota, Z., Kovářová, N., Vrbacký, M., Ješina, P., and Houštěk, J. (2014). ROS generation and multiple forms of mammalian mitochondrial glycerol-3-phosphate dehydrogenase. Biochim. Biophys. Acta *1837*, 98–111.

Murray, A.W. (1971). The biological significance of purine salvage. Annu. Rev. Biochem. *40*, 811–826.

O'Neill, L.A., and Pearce, E.J. (2016). Immunometabolism governs dendritic cell and macrophage function. J. Exp. Med. *213*, 15–23.

Otwinowski, Z., and Minor, W. (1997). Processing of X-ray Diffraction Data Collected in Oscillation Mode. Methods Enzymol. *276*, 307–326.

Pajor, A.M. (2014). Sodium-coupled dicarboxylate and citrate transporters from the SLC13 family. Pflugers Arch. *466*, 119–130.

Palmieri, F. (2004). The mitochondrial transporter family (SLC25): physiological and pathological implications. Pflugers Arch. *447*, 689–709.

Palmieri, F. (2013). The mitochondrial transporter family SLC25: identification, properties and physiopathology. Mol. Aspects Med. *34*, 465–484.

Perna, V., Agger, J.W., Holck, J., and Meyer, A.S. (2018). Multiple Reaction Monitoring for quantitative laccase kinetics by LC-MS. Sci. Rep. *8*, 8114.

Prosser, G.A., Larrouy-Maumus, G., and de Carvalho, L.P. (2014). Metabolomic strategies for the identification of new enzyme functions and metabolic pathways. EMBO Rep. *15*, 657–669.

Ralser, M. (2018). An appeal to magic? The discovery of a non-enzymatic metabolism and its role in the origins of life. Biochem. J. *475*, 2577–2592.

Robergs, R.A., Ghiasvand, F., and Parker, D. (2004). Biochemistry of exercise-induced metabolic acidosis. Am. J. Physiol. Regul. Integr. Comp. Physiol. *287*, R502–R516.

Ruperto, N., Brunner, H.I., Quartier, P., Constantin, T., Wulffraat, N., Horneff, G., Brik, R., McCann, L., Kasapcopur, O., Rutkowska-Sak, L., et al.; PRINTO; PRCSG (2012). Two randomized trials of canakinumab in systemic juvenile idiopathic arthritis. N. Engl. J. Med. *367*, 2396–2406.

Say, R.F., and Fuchs, G. (2010). Fructose 1,6-bisphosphate aldolase/phosphatase may be an ancestral gluconeogenic enzyme. Nature *464*, 1077–1081.

Seelig, B. (2017). Multifunctional enzymes from reduced genomes - model proteins for simple primordial metabolism? Mol. Microbiol. *105*, 505–507.

Skon-Hegg, C., Zhang, J., Wu, X., Sagolla, M., Ota, N., Wuster, A., Tom, J., Doran, E., Ramamoorthi, N., Caplazi, P., et al. (2019). LACC1 Regulates TNF and IL-17 in Mouse Models of Arthritis and Inflammation. J. Immunol. *202*, 183–193.

Slepkov, E.R., Rainey, J.K., Sykes, B.D., and Fliegel, L. (2007). Structural and functional analysis of the Na+/H+ exchanger. Biochem. J. *401*, 623–633.

Sugden, P.H., and Newsholme, E.A. (1975). The effects of ammonium, inorganic phosphate and potassium ions on the activity of phosphofructokinases from muscle and nervous tissues of vertebrates and invertebrates. Biochem. J. *150*, 113–122.

Sullivan, L.B., Gui, D.Y., Hosios, A.M., Bush, L.N., Freinkman, E., and Vander Heiden, M.G. (2015). Supporting Aspartate Biosynthesis Is an Essential Function of Respiration in Proliferating Cells. Cell *162*, 552–563.

Tannahill, G.M., Curtis, A.M., Adamik, J., Palsson-McDermott, E.M., McGettrick, A.F., Goel, G., Frezza, C., Bernard, N.J., Kelly, B., Foley, N.H., et al. (2013). Succinate is an inflammatory signal that induces IL-1β through HIF-1α. Nature *496*, 238–242.

Tickle, I.J., Flensburg, C., Keller, P., Paciorek, W., Sharff, A., Vonrhein, C., and Bricogne, G. (2018). STARANISO (Global Phasing Ltd).

Tyagi, A.K., and Cooney, D.A. (1980). Identification of the antimetabolite of L-alanosine, L-alanosyl-5-amino-4-imidazolecarboxylic acid ribonucleotide, in tumors and assessment of its inhibition of adenylosuccinate synthetase. Cancer Res. *40*, 4390–4397.

Tyagi, A.K., and Cooney, D.A. (1984). Biochemical pharmacology, metabolism, and mechanism of action of L-alanosine, a novel, natural antitumor agent. Adv. Pharmacol. Chemother. *20*, 69–121.

Uhlig, H.H., and Powrie, F. (2018). Translating Immunology into Therapeutic Concepts for Inflammatory Bowel Disease. Annu. Rev. Immunol. *36*, 755–781.

van Waarde, A. (1988). Operation of the purine nucleotide cycle in animal tissues. Biol. Rev. Camb. Philos. Soc. *63*, 259–298.

Vonrhein, C., Flensburg, C., Keller, P., Sharff, A., Smart, O., Paciorek, W., Womack, T., and Bricogne, G. (2011). Data processing and analysis with the autoPROC toolbox. Acta Crystallogr. D Biol. Crystallogr. *67*, 293–302.

Wilson, D.K., Rudolph, F.B., and Quiocho, F.A. (1991). Atomic structure of adenosine deaminase complexed with a transition-state analog: understanding catalysis and immunodeficiency mutations. Science *252*, 1278–1284.

Yao, C.H., Fowle-Grider, R., Mahieu, N.G., Liu, G.Y., Chen, Y.J., Wang, R., Singh, M., Potter, G.S., Gross, R.W., Schaefer, J., et al. (2016). Exogenous Fatty Acids Are the Preferred Source of Membrane Lipids in Proliferating Fibroblasts. Cell Chem. Biol. *23*, 483–493.

Zimmerman, T.P., Gersten, N.B., Ross, A.F., and Miech, R.P. (1971). Adenine as substrate for purine nucleoside phosphorylase. Can. J. Biochem. *49*, 1050–1054.

STAR★METHODS

KEY RESOURCES TABLE

REAGENT or RESOURCE	SOURCE	IDENTIFIER
Antibodies		
PNP (H-7) (monoclonal)	Santa Cruz Biotechnology	Cat#sc-36508; RRID:AB_10845931
MTAP (42-T) (monoclonal)	Santa Cruz Biotechnology	Cat#sc-100782; RRID:AB_2147095
ADA (D-4) (monoclonal)	Santa Cruz Biotechnology	Cat#sc-28346; RRID:AB_626634
LACC1/FAMIN (E-12) (monoclonal)	Santa Cruz Biotechnology	Cat#sc-376231
ADA (polyclonal)	Novus Biologicals	Cat#NBP1-87404; RRID:AB_11025679
Beta-Actin, unconjugated, (13E5) (monoclonal)	Cell Signaling Technology	Cat#4970; RRID:AB_2223172
Beta-Actin, HRP Conjugated, (13E5) (monoclonal)	Cell Signaling Technology	Cat#5125; RRID:AB_1903890
Phospho AMPKα Thr172 (40H9) (monoclonal)	Cell Signaling Technology	Cat#2535; RRID:AB_331250
AMPKα (D5A2) (monoclonal)	Cell Signaling Technology	Cat#5831; RRID:AB_10622186
Bacterial and Virus Strains		
E. coli: BL21 (DE3) Competent Cells	Thermo Fisher Scientific	Cat#EC0114
Biological Samples		
N/A	N/A	N/A
Chemicals, Peptides, and Recombinant Proteins		
Recombinant human M-CSF	Peprotech	Cat#300-25
Ultrapure lipopolysaccharide (LPS) from *E. coli* K12	InvivoGen	Cat#tlrl-peklps
Recombinant murine IFN-γ	Peprotech	Cat#315-05
Oligomycin A	Sigma-Aldrich	Cat#75351; CAS:579-13-5
Carbonyl cyanide 4-(trifluoromethoxy) phenylhydrazone (FCCP)	Sigma-Aldrich	Cat#C2920; CAS:370-86-5
Rotenone	Sigma-Aldrich	Cat#R8875; CAS:83-79-4
Antimycin A from *Streptomyces* sp.	Sigma-Aldrich	Cat#A8674; CAS:1397-94-0
2-deoxy-*D*-glucose (2-DG)	Sigma-Aldrich	Cat#D8375; CAS:154-17-6
Adenosine	Sigma-Aldrich	Cat#A9251; CAS:58-61-7
Inosine	Sigma-Aldrich	Cat#I4625; CAS:58-63-9
Hypoxanthine	Sigma-Aldrich	Cat#H9377; CAS:68-94-0
5-Deoxy-5-(methylthio)adenosine (MTA)	Sigma-Aldrich	Cat#D5011; CAS:2457-80-9
S-(5-Adenosyl)-*L*-methionine	Sigma-Aldrich	Cat# A7007; CAS:86867-01-8
S-(5-Adenosyl)-*L*-homocysteine	Sigma-Aldrich	Cat#A9384; CAS:979-92-0
Cytidine	Sigma-Aldrich	Cat#C122106; CAS:65-46-3
Uridine	Sigma-Aldrich	Cat#U3750; CAS:58-96-8
2′-Deoxyadenosine	Sigma-Aldrich	Cat#D7400; CAS:16373-93-6
5′-Deoxyadenosine	Sigma-Aldrich	Cat#D1771; CAS:4754-39-6
Cholesterol Oxidase from *Streptomyces* sp.	Sigma-Aldrich	Cat#C8649; CAS:9028-76-6
L-Glutamine-$^{15}N_2$	Sigma-Aldrich	Cat#490032; CAS:204451-48-9
Palmitic acid-$^{13}C_{16}$	Sigma-Aldrich	Cat#605573; CAS:56599-85-0
Fumaric acid-$^{13}C_4$	Sigma-Aldrich	Cat#606014
Guanosine-$^{13}C_1$,$^{5}N_2$	Santa Cruz Biotechnology	Cat#sc-490348 CAS:197227-95-5
Sodium fumarate-2,3-$^{13}C_2$	Sigma-Aldrich	Cat#489468 CAS:287389-39-3
L-Glutamine-$^{13}C_5$,$^{15}N_2$	Sigma-Aldrich	Cat#607983
D-Glucose-^{13}C	Sigma-Aldrich	Cat#389374; CAS:110187-42-3
Adenosine-$^{13}C_{10}$,$^{15}N_5$	Cambridge Isotope Laboratories	Cat#CNLM-3806 CA-PK

(*Continued on next page*)

Continued

REAGENT or RESOURCE	SOURCE	IDENTIFIER
Adenine:HCL:1/2-H2O-$^{15}N_5$	Cambridge Isotope Laboratories	Cat#NLM-6924-PK
SB-204990 (ACLY inhibitor)	Cayman Chemical	Cat#15245;CAS: 154566-12-8
L-alanosine	Cayman Chemical	Cat#19545;CAS: 5854-93-3
Laccase from *Trametes versicolor*	Sigma-Aldrich	Cat#51639;CAS: 80498-15-3
ABTS	Sigma-Aldrich	Cat#10102946001; CAS:30931-67-0
Ferulic acid	Sigma-Aldrich	Cat#1270311;CAS:1135-24-6
Sinapic acid	Sigma-Aldrich	Cat#D7927; CAS:530-59-6
Fumaric acid	Sigma-Aldrich	Cat#F8509; CAS: 110-17-8
TRIzol Reagent	Thermo Fisher Scientific	Cat#15596026
Recombinant full-length human FAMIN (FAMIN^{254I} and FAMIN^{254V})	This paper	N/A
YfiH	This paper	N/A
YlmD	This paper	N/A
Recombinant truncated FAMIN (FAMIN$^{\Delta176}$)	This paper	N/A
TEV Protease	Sigma-Aldrich	Cat#T4455
L-Malic acid	Sigma-Aldrich	Cat#M7397; CAS: 97-67-6
Phenylmethylsulfonyl fluoride (PMSF)	Sigma-Aldrich	Cat#10837091001; CAS: 329-98-6
Hypoxanthine-$^{13}C_5$,$^{15}N_2$	Santa Cruz Biotechnology Ltd.	SC-353627
Adenosine monophosphate-$^{13}C_{10}$,$^{15}N_5$	Sigma Aldrich	Cat#650676
Adenosine triphosphate-$^{13}C_{10}$,$^{15}N_5$	Sigma Aldrich	Cat#710695
Succinic acid-$^{13}C_4$	Sigma Aldrich	Cat#491985
Cell Free Amino Acid Mixture- ^{13}C,^{15}N	Sigma Aldrich	Cat#767964-1EA
Critical Commercial Assays		
pHrodo Red AM Intracellular pH Indicator	Thermo Fisher Scientific	Cat#P35372
BCECF AM	Thermo Fisher Scientific	Cat#B1150
CyQUANT Cell Proliferation Assay Kit	Thermo Fisher Scientific	Cat#C35011
MitoSOX Red Mitochondrial Superoxide Indicator	Thermo Fisher Scientific	Cat#M36008
Mitochondrial Membrane Potential Assay Kit (TMRE)	Abcam	Cat#ab113852
MitoTracker Green FM	Thermo Fisher Scientific	Cat#M7514
Mouse Macrophage Nucleofector Kit	Lonza	Cat#VPA-1009
Lipofectamine RNAiMAX Transfection Reagent	Thermo Fisher Scientific	Cat#13778075
Pierce BCA Protein Assay Kit	Thermo Fisher Scientific	Cat#23225
Seahorse XFe96 FluxPak mini	Agilent	Cat#102601-100
Deposited Data		
RNA-Seq	This paper	GEO: GSE126641
Apo YlmD	This paper	PDB: 6T0Y
Inosine-bound YlmD	This paper	PDB: 6T1B
Experimental Models: Cell Lines		
HepG2	ATCC	Cat#HB-8065; RRID:CVCL_0027
Human Embryonic Kidney 293T (Hek293T)	ATCC	Cat#CRL-3216; RRID:CVCL_0063
Experimental Models: Organisms/Strains		
Mouse: *Famin*$^{p.284R}$	(Cader et al., 2016)	N/A
Mouse: *Famin*$^{p.254I}$	(Cader et al., 2016)	N/A
Mouse: *Famin*$^{p.254V}$	(Cader et al., 2016)	N/A
Mouse: *Famin*$^{+/+}$	(Cader et al., 2016)	N/A
Mouse: *Famin*$^{-/-}$	(Cader et al., 2016)	N/A

(*Continued on next page*)

Continued

REAGENT or RESOURCE	SOURCE	IDENTIFIER
Oligonucleotides		
siRNA targeting: human FAMIN (*LACC1*; *C13orf31*)	Horizon Discovery (Dharmacon)	Cat#M-015653-00
siRNA targeting: human purine nucleoside phosphorylase (*PNP*)	Horizon Discovery (Dharmacon)	Cat#M-009579-02
siRNA targeting: human methylthioadenosine phosphorylase (*MTAP*)	Horizon Discovery (Dharmacon)	Cat#M-009539-01
siRNA targeting: human adenosine deaminase (*ADA*)	Horizon Discovery (Dharmacon)	Cat#M-009588-01
siRNA targeting: mouse adenylosuccinate lyase (*ADSL*)	Horizon Discovery (Dharmacon)	Cat#L-064380-01
siRNA targeting: mouse adenylosuccinate synthase (*ADSS*)	Horizon Discovery (Dharmacon)	Cat#L-060265-01
siRNA targeting: mouse adenosine monophosphate deaminase 1 (*AMPD1*)	Horizon Discovery (Dharmacon)	Cat#L-048694-01
siRNA targeting: mouse adenosine monophosphate deaminase 2 (*AMPD2*)	Horizon Discovery (Dharmacon)	Cat#L-063716-01
siRNA targeting: mouse adenosine monophosphate deaminase 3 (*AMPD3*)	Horizon Discovery (Dharmacon)	Cat#L-010174-00
Recombinant DNA		
pESG-IBA105	IBA life sciences	Cat#5-4505-001
pPSG-IBA105	IBA life sciences	Cat#5-4305-001
pMAL-C5X	New England Biolabs	Cat# N8108S
Software and Algorithms		
Prism 8.0	GraphPad software	https://www.graphpad.com/; RRID:SCR_002798
Microsoft Excel	Microsoft	https://www.microsoft.com/en-gb/ RRID:SCR_016137
Thermo Xcalibur 4.1	Thermo Fisher Scientific	Cat#OPTON-30382; RRID:SCR_014593
Compound Discoverer 2.1	Thermo Fisher Scientific	Cat#OPTON-30834
Adobe Illustrator CC 2019 (23.0.3)	Adobe Inc.	https://www.adobe.com/products/illustrator.html; RRID:SCR_010279
Other		
Dextrin Sepharose MBPTrap High Performance column	GE Healthcare	Cat#28-9187-80
Q5 Site-Directed Mutagenesis Kit	New England BioLabs	Cat#E0554S
METLIN database	Scripps Research Institute	https://metlin.scripps.edu/landing_page.php?pgcontent=mainPage
The Universal Protein Resource (UniProt)	EMBL-EBI; Swiss Institute of Bioinformatics (SIB); Protein Information Resource (PIR) - Georgetown University	https://www.uniprot.org/help/about
Gravity flow Strep-Tactin XT Superflow	IBA GMBH	Cat#2-4012-001
PureYield Plasmid Maxiprep System	Promega	Cat#A2392
cOmplete Mini EDTA-free Protease Inhibitor Cocktail	Sigma-Aldrich	Cat#11836170001
Ni-NTA Superflow column	QIAGEN	Cat#30622
Superdex 200 Increase 10/300 GL	GE life sciences	Cat#28990944
Seahorse XF Base Medium	Agilent	Cat#102353-100
20 × LumiGLO Reagent	Cell Signaling Technology	Cat#7003
BEH amide (150 mm x 2.1 mm, 1.7 μm)	Waters Ltd.	Cat#186004802
BEH C8 (100 mm x 2.1 mm, 1.7 μm)	Waters Ltd.	Cat#186002878
ACE C18-PFP (150 mm x 2.1, 2 μm)	Hichrom	Cat#EXL-1010 1502U
Gemini NX-C18 (150 × 2 mm, 3 μm)	Phenomenex	Cat#00F-4453-B0

LEAD CONTACT AND MATERIALS AVAILABILITY

Further information and requests for resources and reagents should be directed to and will be fulfilled by the Lead Contact, Arthur Kaser (ak729@cam.ac.uk). All unique/stable reagents generated in this study are available from the Lead Contact upon reasonable request but may require a completed Materials Transfer Agreement.

EXPERIMENTAL MODEL AND SUBJECT DETAILS

Mice

6- to 10-week-old mice were used for all experiments and were age- and gender-matched for individual experiments. C57BL/6N *Famin*$^{p.254I}$, *Famin*$^{p.254V}$, *Famin*$^{p.284R}$, *Famin*$^{+/+}$ and *Famin*$^{-/-}$ mice have previously been described (Cader et al., 2016). Mice were heterozygously bred and for all experiments littermates were randomly assigned to experimental groups. Mice were maintained under specific pathogen-free conditions at the Central Biomedical Services facility, University of Cambridge. All procedures performed had local ethics and UK Home Office approval.

Cell lines

HepG2 (RRID: CVCL_0027), an adherent cell line isolated from liver lesions of a male Caucasian patient (ATCC HB-8065), and HEK293T (RRID: CVCL_0063) a cell line derived from human fetal kidney (ATCC CRL-3216) were maintained in DMEM medium and kept in a 5% carbon dioxide (CO_2) incubator at 37°C. Unless otherwise stated, all culture media were supplemented with penicillin/streptomycin (1%) and heat-inactivated fetal bovine serum (10%). All cell lines used in this study were authenticated and purchased from ATCC and are not included within the register of misidentified cell lines curated by the International Cell Line Authentication Committee registry (ICLAC).

Murine bone marrow-derived macrophage

Bone marrow-derived macrophages (BMDMs) were prepared by flushing mouse femurs and tibias with PBS. Cells were filtered through a 70 μm cell strainer and re-suspended in complete RPMI-1640 medium (containing 100 U/mL of penicillin-streptomycin, 1 mM HEPES buffer and 10% FBS). To generate BMDMs, cells were cultured for 6 days in complete medium containing 100 ng/mL of M-CSF with media exchanged after 3 days. Macrophages were harvested, seeded and polarized for 24 h toward M1 macrophages with IFN-γ (50 ng/mL) plus LPS (20 ng/mL), or toward M2 macrophages with IL-4 (20 ng/mL), or left unstimulated and used as M0 macrophages. For adenosine, guanosine, adenine, fumarate and palmitate tracing experiments, M0 macrophages and/or M1 macrophages were pulsed for 3 h or as indicated with 50 μM [$^{13}C_{10}{}^{15}N_5$] adenosine, [$^{15}N_5$] adenine, [$^{13}C_1{}^{15}N_2$] guanosine or 100 μM [$^{13}C_{16}$] palmitate (6:1 conjugation with BSA) or 300 μM [$^{13}C_2$] fumarate, [$^{13}C_4$] fumarate prior to direct extraction with 4:1 methanol/H_2O. For glucose tracing experiments, M1 macrophages were cultured for 1 h or as indicated in RPMI glucose-free medium supplemented with 2 g/L of [$^{13}C_6$] glucose prior to direct methanol extraction. For glutamine tracing experiments, M1 macrophages were cultured with RPMI-glutamine free medium supplemented with 2 mM of [$^{13}C_5{}^{15}N_2$] glutamine or [$^{15}N_2$] glutamine for 24 h prior to direct methanol extraction.

METHOD DETAILS

Plasmids

Complementary DNA encoding human FAMIN^{254I} (NP_001121775, NM_001128303) was cloned into a pESG-IBA105 vector (IBA Life Sciences) that contains an N-terminal Twin-Strep-tag and TEV cleavage motif. The FAMIN^{254V} construct was generated via site-directed mutagenesis using a Q5 Site-Directed Mutagenesis Kit (New England BioLabs), following manufacturer's instructions. Sequences for YfiH (Uniprot P33644, PDB 1Z9T; from *Escherichia coli* strain K12, phylum *Proteobacteria*) and YlmD (Uniprot P84138, PDB 1T8H; from *Geobacillus stearothermophilus*, phylum *Firmicutes*) were synthesized by Origene and cloned into a pPSG-IBA105 vector (IBA Life Sciences). For FAMIN and FAMIN$^{\Delta 176}$ (amino acids 176-430 of FAMIN) MBP fusion proteins, *FAMIN* cDNA sequences were synthesized by GenScript and codon-optimized for prokaryotic expression, and cloned into a pMAL-C5x (New England BioLabs) vector downstream of a MBP tag that is linked to Factor Xa and TEV protease cleavage motifs.

Mammalian expression and purification of FAMIN

HEK293T cells were transfected with PEI-DNA complex containing the Strep-tagged FAMIN expression plasmids. After 48-72 h, transfected cells were harvested in PBS and centrifuged twice at 800 × g for 3 min and the pellet resuspended in hypotonic lysis buffer (10 mM NaCl, 10 mM HEPES, 1 mM TCEP and 10% glycerol pH 7.6) supplemented with Complete Mini EDTA-free protease inhibitor cocktail (Sigma) plus PMSF at 1 mM. Following sonication and clearance by centrifugation at 50,000 × g, the lysates were then loaded onto a Streptactin XT Superflow column (IBA Life Sciences) pre-equilibrated with at least 4 column volumes of lysis buffer. The column was then washed with 10 column volumes of wash buffer (100 mM NaCl, 100 mM HEPES, 1 mM TCEP and 10% glycerol pH 7.6) and the Strep-tagged protein was eluted from the column with 6 column volumes of 50 mM biotin. The purified recombinant protein was then incubated with His-tagged TEV protease (Sigma) at a ratio of 10:1 as determined by A280

quantification using a NanoDrop spectrophotometer. The mixture was incubated overnight at 4°C. TEV protease was then removed by passing the mixture through a pre-equilibrated 1 mL Ni-NTA Superflow column (IBA Life Sciences). The flow-through constituting tag-free recombinant protein was collected. This was then concentrated with a 10 kDa column filter (Amicon) and further purified by size exclusion using an AKTA Superdex 200 increase (10/300) column (GE Life Sciences) column, followed by copious washing. Eluted fractions corresponding to positive peaks on the chromatogram were confirmed on Coomassie SDS-PAGE. Streptactin-purified FAMIN with retained tag exhibited activity indistinguishable from protein prepared, as described above, and was used in select experiments as indicated in the legend.

Prokaryotic expression and purification of MBP-FAMIN fusion proteins

E. coli BL21(DE3) cells were transformed with MBP-full length FAMIN or MBP-FAMIN$^{\Delta 176}$ expression plasmids and grown at 30°C in ampicillin supplemented LB media. Expression was induced at an OD600 of 0.5 – 0.7 with 0.3 mM IPTG for 4 h. Cultures were harvested by centrifugation and cell pellets washed twice with PBS. Cells were then resuspended in 5 mL of lysis buffer containing 20mM NaCl, 20 mM HEPES, 10% glycerol, pH 8.0, 1× cOmplete Mini EDTA-free protease inhibitor cocktail (Roche). The cells were lysed by sonication on ice and cleared by centrifugation at 35,000× *g* for 30 minutes. The soluble fraction was treated with 5 μg / mL of DNase I (Sigma) and 10 μg / mL of RNase A (Sigma) for 15 minutes on ice. The protein-containing supernatant was filtered through a 0.2 μm filter, diluted in 10× volume of lysis buffer, and then loaded onto a pre-equilibrated dextrin sepharose MBPTrap High Performance column (GE Healthcare). The column was washed with 20 column volumes of modified lysis buffer containing 750 mM NaCl. The protein was eluted with 10 column volumes of a buffer containing 100 mM NaCl, 20 mM HEPES, 10 mM maltose, 10% glycerol, pH 8.0. The eluted fractions were pooled and concentrated for use in further assays.

Expression and Purification of YlmD and YfiH

E. coli BL21(DE3) cells transformed with the YlmD or YfiH expression plasmid were grown at 37°C in LB media containing 100 mg l^{-1} ampicillin. Expression was induced at an OD600 of 0.6 with 0.1 mM IPTG for 18 h at 18°C. Cultures were harvested by centrifugation at 7,000 × g then resuspended in lysis buffer containing 10 mM Tris, pH 8.0, 200 mM NaCl, 10% glycerol, 2 mM DTT, 1:10,000 (v/v) benzonase solution (Sigma), 1 × cOmplete Mini EDTA-free protease inhibitor cocktail (Roche). The cells were lysed by sonication on ice. The lysate was clarified by centrifugation (30 min, 35,000 × *g*). The protein-containing supernatant was filtered through a 0.45 μm filter and loaded onto a 5 mL StrepTrap column (GE Healthcare). The column was washed with 10 column volumes of 10 mM Tris, pH 8.0, 200 mM NaCl, 10% glycerol, 2 mM DTT. The protein was eluted using 4 column volumes of 10 mM Tris, pH 8.0, 200 mM NaCl, 10% glycerol, 2 mM DTT, 2.5 mM D-desthiobiotin. The elution fractions were pooled and further purified using on a Superdex 200 increase (10/300) size-exclusion column (GE Healthcare) in 10 mM HEPES pH 7.4, 200 mM NaCl, 0.5 mM TCEP.

Crystallization and crystallographic structure determination of YlmD

YlmD was concentrated to 5.6 mg ml^{-1} and crystal hanging drop vapor diffusion experiments were set up at 22°C in EasyXtal 15-well DG-tool plates (QIAGEN). Hanging drops were set up by mixing 1.5 μl of protein and 1.5 μl of reservoir solution, 0.1 M HEPES pH 7.5, 0.5 M NaCl, 25% PEG 6000. For data collection without inosine, crystals were harvested and soaked for 5-10 min in cryoprotectant containing 0.1 M HEPES pH 7.5, 0.5 M NaCl, 25% PEG 6000 and 20% glycerol. For data collection in the presence of inosine, crystals were soaked for 45-60 min in cryoprotectant containing 0.1 M HEPES pH 7.5, 0.5 M NaCl, 25% PEG 6000, 20% glycerol, 0.5 mM sodium phosphate, 0.5 mM zinc sulfate and 18.7 mM inosine. Overnight soaks with inosine and co-crystallization with inosine resulted in lower-resolution diffraction without improving electron density for bound inosine. The crystals were then flash frozen in liquid nitrogen. X-ray diffraction data were collected at 100 K at Diamond Light Source beamlines I03 and I04 and processed with autoPROC (Vonrhein et al., 2011) and STARANISO (Tickle et al., 2018).

The structure was determined by molecular replacement with Phaser using the available structure of YlmD (PDB 1T8H) as the search model (McCoy et al., 2007). Models were iteratively refined in Fourier space using data up to 1.2 Å resolution with REFMAC (Chen et al., 2010; Otwinowski and Minor, 1997) and PHENIX (Adams et al., 2010). Model building and real space refinement were performed in COOT version 0.8.9.2 (Emsley and Cowtan, 2004).

Extraction of aqueous metabolites

Cells were harvested as indicated using either direct extraction with 4:1 methanol:water or trypsin-EDTA (0.25%). Unless otherwise indicated, for direct methanol extraction, cells were washed twice with PBS followed by addition of pre-chilled 4:1 methanol:water. Cells were scraped and the resulting methanol mixture transferred to 2 mL-flat-bottomed screw cap tubes. Samples were then vortexed, sonicated and lastly centrifuged at 21,000 *g* for 10 minutes to pellet any debris. The supernatant was transferred to new 2 mL tubes for drying as described below. Measurement of cellular P_i levels necessitated phosphate-free buffer wash steps, with PBS replaced by a buffer consisting of 162mM ammonium acetate (pH 7.4). All solvents used were HPLC grade or higher and obtained from Honeywell (Fisher Scientific).

Cell pellets harvested using trypsinization were washed with PBS and then subjected to extraction using the methanol:chloroform method described by Folch et al. (1957). Briefly, a stainless steel ball (QIAGEN) was added to each washed cell pellet on dry ice along with 1 mL of ice cold 2:1 chloroform:methanol inside a 2 mL-flat-bottomed screw cap tube (Starlab). The samples were homogenized using a Tissue Lyser (QIAGEN) for 10 min at 25 Hz to ensure optimum extraction and ascertaining to freeze the tissue lyser plates prior

to homogenization in order to keep samples cold during extraction. 400 μL of ice cold water was added and the samples thoroughly vortexed and sonicated for 5 minutes before centrifugation at 21,000 *g* for 5 min. After centrifugation the aqueous (top layer) and organic (bottom layer) fractions were separated and aliquoted into separate screw-cap tubes both kept on dry ice. A further 1 mL of 2:1 chloroform:methanol was added to the original tube containing the protein pellet and the extraction repeated as described above. The resulting layers were combined, dried (as described below) and stored at −20°C prior to further preparation and analysis.

LC-MS sample preparation

Aqueous extracts of cells or protein reaction mixtures were lyophilised using a centrifugal evaporator (Savant, Thermo Scientific) and reconstituted in 100 μL (for cell extracts) and 200 μL (for protein reaction mixtures) of 7:3 acetonitrile: 0.1 M aqueous ammonium carbonate containing 2 μM [$^{13}C_{10}{}^{15}N_5$] adenosine monophosphate, [$^{13}C_{10}{}^{15}N_5$] adenosine triphosphate, 10 μM [$^{13}C_4$] succinic acid and 10 μM [$^{13}C_5{}^{15}N_5$] glutamic acid (all from Sigma Aldrich except the glutamic acid from Cambridge Isotope Laboratories) as internal standards, although it should be noted that for experiments using labeled substrates, internal standards were omitted to avoid contamination of metabolites. The resulting solution was vortexed then sonicated for 15 min followed by centrifugation at 21,000 *g* to pellet any remaining undissolved material. Samples not run in HILIC mode were reconstituted directly with 50 μL of aqueous 10 mM ammonium acetate containing 2 μM [$^{13}C_{10}{}^{15}N_5$] adenosine monophosphate, adenosine triphosphate [$^{13}C_{10}{}^{15}N_5$], 10 μM [$^{13}C_4$] succinic acid and a 2 in 100000 dilution of a cell free amino acid mixture containing all the proteinogenic amino acids U[$^{13}C^{15}N$] labeled. Samples were thoroughly vortexed and sonicated as above. After centrifugation the supernatants were transferred with an automatic pipette into a 300 μL vial (Fisher Scientific) and capped ready for analysis. Ammonium carbonate and ammonium acetate were Optima grade obtained from Fisher Scientific.

LC-MS analysis of aqueous metabolites

For untargeted analysis, a Velos Pro Elite orbitrap mass spectrometer coupled to a U3000 chromatography system or a Q Exactive Plus orbitrap coupled to a Vanquish Horizon ultra high performance liquid chromatography system was used. For targeted analysis, samples were analyzed using a Quantiva triple stage quadrupole mass spectrometer coupled to a Vanquish Horizon (all analytical instrument combinations supplied by Thermo Fisher Scientific).

Samples were then analyzed using a bridged ethylene hybrid (BEH) amide hydrophilic interaction liquid chromatography (HILIC) approach for the highly polar aqueous metabolites. For this analysis the strong mobile phase (A) was 100 mM ammonium carbonate, the weak mobile phase was acetonitrile (B) with 1:1 water:acetonitrile being used for the needle wash. The LC column used was the BEH amide column (150 × 2.1 mm, 1.7 μm, Waters). The following linear gradient was used: 20% A in acetonitrile for 1.5 min followed by an increase to 60% A over 2.5 min with a further 1 min at 60% A after which the column was re-equilibrated for 1.9 min. After each chromatographic run the column was washed with 30 column volumes of 6:4 water:acetonitrile followed by a further 10 column volumes of 95:5 acetonitrile:water for storage. The total run time was 7 min, the flow rate was 0.6 mL/min and the injection volume was 5 μL. In order to resolve pentose phosphates for identification of ribose-1-phosphate a shallower gradient was employed: 30% A in acetonitrile for 2.0 minutes followed by an increase to 50% A over 3.0 minutes with re-equilibration for 1.9 minutes. After HILIC analysis samples were dried and reconstituted in the same volume of 10 mM ammonium acetate (for samples not run in HILIC mode this drying step was omitted) prior to orthogonal mixed mode analysis using an ACE Excel C18-PFP column (150 × 2.1 mm, 2.0 μm, Hichrom). Mobile phase A consisted of water with 10 mM ammonium formate and 0.1% formic acid and mobile phase B was acetonitrile with 0.1% formic acid. For gradient elution mobile phase B was held at 0% for 1.6 min followed by a linear gradient to 30% B over 4.0 minutes, a further increase to 90% over 1 min and a hold at 90% B for 1 min with re-equilibration for 1.5 minutes giving a total run time of 6.5 minutes. The flow rate was 0.5 mL/min and the injection volume was 2 μL. The needle wash used was 1:1 water:acetonitrile. Both chromatography modes were used for both targeted and untargeted analysis.

For basic pH reversed phase LC-MS analysis of analytes such as nucleoside phosphates and inorganic phosphate (P_i; 96.9696 in negative ESI) in samples reconstituted in aqueous ammonium acetate, a base stable Phenomenex Gemini NX-C18 (150 × 2 mm, 3 μm) (Phenomenex Ltd., Macclesfield, UK) column was employed using the following chromatography method with a weak mobile phase (A) of 10 mM ammonium acetate with 0.1% ammonia and a strong mobile phase (B) of acetonitrile. Mobile phase B was held at 0% for 1.6 min, followed by a linear gradient to 30% B over 4.0 minutes, a further increase to 90% over 1 min, and a hold at 90% B for 1 min, with re-equilibration for 1.5 minutes giving a total run time of 6.5 minutes. The flow rate was 0.5 mL/min and the injection volume was 2 μL. The needle wash used was 1:1 water:acetonitrile.

For enzyme kinetic assays requiring quantitation of ribose-1-phosphate a further chromatographic approach was used to allow for analysis of all substrates and products using a single assay. A Waters BEH C8 column was used (100 × 2.1 mm, 1.7 μm) with a weak mobile phase (A) of aqueous 10 mM ammonium acetate with 0.1% ammonia and a strong mobile phase (B) of acetonitrile. For gradient elution mobile phase B was held at 0% for 1.6 min, followed by a linear gradient to 30% B over 4.0 minutes, a further increase to 90% over 1 min, and a hold at 90% B for 1 min, with re-equilibration for 1.5 minutes giving a total run time of 6.5 minutes. The flow rate was 0.5 mL/min and the injection volume was 2 μL. The needle wash used was 1:1 water:acetonitrile. For those assays requiring only nucleotide and nucleoside quantitation the acidic C18-PFP approach described above was used. The ammonium formate was Optima grade supplied by Fisher Scientific.

Untargeted analysis on the Elite used a high resolution FTMS full scan of 60-1500 *m/z* with a resolution of 60,000 ppm, where due to positive mode negative mode equilibration times each mode was run independently. Source parameters used for the orbitrap were a

vaporizer temperature of 400°C, an ion transfer tube temperature of 300°C, an ion spray voltage of 3.5 kV (2.5 kV for negative ion mode) and a sheath gas, auxiliary gas and sweep gas of 55, 15 and 3 arbitrary units respectively with an S-lens RF (radio frequency) of 60%. For untargeted analysis using the Q Exactive Plus a full scan of 60-900 *m/z* was used at a resolution of 70,000 ppm where positive and negative ion mode assays were run separately in order to maximize data points across a peak at the chosen resolution. The source parameters were the same as those used for the Elite. For analysis of CoA species and reducing equivalents using the Q Exactive Plus orbitrap unique mass spectrometry methodology was employed where the full scan mass range was reduced to 500-1000 *m/z*, the capillary temperature was increased to 350°C and the S-lens RF to 100%.

Targeted analysis on the Quantiva utilized selected reaction monitoring (SRM) employing fast polarity switching with mass transitions and compound dependent parameters (collision energy voltage and RF lens voltage) determined on infusion of 1 μM standards at a flow rate of 10 μl/min in 4:1 acetonitrile:water with 0.1% acetic acid. Source parameters used were a vaporizer temperature of 440°C and ion transfer tube temperature of 362°C, an ion spray voltage of 3.5 kV (2.5 kV for negative ion mode) and a sheath gas, auxiliary gas and sweep gas of 54, 17 and 2 arbitrary units respectively. All fragmentation experiments were carried out using high energy collision dissociation (HCD) at a collision energy of 25eV.

For quantitation of enzyme reaction products in order to determine V_{max} and K_m values a unique sample preparation was employed. Dried enzyme assay samples were reconstituted in 200 μL of 10 mM ammonium acetate containing 1 μM [$^{13}C_{10}{}^{15}N_5$] adenosine, [$^{15}N_5$] adenine, [$^{15}N_4$] inosine (all obtained through Cambridge Isotope laboratories) and [$^{13}C_5{}^{15}N_2$] hypoxanthine (Santa Cruz Biotechnology Ltd., Dallas, TX, USA), thoroughly vortexed, sonicated and transferred to 300 μL glass vials and capped for analysis. Enzyme assay samples using substrate concentrations above 10 μM were further diluted to an effective concentration of 10 μM in the same reconstitution buffer to avoid concentrations above the linear analytical range of the instrumentation. Samples were run using the C18-PFP method described above on the Q Exactive Plus Orbitrap (using established instrumental parameters) with an injection volume of 2 μL. Blank injections were placed in between each test sample to eliminate carry-over effects.

LC-MS data processing

Data were acquired, processed and integrated using Xcalibur (Version 3.0, Thermo Fisher Scientific) and Compound Discoverer (Version 2.1, Thermo Fisher Scientific). For targeted analysis, metabolites of interest were identified using high resolution *m/z* values as specified in the METLIN database (Scripps Research Institute) corresponding to their $[M+H]^+$ or $[M-H]^-$ ion adducts in positive or negative ionisation modes, respectively. Compound retention time and fragmentation pattern were validated against known external standards. Peak areas corresponding to metabolite levels were manually quantified and normalized to internal standard or total ion content (as appropriate). NAD^+/NADH ratios were quantified as relative levels and hence relative ratios have been provided.

For untargeted multivariate analysis performed as part of the screen for enzymatic activity and macrophage metabolomics, data were processed using Compound Discoverer (Version 2.1, Thermo Fisher Scientific) to determine unique LC-MS features with differential abundance between sample groups. For each differential MS feature, chromatogram peaks were manually verified using Xcalibur (Version 3.0, Thermo Fisher Scientific). Accurate *m/z* values of putative compounds were compared against the METLIN database (Scripps Research Institute) including $[M+H]^+$, $[M+Na]^+$, $[M+NH_4]^+$ for positive mode and $[M-H]^-$, $[M+Cl]^-$ for negative mode ion adducts with a mass tolerance of 2ppm. A combination of MS/MS fragmentation profile, molecular formulae calculation based on isotope pattern and expected chromatographic chemical behavior was then used to attribute metabolite identity. In case of ambiguity, and for all proposed FAMIN products and substrates, external standards were used to confirm metabolite identification. Data from positive and negative ionisation modes were combined and duplicate metabolite identities removed. Data was normalized to total ion content and fold change graphically depicted as volcano plots. Metabolite levels between groups were compared using a two-tailed, unpaired Student's t test. For macrophage metabolomics Benjamini-Hochberg correction for multiple testing was applied.

For tracing experiments with [$^{13}C_{10}{}^{15}N_5$] adenosine, [$^{15}N_5$] adenine, [$^{13}C_1{}^{15}N_2$] guanosine, [$^{13}C_{16}$] palmitate, [$^{13}C_6$] glucose, [$^{13}C_5{}^{15}N_2$] glutamine, [$^{15}N_2$] glutamine, [$^{13}C_4$] fumarate and [$^{13}C_2$] fumarate, ^{13}C and/or ^{15}N incorporation into compounds were identified using accurate mass shift of +1.0034 and +0.9970, respectively. [$^{13}C_2$] fumarate contained ^{13}C atoms at position 2 and 3. Unless otherwise indicated, cells were also control-pulsed with unlabelled reagent to determine effects of natural ^{13}C abundance (1.1%) and ^{15}N abundance (0.4%), with levels subtracted from quantified stable isotope incorporation as required. Mass isotopomer (MI) fraction was defined as the peak area of the MI divided by the total peak areas for all MIs expressed as a percentage.

Enzyme assays

Putative enzymatic function of recombinant human FAMIN ($FAMIN^{254I}$) was investigated against an aqueous HepG2 metabolite library or nucleoside substrates at indicated concentrations and detected using UHPLC-MS as described above. The library consisted of the dried, Folch extracted aqueous phase from 5 × 10^6 cells HepG2 cells 48h after transfection with *FAMIN* siRNA. Unless otherwise indicated in the figure legends, HEK293T cell-expressed protein was used for all assays. The reaction mixture (final volume 100 μL) consisted of 10 μg of recombinant protein and 10 μM nucleoside substrate in Dulbecco's PBS (Thermo Fisher), pH 7.4 unless otherwise indicated. For the reverse reaction enzyme assay, 50 μM of adenine and ribose-1-phosphate were used. Protein elution buffer as described above was used as a control. The samples were incubated at 37°C for 1 h and then quenched with × 5 volume of ice-cold methanol. Samples were centrifuged at 21,000 *g* for 5 min transferred to fresh tubes and then dried down prior to analysis as described above.

Laccase assay

Laccase (benzenediol: oxygen oxidoreductase; EC 1.10.3.2) enzymatic activities of recombinant FAMIN^{254I}, YfiH and YlmD were tested against the non-phenolic synthetic substrate ABTS [2,2-azinobis-(3-ethylbenzothiazoline-6-sulfonic acid)] as described (Gorshkov et al., 2017). 10 μg/mL of laccase from *Trametes versicolor* (positive control) or an equivalent quantity of purified FAMIN^{254I}, YfiH or YlmD was used in all assays. The reaction mixture (final volume 100 μL) consisted of 1 mM ABTS, 0.1 mM $CuSO_4$ and purified protein in Dulbecco's PBS (Thermo Fisher), pH 7.4. The samples were incubated at 37°C and activity determined by measuring absorbance change at 405 nM. For LC-MS based laccase assays, the reaction mixture (final volume 100 μL) consisted of 10 μg of recombinant protein and 10 μM laccase substrate, sinapic acid or ferulic acid, in Dulbecco's PBS (Thermo Fisher), pH 7.4 unless otherwise indicated. The samples were incubated at 37°C for 1 h and then quenched with × 5 volume of ice-cold methanol. Samples were centrifuged at 21,000 *g* for 5 min, transferred to fresh tubes and then dried down prior to analysis as described above.

Intracellular pH assay

Intracellular pH (pH_c) was determined using the fluorogenic cytoplasmic pH indicator probe pHrodo Red AM (Thermo Fisher). M0, M1-polarized BMDMs, and HepG2 cells were incubated at 37°C for 30 min in Hank's Balanced Salt Solution (HBSS) supplemented with 20mM HEPES and with pHrodo diluted at 5 μM final concentration. Cells were then washed with HEPES-HBSS and fluorescence measured using a microplate reader (Tecan infinite M1000) with an excitation/emission at 560/585nm. To assess the effects of exogenously supplied fumarate and malate on pH_c, M0 and M1-polarized BMDMs were incubated 24 h prior to pHrodo assay with medium supplied with 300 μM fumarate, 300 μM malate or vehicle control. To evaluate the effects of *L*-alanosine treatment on pH_c, HepG2 cells and M1 macrophages were treated 24 h prior to pHrodo assay with 100uM *L*-alanosine or at the concentration indicated in figure legends in the presence or absence of 300 μM fumarate, 300 μM malate or vehicle control. pH_c was alternatively assessed in M1-polarized macrophages using a dual-excitation ratiometric pH indicator, BCECF AM probe (Thermo Fisher). In brief, cells were loaded with 5 μM of BCECF diluted in HBSS and incubated in a non-CO_2 incubator at 37°C for 30 min. Cells were washed twice with HBSS and signals measured using a microplate reader (Tecan infinite M1000) with dual excitation set at 490 nm and 440 nm and fixed emission at 535 nm.

Oxygen consumption rate and extracellular acidification rate

HepG2 cells were directly plated (7 × 10^3 cells/well) and transfected with specific targeting siRNAs (Dharmacon) for 48 h in XF-96 cell culture plates. BMDMs (7 × 10^4 cells/well) were plated in XF-96 plates and differentiated as described above toward M1 macrophages or left unpolarized and assayed as M0 macrophages. For both BMDMs and HepG2, cells were then washed and incubated for 1 h in XF assay medium (unbuffered DMEM pH 7.4 with 10 mM glucose and 2 mM L-glutamine) in a non-CO_2 incubator at 37°C as per manufacturer's instructions (Seahorse Agilent). Real time measurements of extracellular acidification rate (ECAR) and oxygen consumption rate (OCR) were performed using an XF-96 Extracellular Flux Analyzer (Agilent). Three or more consecutive measurements were obtained under basal conditions and after the sequential addition of 1 μM oligomycin, to inhibit mitochondrial ATP synthase; 1.5 μM FCCP (fluoro-carbonyl cyanide phenylhydrazone), a protonophore that uncouples ATP synthesis from oxygen consumption by the electron-transport chain; and 100 nM rotenone plus 1 μM antimycin A, which inhibits the electron transport chain. To assess glycolysis, three or more consecutive ECAR measurements were obtained under basal conditions and after the sequential addition of 1 μM oligomycin, to elicit maximal glycolytic capacity and 100 mM 2-DG (2-deoxyglucose) to inhibit glycolysis. To assess the effects of *L*-alanosine treatment on OCR and ECAR, cells were exposed to 60 μM (HepG2 cells) or 100 μM (BMDMs) of *L*-alanosine for 24 h or as indicated in the figure legends prior to Seahorse assay. To assess the effects of SB204990 on OCR and ECAR, M0 macrophages were treated with 5 μM of SB204990 for 3 h followed by Seahorse assay. To evaluate the effects of exogenously supplied fumarate or malate on OCR and ECAR, cells were treated 24 h with 250 μM fumarate or malate (HepG2 cells) or 8 h with 300 μM (M0 macrophages) prior to Seahorse assay. OCR was also assessed via Seahorse assay in *Famin*$^{p.254I}$ M0 macrophages silenced for *Adss*, *Adsl or for Ampds (Ampd1, Ampd2 and Ampd3).* Gene silencing in those cells was achieved using an electroporation-based transfection method (Amaxa Nucleofection), according to manufacturer's protocol (Lonza). siRNA of interest was purchased from Dharmacon (Horizon Discovery) and used for nucleofection at final concentration of 300nM.

Transfection of siRNA into HepG2 cells

Gene silencing in HepG2 cells was achieved through lipofection using the Lipofectamine RNAiMAX transfection reagent (Thermo Fisher) coupled to an optimized "reverse transfection" protocol for that cell line as per RNAiMAX manufacturer's protocol (https://www.thermofisher.com/uk/en/home/references/protocols/cell-culture/transfection-protocol/rnaimax-reverse-transfections-lipofectamine.html). For all experiments using siRNA transfection into HepG2 cells, the targeting siRNA of interest was purchased from Dharmacon (Horizon Discovery) and used at final concentration of 25nM.

RNA extraction and sequencing

RNA was extracted using RNeasy Mini Kit (QIAGEN, 74104) with on-column DNase digestion, in accordance with the manufacturer's instructions, and RNA quantified with a NanoDrop ND-1000 spectrophotometer. RNA quality was assessed using the Agilent 2200 TapeStation system. For all samples RNA integrity number was 9.7 or above. Library preparation was performed using the TruSeq stranded mRNA library prep kit (Illumina, 20020594), with 400ng total RNA per sample in accordance with the manufacturer's

instructions. Eleven libraries were sequenced at a time in one lane on an Illumina HiSeq3000 (1x50 base pairs). FastQ files were quality-checked (FastQC; http://www.bioinformatics.babraham.ac.uk/projects/fastqc/) and any residual adaptor sequences were removed (TrimGalore; http://www.bioinformatics.babraham.ac.uk/projects/trim_galore/). Reads were then aligned to the reference genome (mm10, UCSC) using HISAT2 (Kim et al., 2015). Differential gene expression analysis was performed on read count files using the limma package in R with the Voom transformation. Gene Set Enrichment Analysis was performed using log counts-per-million (CPM) following batch correction (sva package in R).

Phylogenetic analysis of FAMIN orthologs

The protein sequences were concatenated and aligned with MAFFT v. 7.20 (RRID: SCR_011811) and maximum-likelihood trees were constructed using RAxML v. 8.2.8 (RRID: SCR_006086) with the standard LG model and 100 rapid bootstrap replicates. Trees were visualized using FastTree followed by iTOL.

Immunoblot

Immunoblot analysis was performed as per standard procedures. In brief, cells were washed with ice-cold PBS and lysed in RIPA buffer (50 mM Tris pH 7.4, 150 mM NaCl, 1% Igepal, 0.5% sodium deoxycholate, 0.1% SDS) supplemented with protease and phosphatase inhibitors. Protein concentration was measured using a Pierce BCA protein assay kit and equal amounts of proteins loaded onto SDS polyacrylamide gels. Proteins were transferred onto nitrocellulose membrane using a Trans-Blot Turbo transfer system (Bio-Rad). Membranes were incubated for 1 h at room temperature in blocking buffer (5% skimmed milk), followed by incubation overnight with primary antibody. Antibodies were detected using HRP-conjugated secondary antibody and visualized using 20 × LumiGLO Reagent (Cell Signaling).

Mitochondrial ROS

For mitochondrial ROS measurements, macrophages were seeded at 4.5×10^4 cells per well in a 96-well half area microplate (Greiner) and polarized as described above. Macrophages were then washed with warm phenol red-free Dulbecco's Phosphate Buffered Saline (DPBS), with $CaCl_2$ and $MgCl_2$. Cells were incubated for 30 min at 37°C with 5 μM of the mitochondrial superoxide indicator probe, MitoSox (Invitrogen), diluted in the same wash medium. Fluorescence intensity was measured after washing using a plate reader (TECAN Infinite M1000) with excitation/emission at 510/580nm. To evaluate the effects of exogenously supplied fumarate on mitochondrial ROS, M1 macrophages were treated with 300 μM fumarate for 24 h prior to the assay.

Mitochondrial membrane potential and biomass

Mitochondrial membrane potential was assessed using the TMRE probe (abcam). Macrophages were seeded at 4.5×10^4 cells per well in a 96-well half area microplate (Greiner) and polarized toward M1 as described above. Cells were incubated for 30 min with TMRE at 100 nM diluted in warm culture medium (RPMI). Cells were then washed twice with warm PBS / 0.2% BSA and fluorescence intensity detected using a plate reader with excitation/emission at 549/575 nm. As indicated, cells were incubated with 5 μM FCCP for 15min prior to adding TMRE. For determination of mitochondrial biomass, M1-polarized microphages were incubated for 30 min with 100 nM of MitoTracker Green (Thermo Fisher) diluted in warm phenol-free, serum-free RPMI medium. Fluorescence intensity was measured using a plate reader (TECAN Infinite M1000) with excitation/emission at 490/516 nm.

Cell proliferation assay

Proliferation rate of HepG2 cells was determined using the CyQUANT Proliferation Assay (Thermo Fisher) following the manufacturer's protocol. In brief, cells were transfected and cultured in black polystyrene microplates with a flat clear bottom (Greiner CELLSTAR). At the indicated time points, fluorescence intensity was measured using a plate reader (Infinite M1000 Pro Multi Detection, TECAN) with appropriate wavelength.

QUANTIFICATION AND STATISTICAL ANALYSIS

Statistical analyses were performed using Graphpad Prism 7 and 8 or Compound Discoverer (Thermo Scientific) as described in LC-MS analysis methods. Statistical parameters including the statistical test used, exact value of *n*, what *n* represents, and measures of distribution and deviation are reported in the figure legends. Unless otherwise stated, statistical significance was calculated as appropriate using unpaired, two-tailed Student's t test or one-way ANOVA with a *P value* of < 0.05 considered significant and applicable post hoc testing. Images utilized within figure schematics have been adapted from https://smart.servier.com/. Data are represented as individual data points with the mean and standard error of the mean (SEM).

DATA AND CODE AVAILABILITY

The data that support the findings of this study are available from the corresponding author upon reasonable request. RNA-Seq data generated in this paper can be accessed at the Gene Expression Omnibus (GEO: GSE126641). Crystallography data for Apo YlmD (PDB: 6T0Y) and inosine-bound YlmD (PDB: 6T1B) have been deposited at the worldwide Protein Data Bank.

Supplemental Figures

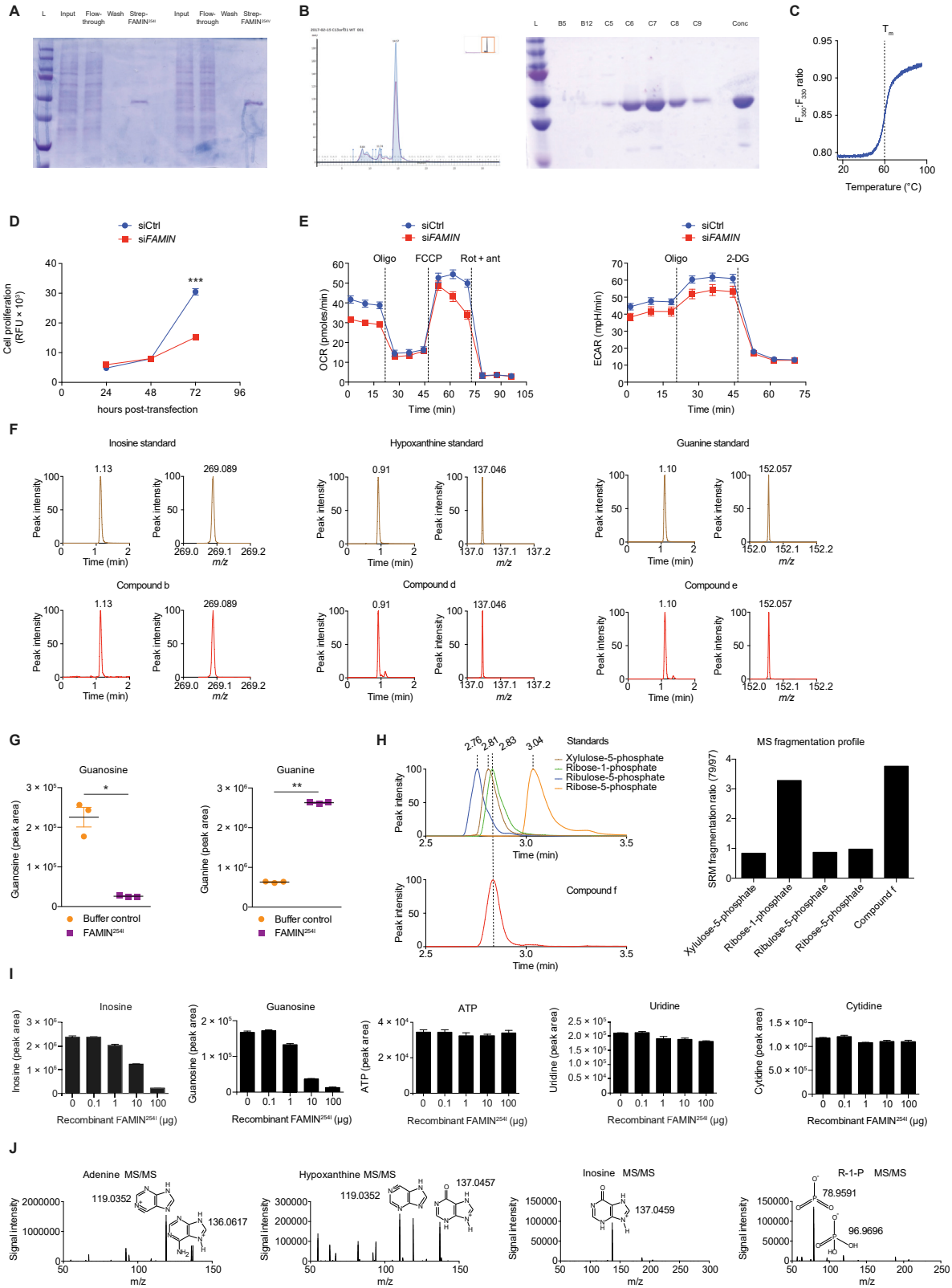

(legend on next page)

Figure S1. FAMIN Metabolizes Purine Nucleosides, Related to Figure 1

(A) Coomassie SDS-PAGE of recombinant human FAMIN^{254I} and FAMIN^{254V} following Strep-Tactin affinity purification. Lanes indicate ladder (L), FAMIN^{254I} or FAMIN^{254V} transfected HEK293T lysate input, column flow-through and concentrated protein eluate.

(B) Left, size exclusion chromatogram of affinity purified FAMIN that has undergone TEV-cleavage to remove Strep-tag. Blue trace corresponds to A280 (protein) and purple trace to A260 (DNA) signal. Fractions C6-C8 were collected, concentrated, and subjected to Coomassie SDS-PAGE. Inset depicts entire chromatogram. Right, Coomassie SDS-PAGE of fractions obtained from size exclusion chromatography. Lanes indicate ladder (L) and fractions B12, C5, C6, C7, C8 and C9, corresponding to the size exclusion chromatogram, and the concentrated protein from fractions C6-C8.

(C) Differential scanning fluorimetry (DSF) of recombinant human FAMIN.

(D) Cell proliferation of HepG2 cells silenced for FAMIN (si*FAMIN*) or transfected with scrambled siRNA (siCtrl) as measured by CyQUANT assay (n = 12).

(E) Oxygen consumption rate (OCR) and extracellular acidification rate (ECAR) of HepG2 cells 48 h after transfection with *FAMIN* or control siRNA. Basal OCR measurement was followed by sequential treatment (dotted vertical lines) with oligomycin A (Oligo), FCCP, and rotenone plus antimycin A (Rot + ant). Basal ECAR measurement was followed by sequential treatment with oligomycin (Oligo) and 2-deoxyglucose (2-DG) (n = 3).

(F) Representative mass spectra and extracted chromatograms for putative FAMIN-catalyzed metabolites and corresponding standards for inosine, hypoxanthine and guanine.

(G) Guanosine and guanine levels following incubation of HepG2 cell aqueous extract with 10 μg recombinant FAMIN^{254I} in 100 μL PBS. (n = 3).

(H) Left, Representative extracted chromatograms for FAMIN-catalyzed compound 'f' and corresponding standards for ribose-1-phosphate, ribose-5-phosphate, ribulose-5-phosphate and xylulose-5-phosphate. All measurements performed using a BEH amide HILIC column and TSQ Quantiva triple quadrupole. Right, Ratio of selected reaction monitoring (SRM) daughter ions with nominal *m/z* values of 79 and 97.

(I) Inosine, guanosine, cytidine, uridine and ATP levels following incubation of 0.1, 1.0, 10.0 or 100.0 μg of recombinant FAMIN^{254I} with the complete metabolomic library (aqueous phase of methanol:chloroform extract of *FAMIN*-silenced HepG2 cells) in 100 μL PBS (n = 3).

(J) LC-MS peaks putatively identified as adenine, hypoxanthine, inosine, or ribose-1-phosphate with nominal *m/z* values of 136, 137, 269 and 229, respectively, were selectively targeted and fragmented using a higher-energy collision dissociation (HCD) collision voltage of 25 eV to give the fragments shown.

Data are represented as mean ± SEM or representative of at least 3 independent experiments. *$p < 0.05$, **$p < 0.01$, ***$p < 0.001$ (unpaired, two-tailed Student's t test).

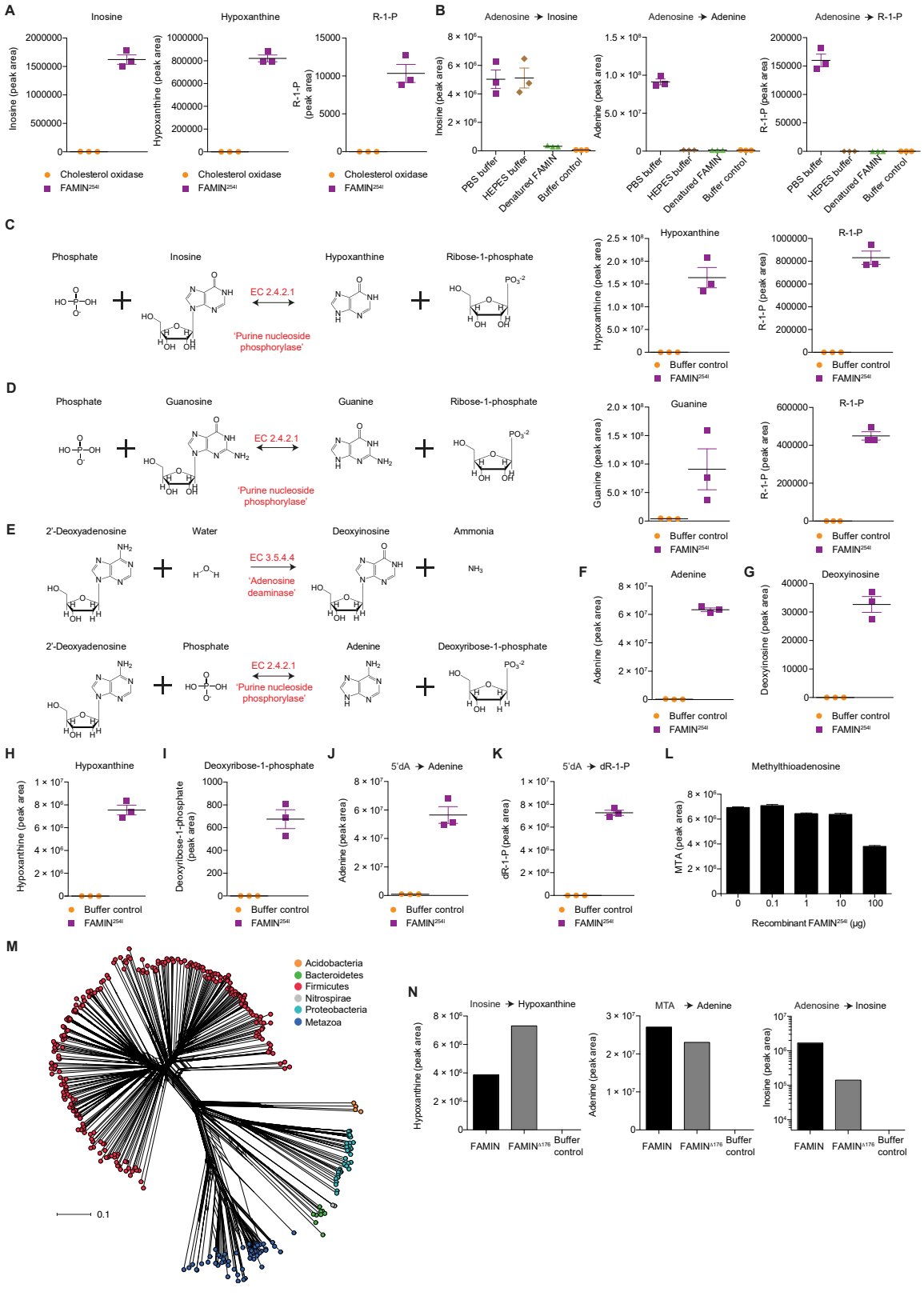

(legend on next page)

Figure S2. Characterization of FAMIN Enzymatic Activity, Related to Figure 2

(A) Inosine, hypoxanthine and ribose-1-phosphate levels following incubation of 10 μg recombinant FAMIN^{254I} or equimolar cholesterol oxidase with 10 μM adenosine for 1 h in 100 μL PBS (n = 3).

(B) Adenine, inosine and ribose-1-phosphate levels following incubation of 10 μg recombinant Strep-tagged FAMIN^{254I} or appropriate controls, including heat-denatured recombinant Strep-tagged FAMIN^{254I}, with 10 μM adenosine for 1 h in 100 μL PBS or HEPES buffer (n = 3).

(C and D) Left, FAMIN-catalyzed enzymatic reactions. Right, levels of guanine or hypoxanthine and ribose-1-phosphate in reactions containing 100 μM guanosine or inosine and recombinant FAMIN^{254I} or buffer control in 100 μL after 1 h at 37°C (n = 3).

(E–I) FAMIN-catalyzed enzymatic reaction with (F) adenine, (G) 2′-deoxyinosine, (H) hypoxanthine and (I) deoxyribose-1-phosphate levels following incubation of 10 μg recombinant Strep-tagged FAMIN^{254I} or buffer control with 10 μM 2′deoxyadenosine for 1 h in 100 μL PBS (n = 3).

(J and K) Adenine (J) and deoxyribose-1-phosphate (K) levels following incubation of 10 μg recombinant Strep-tagged FAMIN^{254I} or buffer control with 10 μM 5′deoxyadenosine (5′dA) for 1 h in 100 μl PBS (n = 3).

(L) MTA levels following incubation of 0.1, 1.0, 10.0 or 100.0 μg of recombinant FAMIN^{254I} with the complete metabolomic library (aqueous phase of methanol:chloroform extract of *FAMIN*-silenced HepG2 cells) in 100 μl PBS (n = 3).

(M) Phylogenetic tree of FAMIN orthologs using human FAMIN protein sequence as the search input.

(N) EC 3.5.4.4 (Adenosine deaminase), EC 2.4.2.1 (purine nucleoside phosphorylase) and EC 2.4.2.28 (MTA phosphorylase) activities of *E. coli* expressed recombinant full-length FAMIN and FAMIN$^{\Delta 176}$ as measured by inosine, hypoxanthine and adenine production following incubation of protein with 10 μM adenosine, inosine and MTA, respectively, in PBS.

Data are represented as mean ± SEM. *p < 0.05, **p < 0.01, ***p < 0.001 (unpaired, two-tailed Student's t test).

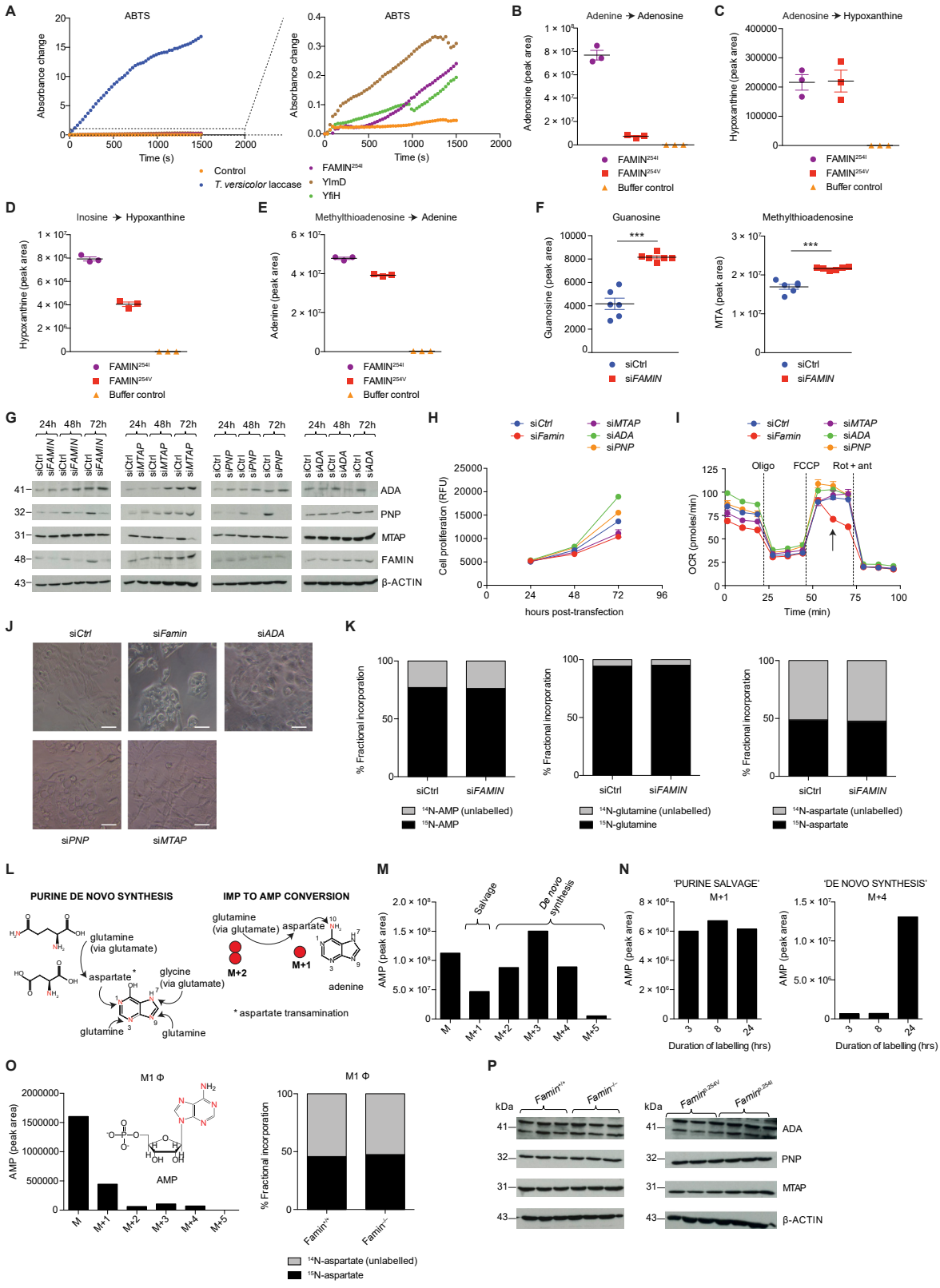

(legend on next page)

Figure S3. FAMIN Enzymatic Activity Determines Cellular Purine Metabolism and Is Impaired in FAMIN^{254V}, Related to Figure 3

(A) Laccase enzyme activity of recombinant YImD, YfiH, FAMIN^{254I} and *Trametes versicolor* laccase using 2,2′-azino-bis-3-ethylbenzothiazoline-6-sulphonic acid (ABTS). Please note the right panel's y axis, which shows a graphical enlargement of the low absorbance readings from the left panel. Data are representative of 2-3 independent experiments.

(B) Adenosine levels following incubation of 10 μg Strep-tagged FAMIN^{254I}, FAMIN^{254V} or control with 50 μM adenine and 50 μM ribose-1-phosphate for 1 h in 100 μL PBS.

(C) Hypoxanthine levels following incubation of 10 μg recombinant Strep-tagged FAMIN^{254I} or FAMIN^{254V} with 10 μM adenosine for 1 h in 100 μL phosphate buffered saline (PBS), (n = 3).

(D) EC 2.4.2.1 (purine nucleoside phosphorylase) and (E) EC 2.4.2.28 (MTA phosphorylase) activities of Strep-tagged FAMIN^{254I} and FAMIN^{254V} as measured by hypoxanthine and adenine following incubation of recombinant protein with 10 μM inosine and methylthioadenosine (MTA), respectively, in PBS (n = 3).

(F) Guanosine and *S*-methyl-5′-thioadenosine levels in control and *FAMIN*-silenced HepG2 cells 48 h after transfection (n = 6).

(G) Immunoblots (IB) for ADA, PNP, MTAP and FAMIN from HepG2 cell lysates silenced for FAMIN (si*FAMIN*), adenosine deaminase (si*ADA*), purine nucleoside phosphorylase (si*PNP*), methylthioadenosine phosphorylase (si*MTAP*) or scrambled siRNA (siCtrl) at 24 h, 48 h or 72 h following transfection; β-ACTIN loading control.

(H) Cell proliferation over time of control, *FAMIN*, *ADA*, *PNP* or *MTAP* silenced HepG2 cells as measured by CyQUANT assay (n = 12).

(I) Oxygen consumption rate (OCR) of HepG2 cells transfected with si*FAMIN*, si*ADA*, si*PNP*, si*MTAP* or siCtrl. Basal OCR measurement was followed by sequential treatment (dotted vertical lines) with oligomycin A (Oligo), FCCP, and rotenone plus antimycin A (Rot + ant), (n = 3). Arrow indicates steep decline observed in siFAMIN cells after treatment with FCCP.

(J) Cell morphology by light microscopy of HepG2 cells silenced with si*FAMIN*, si*ADA*, si*PNP*, si*MTAP* or si*Ctrl* as observed at 72 h after transfection; scale bar = 125 μm. Data are representative of at least 3 independent experiments.

(K–O) A 24h pulse with $^{15}N_2$-glutamine labeled three quarters of AMP in HepG2 cells (n = 3; mean). Since this pulse labeled almost all cellular glutamine and ~50% of aspartate, the number of incorporated ^{15}N atoms into AMP allowed (L–M) estimating the proportion of purine *de novo* synthesis (M+2, M+3, M+4 isotopomers) versus salvage via HPRT (M+1 isotopomer). (N) HepG2 cells engaged both purine salvage and *de novo* synthesis, but as expected with different kinetics. (O) Terminally differentiated M1Φ, in contrast, exhibited very little *de novo* synthesis, Levels of M, M+1, M+2, M+3, M+4, M+5 labeled forms of AMP in M1 macrophages after a 24 h pulse with $^{15}N_2$-glutamine (n = 3; mean). The M+1 isotopomer might substantially underestimate salvage, since only half of aspartate is labeled and any HPRT-dependent salvage subsequent to *de novo* synthesis, or salvage via APRT, would not be captured. This high turnover of the purine ring extends to all essential metabolites and cofactors that contain adenyl groups, i.e., coenzyme A (CoA), acetyl-CoA, flavin adenine dinucleotide (FAD), nicotinamide adenine dinucleotide (NAD), NAD phosphate (NADP), SAM, SAH and MTA (data not shown).

(P) Immunoblots (IB) for adenosine deaminase (ADA), purine nucleoside phosphorylase (PNP) and *S*-methyl-5′-thioadenosine phosphorylase (MTAP) in *Famin*$^{+/+}$ and *Famin*$^{-/-}$ and *Famin*$^{p.254V}$ and *Famin*$^{p.254I}$ M1 macrophages; β-actin, loading control.

Data are represented as mean ± SEM. *p < 0.05, **p < 0.01, ***p < 0.001 (unpaired, two-tailed Student's t test).

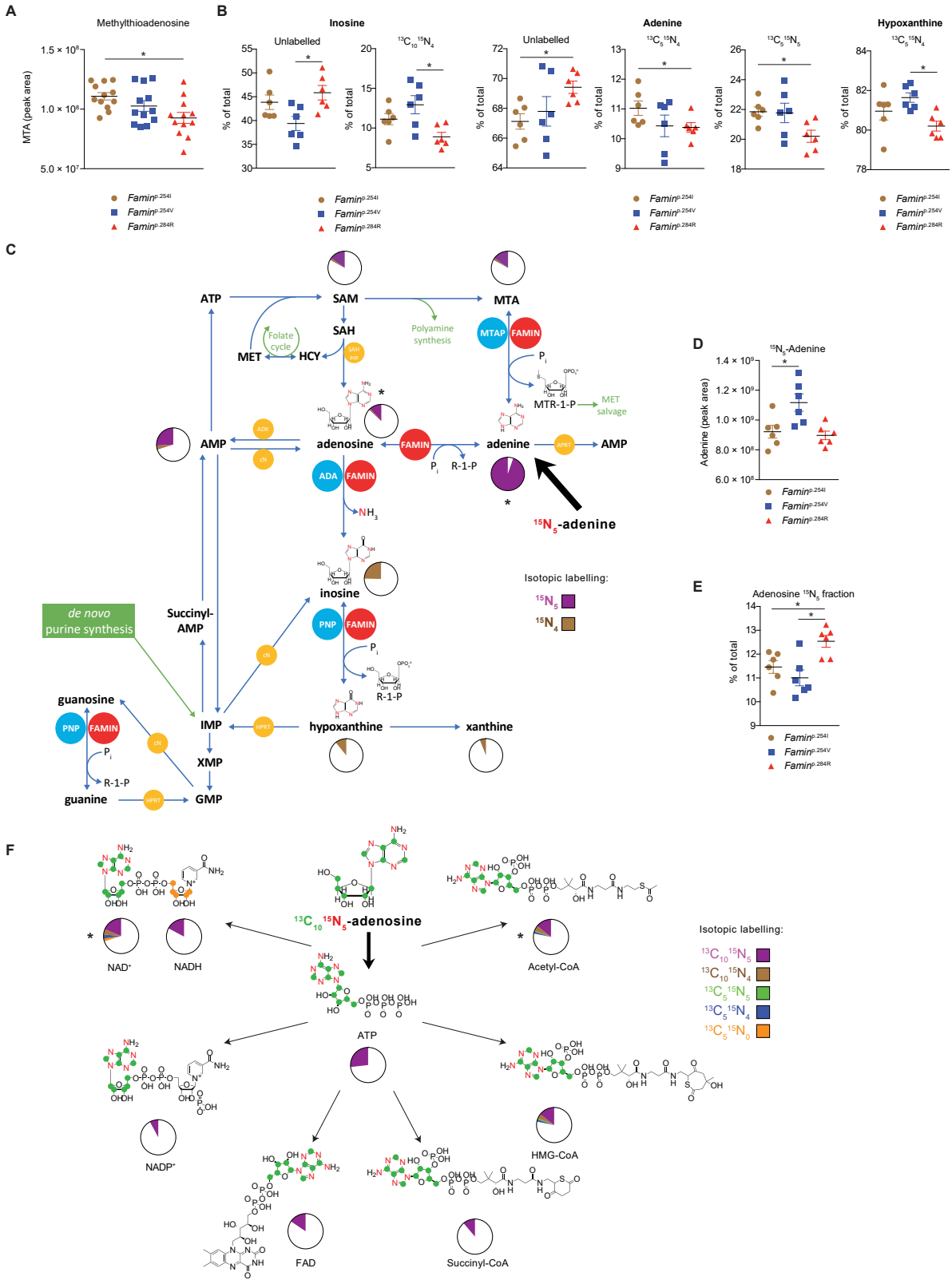

(legend on next page)

Figure S4. FAMIN Affects Routing through Central Purine Metabolism, Related to Figure 4

(A) Methylthioadenosine levels in *Famin*$^{p.254I}$, *Famin*$^{p.254V}$, *Famin*$^{p.284R}$ M1 macrophages (n = 12).

(B) Fraction of inosine, adenine and hypoxanthine labeled as the indicated isotopomer in M1 macrophages after a 3 h pulse with [$^{13}C_{10}{}^{15}N_5$] adenosine (n = 6).

(C) Metabolic fate of stable isotope-labeled [$^{15}N_5$] adenine after a 3 h pulse of M1 macrophages (n = 6; mean). Schematic representation of central purine metabolism. AMP can be generated from adenine via sequential FAMIN and ADK activities or via APRT without loss of label (purple). Labeled [$^{15}N_5$] adenosine can be deaminated into inosine by FAMIN or ADA, with a loss of a single ^{15}N as ammonia, generating a [$^{15}N_4$] isotopomer (brown). Routes of interconversion and relationship with other metabolic pathways are also illustrated. Fractions of different labeled states averaged across genotypes following the 3 h pulse with [$^{15}N_5$] adenine are depicted as pie charts; asterisks indicate metabolites with significantly altered isotopic labeling across genotypes as depicted in Figures S4D and S4E. Adenine phosphoribosyl transferase (APRT); adenosine kinase (ADK); adenosine deaminase (ADA); cytosolic nucleotidase (cN); hypoxanthine-guanine phosphoribosyl transferase (HPRT); purine nucleoside phosphorylase (PNP); *S*-methyl-5′-thioadenosine phosphorylase (MTAP); *S*-adenosylhomocysteine hydrolase (SAHase).

(D) [$^{15}N_5$] adenine levels in M1 macrophages after a 3 h pulse with [$^{15}N_5$] adenine (n = 6).

(E) Fraction of adenosine labeled as the [$^{15}N_5$] isotopomer in M1 macrophages after a 3 h pulse with [$^{15}N_5$] adenine (n = 6).

(F) Fraction of ATP, NAD^+, NADH, FAD, acetyl-CoA, HMG-CoA and succinyl-CoA labeled as the indicated isotopomer in M1 macrophages after a 3 h pulse with [$^{13}C_{10}{}^{15}N_5$] adenosine. Fractions of different labeled states (averaged across *Famin*$^{p.254I}$, *Famin*$^{p.254V}$ and *Famin*$^{p.284R}$ genotypes) are depicted as pie charts. Asterisks indicate significantly altered isotopic labeling across *Famin* genotypes (n = 6 per genotype).

Data are represented as mean ± SEM. *p < 0.05, **p < 0.01, ***p < 0.001 (unpaired, two-tailed Student's t test or one-way ANOVA).

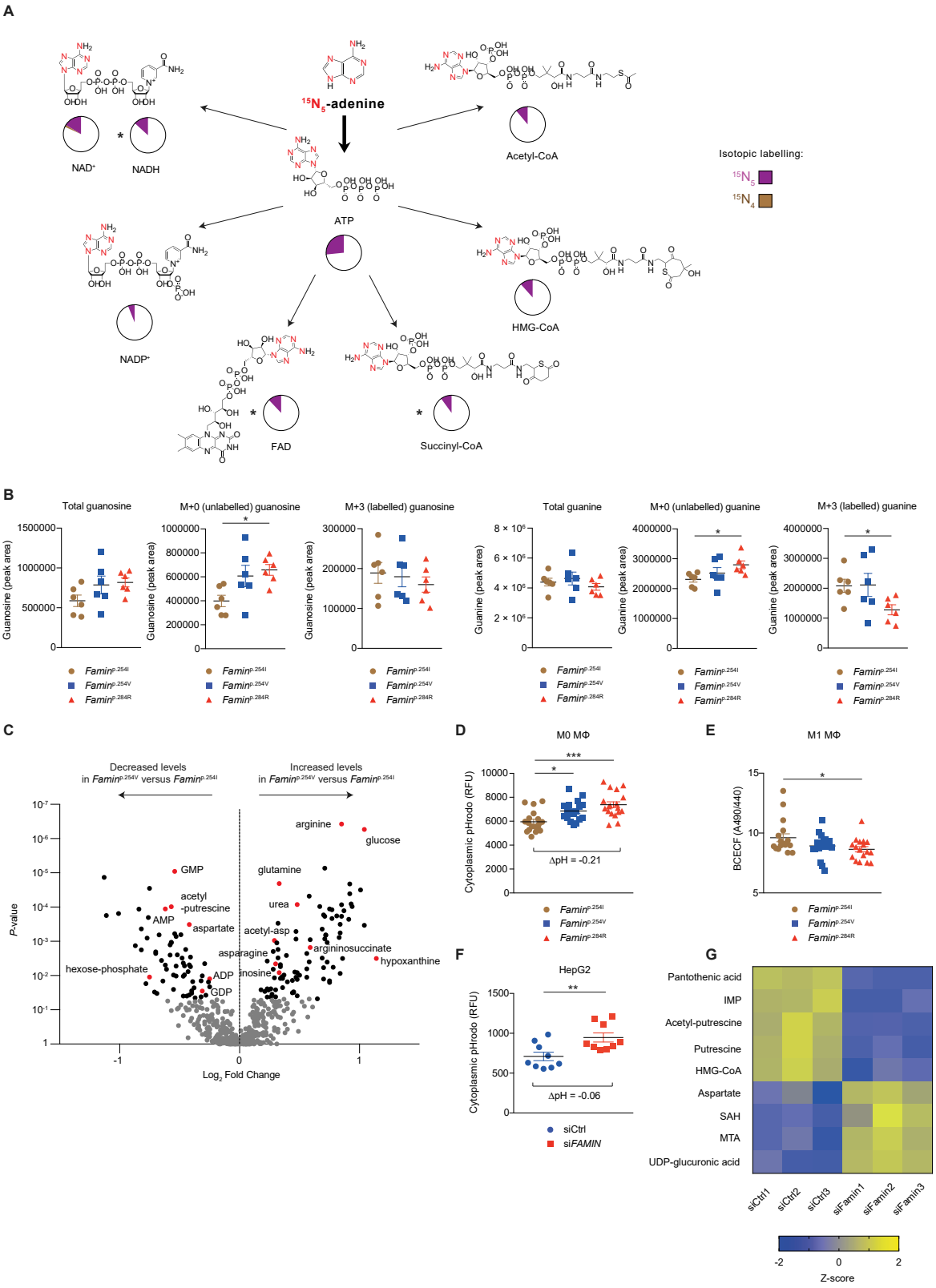

(legend on next page)

Figure S5. FAMIN Activity Affects Purine-Containing Cofactor Turnover, Related to Figure 4

(A) Fraction of ATP, NAD^+, NADH, FAD, acetyl-CoA, HMG-CoA and succinyl-CoA labeled as the indicated isotopomer in M1 macrophages after a 3 h pulse with [$^{15}N_5$] adenine. Fractions of different labeled states (averaged across *Famin*$^{p.254I}$, *Famin*$^{p.254V}$ and *Famin*$^{p.284R}$ genotypes) are depicted as pie charts. Asterisks indicate significantly altered isotopic labeling across *Famin* genotypes (n = 6 per genotype).

(B) Total, unlabelled and [$^{13}C_1{}^{15}N_2$] guanine and guanosine levels in M1 macrophages after a 3 h pulse with [$^{13}C_1{}^{15}N_2$] guanosine (n = 6).

(C) Differential metabolite levels in *Famin*$^{p.254I}$ versus *Famin*$^{p.254V}$ M1 macrophages. Data depicted as a volcano plot using p value and $\log_2$ fold change. Grey dots are non-significant, while black dots correspond to LCMS features with significantly altered abundance following Benjamini-Hochberg correction for multiple testing. Differential metabolites shown in red were confirmed and identified as indicated (n = 6).

(D) Cytoplasmic pH measured using pHrodo in *Famin*$^{p.254I}$, *Famin*$^{p.254V}$, *Famin*$^{p.284R}$ M0 macrophages (n = 18)

(E) Cytoplasmic pH measured using BCECF with dual excitation at 440nm and 490nm in *Famin*$^{p.254I}$, *Famin*$^{p.254V}$, *Famin*$^{p.284R}$ M1 macrophages (n = 18). Reduced 490:440 ratio corresponds to lower (more acidic) pH_c.

(F) Cytoplasmic pH measured using pHrodo in control and *FAMIN*-silenced HepG2 cells 48 h after transfection (n = 9).

(G) Heatmap of metabolites in control and *FAMIN*-silenced HepG2 cells 24 h after transfection (n = 3).

Data are represented as mean ± SEM. *p < 0.05, **p < 0.01, ***p < 0.001 (unpaired, two-tailed Student's t test or one-way ANOVA).

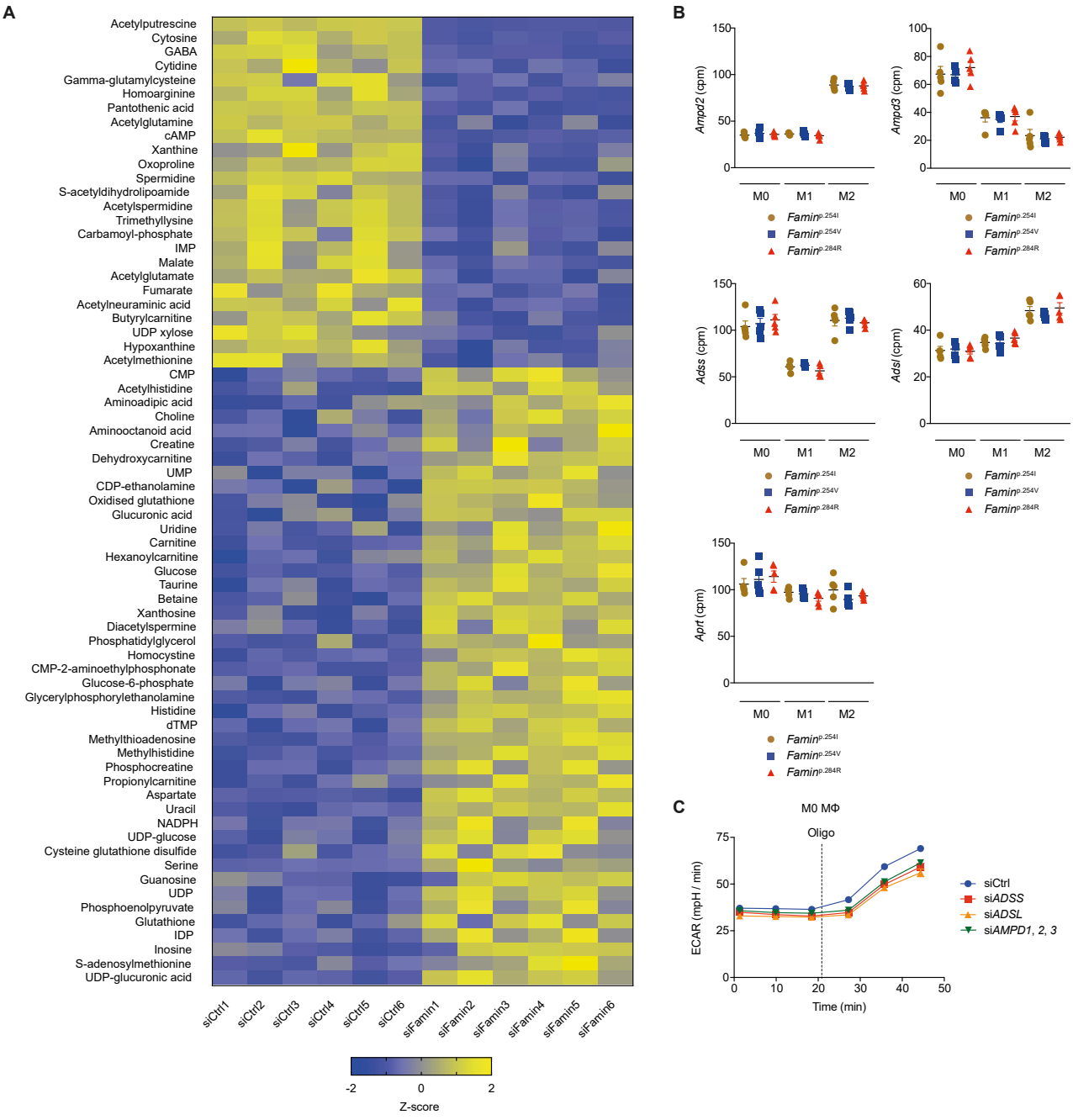

(legend on next page)

Figure S6. A Purine Nucleotide Cycle Operates in Macrophages and HepG2 Cells, Related to Figure 5

(A) Heatmap of metabolites in control and *FAMIN*-silenced HepG2 cells 48 h after transfection (n = 6).

(B) *Ampd2*, *Ampd3*, *Adss*, *Adsl* and *Aprt* expression in *Famin*$^{p.254I}$, *Famin*$^{p.254V}$, *Famin*$^{p.284R}$ M0, M1 and M2 macrophages (n = 5). *Ampd*: AMP deaminase; *Adss*: Adenylosuccinate synthase; *Adsl*: Adenylosuccinate lyase; *Aprt*: Adenine phosphoribosyltransferase.

(C) Extracellular acidification rate (ECAR) of *Famin*$^{p.254I}$ M0 macrophages silenced for *Adss, Adsl and Ampd*s *(Ampd1, 2 and 3)* or transfected with a non-targeting scrambled siRNA control. Basal ECAR measurement was followed by sequential treatment (dotted vertical lines) with oligomycin A (Oligo) (n = 3). *Ampd*: AMP deaminase; *Adss*: Adenylosuccinate synthase; *Adsl*: Adenylosuccinate lyase.

(D) Oxygen consumption rate (OCR), and extracellular acidification rate (ECAR) with maximal respiratory and glycolytic capacities of control and *FAMIN*-silenced HepG2 cells treated with 10 μM, 20 μM, 60 μM, 100 μM of *L*-alanosine or vehicle control for 24 h. Basal OCR and ECAR measurements followed by sequential treatment (dotted vertical lines) with oligomycin A (Oligo), FCCP, and rotenone plus antimycin A (Rot + ant) (n = 3).

Data are represented as mean ± SEM.

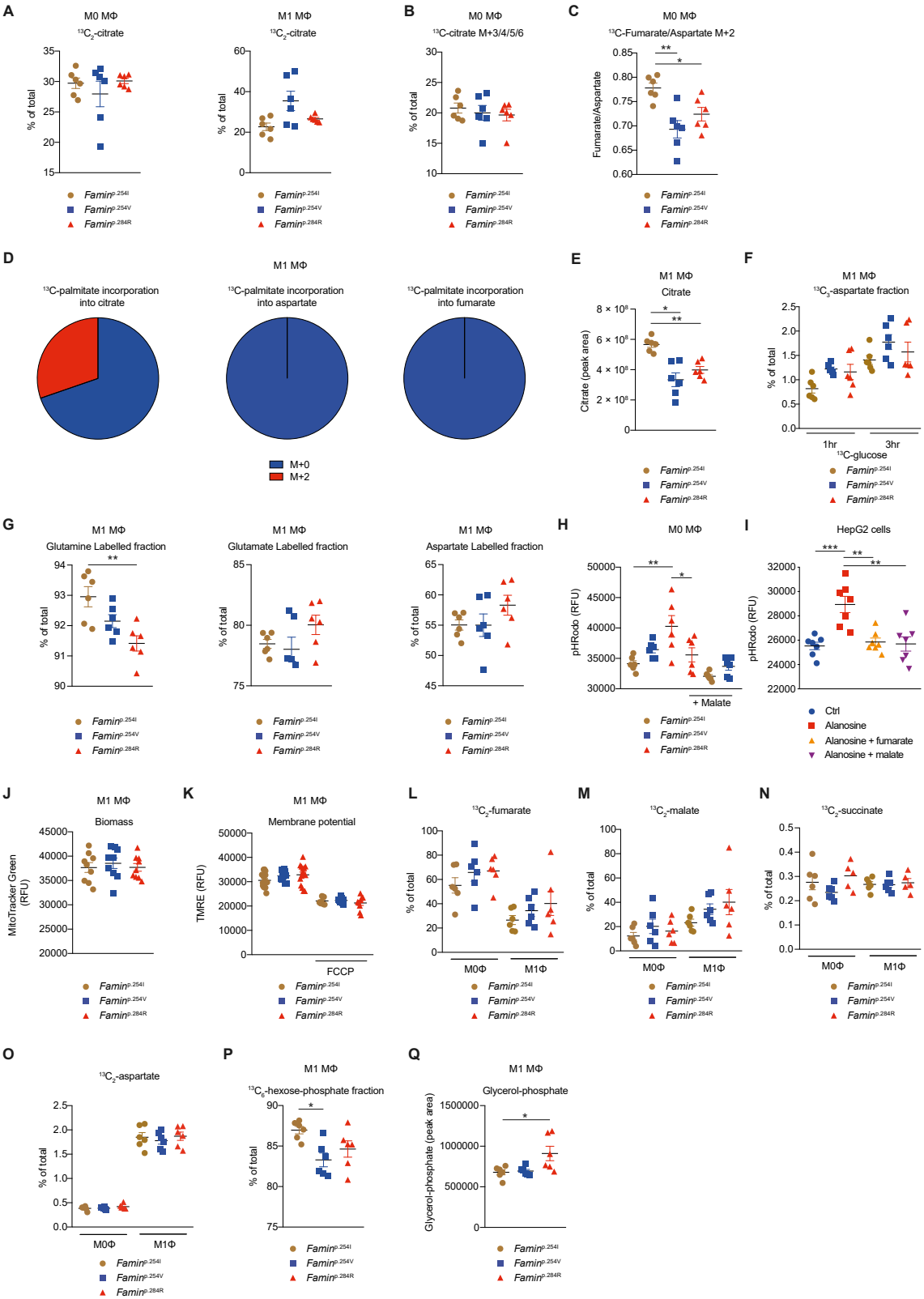

(legend on next page)

Figure S7. The Purine Nucleotide Cycle Is Linked to FAO, and FAMIN Deficiency Can Be Rescued by Exogenous Fumarate, Related to Figures 6 and 7

(A and B) Fraction of citrate labeled as the indicated isotopomer in *Famin*$^{p.254I}$, *Famin*$^{p.254V}$, *Famin*$^{p.284R}$ M0 and M1 macrophages after a 3 h pulse with 100 μM [$^{13}C_{16}$] palmitate conjugated with BSA at 6:1 ratio (n = 6).

(C) Ratio of $^{13}C_2$-fumarate (M+2) to $^{13}C_2$-aspartate (M+2) levels in M0 macrophages after a 3 h pulse with 100 μM [$^{13}C_{16}$] palmitate (n = 6).

(D) Fractions of different labeled states of citrate, aspartate and fumarate (averaged across *Famin*$^{p.254I}$, *Famin*$^{p.254V}$ and *Famin*$^{p.284R}$ genotypes) in M1 macrophages after a 3 h pulse with 100 μM [$^{13}C_{16}$] palmitate conjugated with BSA at 6:1 ratio (n = 6) depicted as pie chart.

(E) Citrate levels in *Famin*$^{p.254I}$, *Famin*$^{p.254V}$, *Famin*$^{p.284R}$ M1 macrophages (n = 6).

(F) Fraction of aspartate labeled as the indicated isotopomer in *Famin*$^{p.254I}$, *Famin*$^{p.254V}$, *Famin*$^{p.284R}$ M1 macrophages after a 1 or 3 h pulse with 2 g/L [$^{13}C_6$] glucose (n = 6).

(G) Fraction of labeled glutamine, glutamate and aspartate in *Famin*$^{p.254I}$, *Famin*$^{p.254V}$, *Famin*$^{p.284R}$ M1 macrophages after a 3 h pulse with 2 mM [$^{13}C_5{}^{15}N_2$] glutamine (n = 6).

(H) Cytoplasmic pH (pH_c) measured using pHrodo in *Famin*$^{p.254I}$, *Famin*$^{p.254V}$, *Famin*$^{p.284R}$ M0 macrophages treated with 300 μM of malate or vehicle control for 24 h. Same control group as Figure 7D (n = 6).

(I) Cytoplasmic pH (pH_c) measured using pHrodo in HepG2 cells treated with vehicle control or 100 μM of *L*-alanosine for 24 h, supplemented as indicated with 300 μM fumarate or malate (n = 7).

(J) Mitochondrial biomass measured using MitoTracker Green in *Famin*$^{p.254I}$, *Famin*$^{p.254V}$, *Famin*$^{p.284R}$ M1 macrophages (n = 6).

(K) Mitochondrial membrane potential measured using TMRE in *Famin*$^{p.254I}$, *Famin*$^{p.254V}$, *Famin*$^{p.284R}$ M1 macrophages, and collapsed following FCCP treatment as indicated (n = 9/6).

(L–O) Labeling of (L) fumarate, (M) malate, (N) succinate and (O) aspartate in M0 and M1 macrophages after a [$^{13}C_2$] fumarate pulse (n = 6).

(P) Fraction of hexose-phosphate labeled as the indicated isotopomer in *Famin*$^{p.254I}$, *Famin*$^{p.254V}$, *Famin*$^{p.284R}$ M1 macrophages after a 1 h pulse with 2 g/L [$^{13}C_6$] glucose (n = 6).

(Q) Glycerol-3-phosphate in *Famin*$^{p.254I}$, *Famin*$^{p.254V}$, *Famin*$^{p.284R}$ M1 macrophages (n = 6).

Data are represented as mean ± SEM. *p < 0.05, **p < 0.01, ***p < 0.001 (unpaired, two-tailed Student's t test or one-way ANOVA).

Journal of proteome research

pubs.acs.org/jpr

Article

The Human and Mouse Islet Peptidome: Effects of Obesity and Type 2 Diabetes, and Assessment of Intraislet Production of Glucagon-like Peptide-1

Sam G. Galvin, Richard G. Kay, Rachel Foreman, Pierre Larraufie, Claire L. Meek, Emma Biggs, Peter Ravn, Lutz Jermutus, Frank Reimann,* and Fiona M. Gribble*

Cite This: *J. Proteome Res.* 2021, 20, 4507−4517

Read Online

ACCESS | Metrics & More | Article Recommendations | Supporting Information

ABSTRACT: To characterize the impact of metabolic disease on the peptidome of human and mouse pancreatic islets, LC-MS was used to analyze extracts of human and mouse islets, purified mouse alpha, beta, and delta cells, supernatants from mouse islet incubations, and plasma from patients with type 2 diabetes. Islets were obtained from healthy and type 2 diabetic human donors, and mice on chow or high fat diet. All major islet hormones were detected in lysed islets as well as numerous peptides from vesicular proteins including granins and processing enzymes. Glucose-dependent insulinotropic peptide (GIP) was not detectable. High fat diet modestly increased islet content of proinsulin-derived peptides in mice. Human diabetic islets contained increased content of proglucagon-derived peptides at the expense of insulin, but no evident prohormone processing defects. Diabetic plasma, however, contained increased ratios of proinsulin and des-31,32-proinsulin to insulin. Active GLP-1 was detectable in human and mouse islets but 100−1000-fold less abundant than glucagon. LC-MS offers advantages over antibody-based approaches for identifying exact peptide sequences, and revealed a shift toward islet insulin production in high fat fed mice, and toward proglucagon production in type 2 diabetes, with no evidence of systematic defective prohormone processing.

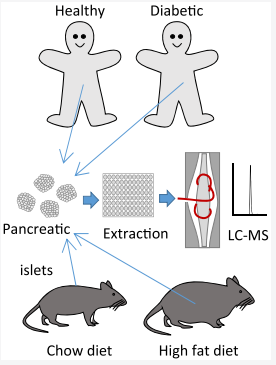

KEYWORDS: *pancreatic islets, mass spectrometry, peptidomics, type 2 diabetes, insulin, glucagon*

INTRODUCTION

Pancreatic islets secrete multiple biologically active peptide hormones, most notably insulin, glucagon, and somatostatin (SST), but a number of recent studies have highlighted the possibility that they might also secrete the incretin hormones, glucagon-like peptide 1 (GLP-1)[1−6] and glucose-dependent insulinotropic peptide (GIP).[7,8] Intraislet release of GLP-1 has been postulated to modulate insulin secretion under conditions such as metabolic stress, although it remains unclear whether it is produced locally at levels sufficient to exert physiologically significant effects on beta cells. The literature is complicated by the use of antibody-based methods to detect and quantify peptide hormones as these are prone to antibody cross-reactivity, but improvements in mass spectrometry methods now allow identification and quantification of exact peptide sequences. This study aimed to identify the exact peptide sequences produced and released from mouse and human islets, and the impact of consuming a high fat diet or development of type 2 diabetes.

Five islet cell populations have been described, including the 3 major cell types: beta cells producing insulin and islet amyloid polypeptide (IAPP), alpha cells producing glucagon and delta cells producing SST-14, together with rarer PP-cells producing pancreatic polypeptide (PPY), and epsilon cells producing ghrelin.[9] Pancreatic islet development shares common endodermal origins and transcription factor requirements with intestinal enteroendocrine cells, so it is not surprising to find overlap of hormone expression between islets and the gut. Indeed, the intestinal hormone peptide YY (PYY) has been detected in alpha, delta, and gamma cells in mouse but not humans.[10,11] GIP has been detected as a shortened version in human and mouse islets (GIP(1−30), compared with (1−42) in the gut), although some antibodies against GIP have been questioned due to their propensity to bind to proglucagon derived peptides,[12−14] and transcriptomic studies failed to find expression of *Gip* in mouse[11] or human islets.[10]

Proglucagon is processed by prohormone convertase (PC) 2 in islets to release glucagon, and by PC1/3 in the gut to generate bioactive GLP-1(7−37/7−36amide). Longer forms of GLP-1(1−37/1−36amide) have been identified in human and rat pancreas[15] and are not bioactive against the GLP-1 receptor (GLP1R) but cross-react with many antibodies against GLP-1. Antagonizing GLP1R attenuates glucose-

Received: June 2, 2021
Published: August 23, 2021

https://doi.org/10.1021/acs.jproteome.1c00463
J. Proteome Res. 2021, 20, 4507−4517

stimulated insulin secretion (GSIS) from human and mouse islets even in the absence of an intestinal source of GLP-1,[4,6,16,17] suggesting a local islet source of a GLP1R agonist peptide, but this need not be GLP-1, as glucagon itself acts on the GLP-1 receptor, albeit with 50−100-fold lower potency than active GLP-1.[18,19] Several studies utilizing liquid chromatography coupled to mass spectrometry (LC-MS) have detected active GLP-1 in islets but have not commented on its abundance relative to glucagon.[1,20]

In addition to clarifying controversies around intraislet GLP-1 and GIP, unbiased LC-MS has potential for elucidating how the islet peptidome responds to metabolic stress. Obesity is well-known to increase insulin secretion, and in rodent models causes beta cell hyperplasia.[21] In type 2 diabetes (T2DM) and diabetic mouse models, there have been reports of beta cell dedifferentiation,[22−24] increased alpha cell numbers, and islet GLP-1 production.[1,2]

In this study, we used LC-MS to probe the peptidome of human and mouse islets in health and under conditions of obesity and T2DM, and to analyze intraislet production of incretin peptides. Using similar LC-MS peptidomic methods, we have previously identified and quantified endocrine peptides in a variety of tissues, plasma, and cell supernatants.[25−27]

METHODS

Unless otherwise stated, all chemicals were obtained from Sigma-Aldrich (Poole, UK). GLP-1(7−36 amide) and glucagon standards were from Bachem (Bubendorf, Switzerland). Internal standards for GLP-1(7−36 amide) and glucagon were from Cambridge Research Biochemicals (Billingham, UK).[28]

Mice

All work was conducted in keeping with the Animals (Scientific Procedures) Act 1986 Amendment Regulations of 2012 and approved by the University of Cambridge Animal Welfare and Ethical Review Board under project licenses 70/7824 and PE50F6065. Mice (either gender, if not stated otherwise) were on a C57BL/6 background, bred in-house under SPF conditions and between 10 and 29 weeks old. For the diet-induced obese (DIO) study, 9−15 week old male mice were assigned to 1 of 2 groups; one fed high fat diet (HFD) (60% fat, Research Diets) for 13 weeks and the other standard chow. Fasting blood glucose levels were taken after 6 h fast. Sixty islets from each mouse were isolated and lysed as below.

Islet Isolation

Mice were sacrificed by cervical dislocation and the pancreas injected with ice-cold Collagenase V (0.75 mg/mL) in HBSS. After digesting the pancreas at 37 °C for 12 min, islets were washed and hand-picked into HBSS with 0.1% BSA (w/v).

Islet Lysate Peptidomics

Islets were washed in HBSS before lysing in a Protein LoBind Eppendorf with 200 μL 6 mol/L guanidine hydrochloride (GuHCl). Three freeze thaw cycles were carried out to aid cell lysis. Proteins were precipitated by adding 800 μL of 80% ACN (v/v) and centrifuging at 4 °C for 5 min at 12 000*g*. The aqueous lower phase containing the peptides was collected, dried in a centrifugal evaporator overnight and stored at −70 °C.

Isolation of Islet Cell Populations

Beta, alpha, and delta cell populations were purified using an Influx Cell Sorter (BD Biosciences, Franklin Lakes, NJ) at the Cambridge Institute for Metabolic Research flow cytometry group. Beta and alpha cells were purified from islets of Glu-GFP mice and delta cells from Sst-Cre/EYFP mice, as described previously.[11] Cells were sorted into 200 μL 6 mol/L GuHCl, then treated as described for islet lysates.

Islet Secretion Assays

Fresh islets were incubated at 37 °C in Kreb's Ringer Buffer (KRB (mmol/L); 129 NaCl, 5 $NaHCO_3$, 4.8 KCl, 1.2 KH_2PO_4, 1.2 $MgSO_4$, 10 HEPES, 2.5 $CaCl_2$ with 0.05% BSA (w/v) for 1 h. Islets were transferred to Protein LoBind Eppendorf tubes with 300 μL of prewarmed KRB containing stimuli detailed in figure legends. Tubes were incubated at 37 °C for 45 min, then 270 μL of supernatant was removed and snap frozen. Nine supernatants were pooled for LC-MS analysis.

Human Islet Study

Ethical approval was obtained from University of Cambridge Human Biology Research Ethics Committee (#HBREC.2019.38). Human islets for research were provided by the Alberta Diabetes Institute IsletCore at the University of Alberta in Edmonton (www.isletcore.ca) with the assistance of the Human Organ Procurement and Exchange (HOPE) program, Trillium Gift of Life Network (TGLN) and other Canadian organ procurement organizations. Islet isolation was approved by the Human Research Ethics Board at the University of Alberta (Pro00013094). All donors' families gave informed consent for the use of pancreatic tissue in research. Donor characteristics (mean ± st. dev.) are Controls (6 male, 3 female), age 50 ± 5 years, BMI 30 ± 3 kg/m^2; T2DM (3 male, 4 female), age 52 ± 7 years, BMI 28 ± 4 kg/m^2, HbA1c 7.3 ± 1.2%, (1 diet-controlled, 4 on metformin, 1 on other oral antihyperglycemic agent, 1 on insulin). Measurements of islet insulin content and Islet Particle Index (a measure of islet size), generated by the Alberta Islet Core at the time of tissue collection, were not significantly different between the T2DM and control groups. Anonymized, snap frozen human islets (2000 islet equivalents (IEQ) per donor, i.e., the standardized equivalent of 2000 islets of diameter 150 μm) were thawed, washed 3× with HBSS, spun at 200*g* for 5 min at 4 °C, and supernatants discarded. Islets were lysed in 250 μL of 6 mol/L GuHCl with 3 freeze thaw cycles, and proteins precipitated as above.

Preparation of Standard Curves

Calibration curves for glucagon and GLP-1(7−36amide) were prepared in matrix comprising mouse pancreatic acinar tissue from which visible islets had been removed, treated with GuHCl and ACN, as above. Internal standards for glucagon and GLP-1(7−36amide) were spiked into calibration standards and islet lysates.

Solid Phase Extraction, Reduction, and Alkylation

Solid phase extraction (SPE), reduction and alkylation, were performed as described previously.[29] Cellular lysates were reconstituted in 0.1% FA (v/v) and supernatants acidified with formic acid to a final percentage of 0.1% (v/v). Samples were extracted on an Oasis PRiME HLB μElution plate (Waters, Milford, MA). Only cellular lysates were reduced and alkylated. Supernatants were run immediately after SPE.

https://doi.org/10.1021/acs.jproteome.1c00463
J. Proteome Res. 2021, 20, 4507−4517

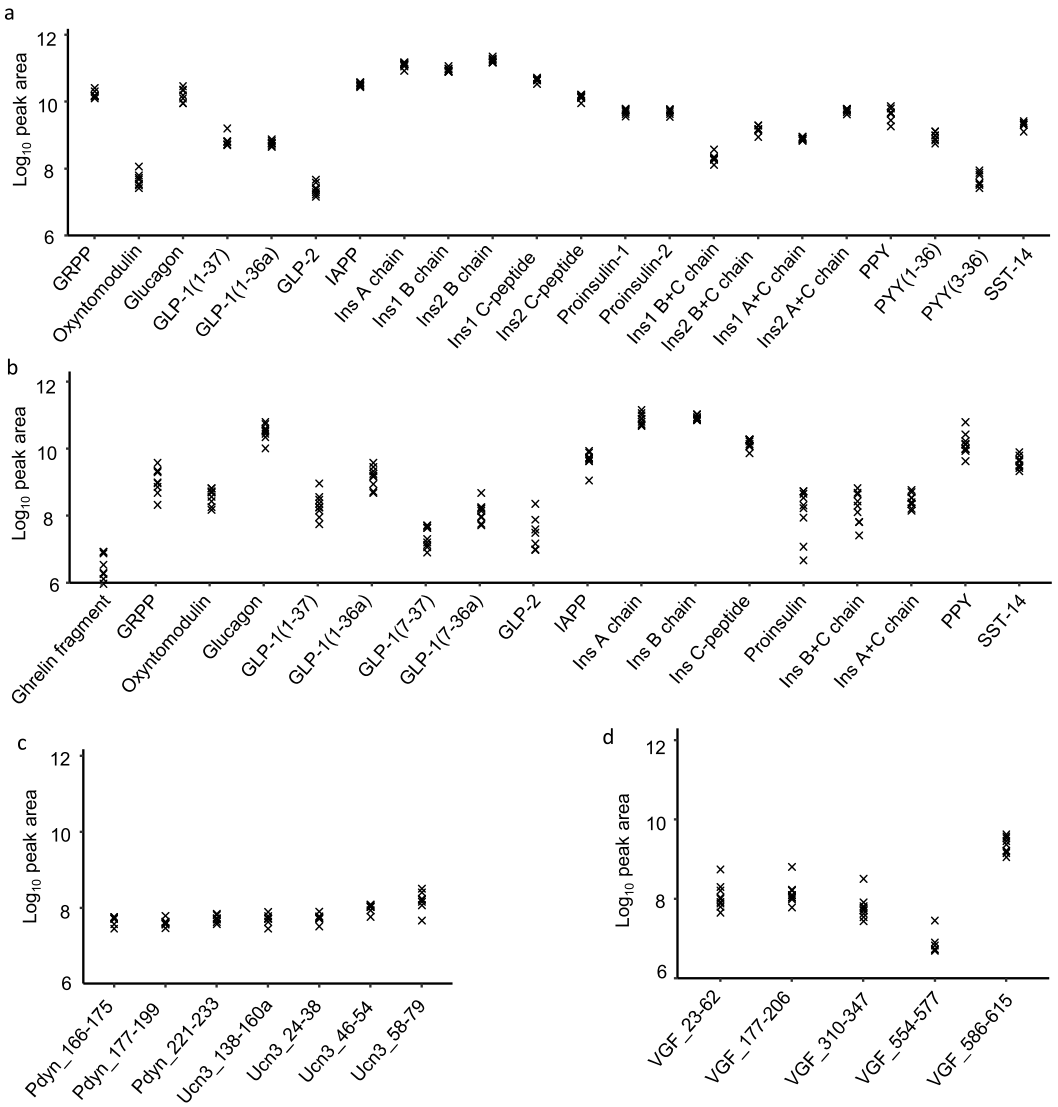

Figure 1. Overview of peptides produced from prohormones in mouse and human islets. Quantification of peptides derived from classical islet prohormones by DDA in mouse islets (a), and human islets (b). Peptides derived from prourocortin-3 and proenkephalin-B in mouse islets (c) and peptides derived from proVGF in human islets (d). If peptides do not have an assigned name in the literature then peptides are named for their gene of origin as well as their position on that gene; e.g., Pdyn_177−199 originates from Pdyn and spans amino acids 177−199. Mouse data from 7 mice. Human data from 9 individuals. N.B. The A chains of insulin-1 an insulin-2 are identical and so only 1 peptide is displayed for the insulin A chain.

Nano LC-MS

For detailed methods on columns, source settings, gradient details, and database searching see ref 29. Briefly, samples were analyzed on a Thermo Fisher UltiMate 3000 Nano LC system coupled to a Q Exactive Plus Orbitrap mass spectrometer (ThermoScientific, San Jose, USA) using electrospray ionization in positive mode. Method run time was 130 min with a full MS scan on ions between 400 and 1600 m/z prior to a MS/MS scan 10 top ions per scan. Product ion scans were used to monitor for specific ions given in Supplementary Table S1. Data files were searched against the mouse SwissProt database (downloaded 26/10/2017) using PEAKS v8.5 software (Waterloo, Ontario, Canada). To quantify data acquired by product ion scans, Xcalibur v4.3.73.11 (Thermo Fisher Scientific) was used to integrate area under the curve on the chromatogram.

Human Plasma

Stored human plasma from the placebo arm of a previous study[30] in which healthy volunteers and patients with type 2 diabetes received a 75 g oral glucose tolerance test, was analyzed by LC-MS to measure insulin, proinsulin and des 31−32 proinsulin. Samples were extracted using well established methods[31] and analyzed on a microflow LC system, coupled to a HSS T3 ionKey (Waters) on the TQ-XS spectrometer. Ten μL of sample was injected onto a trap column at 15 μL/min for a 3 min load, with mobile phases set to 90%A (0.1% formic acid (aq)) and 10% B (0.1% formic acid (acetonitrile)). The ionKey column was set at 45 °C and the analytes were separated over a 13 min gradient from 10% to 55% B, at a flow rate of 3 μL/min. The column was flushed for 3 min at 85% B before returning to initial conditions, resulting in an overall run time of 20 min. Targeted SRM transitions were set up based on parent and precursor ion fragments for each peptide (Supplementary Table S2). Peptide peak areas were quantified

https://doi.org/10.1021/acs.jproteome.1c00463
J. Proteome Res. 2021, 20, 4507−4517

using MassLynx v4.2 (Waters) and normalized as peak area ratio against an internal standard, bovine insulin.

Data Analysis

Data visualization and statistical analysis were carried out using RStudio (v1.3) and R (v4.0.2). When peptidomic differences between one or more groups needed to be assessed, the outputs of PEAKS database searches were obtained and analyzed in R. To control for multiple comparisons, *P* values were adjusted using a permutation-based method using Perseus (Max Planck Institute of Biochemistry, v1.6.14.0).

RESULTS

Peptidomics of Human and Mouse Islets

The major islet hormones—insulin, glucagon, SST, PPY, and IAPP—were detected by LC-MS/MS in extracts of lysed human and mouse islets (Figure 1a,b). Using data dependent acquisition (DDA), we also detected a range of other peptides, including proinsulin, C-peptide, and partially processed insulins, as well as GRPP (the N-terminus of proglucagon) and inactive forms of GLP-1 (1−36amide and 1−37). Active GLP-1 was detectable only in the human samples with this method (Figure 1b). An N-terminal fragment of ghrelin (GHRL_24−37) was detected in human islets, but full length and acylated versions of ghrelin were not detectable in either species. In mouse islets we detected PYY and fragments of prourocortin-3 and proenkephalin-B (alpha-neoendorphin and rimorphin)[32,33] (Figure 1c), and in human islets we found peptides from neurosecretory protein VGF (Figure 1d). We also detected a number of peptides derived from granin proteins and vesicular processing enzymes (Supplementary Figure S1).

Peptidomics of Purified Alpha, Beta, and Delta Cells

We determined the cellular origin of the different peptides by analyzing FACS-purified mouse alpha, beta and delta cells. Across all islet cell samples, 999 peptides were matched by PEAKS database searching, of which 559 were detectable in at least 2 samples. Peptides from proinsulin, proglucagon and proSST separated across the beta, alpha and delta cells respectively, as expected (Figure 2a and Supplementary Table S3). Pancreatic polypeptide (PPY) was detected in alpha and delta cells, although our method of cell separation may have excluded collection of a cell type specifically expressing PPY. PYY was mostly found in delta cells. Peptides from urocortin 3 and proenkephalin-B were found at highest levels in beta cells, together with IAPP (Supplementary Table S3). Most peptides were predominantly identified in a single cell population (Figure 2b and Supplementary Table S3).

Intraislet GLP-1 and GIP

Although active forms of GLP-1(7−36amide and 7−37) were readily detectable in human islets, their peak areas were substantially smaller than those of either glucagon or N-terminally extended inactive GLP-1(1−36 amide and 1−37) (Figure 1b and 3c). From standard curves for glucagon and GLP-1(7−36amide), we estimated that human islets contained 1.2 ± 0.4 pg/IEQ (mean ± SEM, n = 9) of GLP-1(7−36amide), whereas glucagon concentrations were above the highest calibration standard, equivalent to >150 pg/IEQ, with an estimated value of ∼370 pg/IEQ (Supplementary Figure S2). From both the calibrated results and the peak areas shown in Figure 1 and 3c, the glucagon:GLP-1 ratio in human islets was estimated to be >100:1, and likely closer to 300:1.

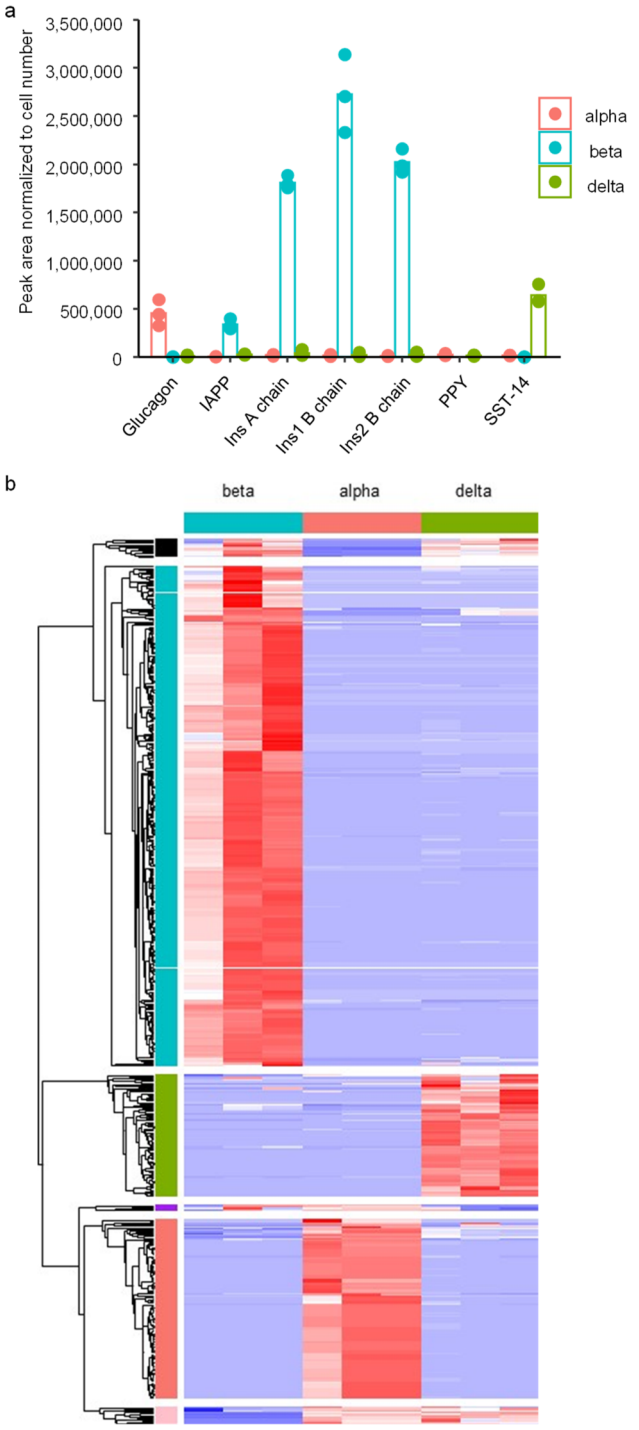

Figure 2. Peptidomics of FACS purified mouse alpha beta and delta cells. (a) Abundance of major islet hormones in the three FACS purified islet cell populations. (b) Heatmap of all peptides matched through Peaks database searching in the 3 purified cell populations. In all plots, the peak area of each peptide was normalized to the number of cells in that sample to account for differences in cell numbers. For alpha and beta FACS purified cells, 3 separate samples were obtained from 3 individual mice, whereas delta cells from 3 pairs of mice were pooled to obtain 3 samples.

In mouse islet lysates, GLP-1(7−36amide and 7−37) could be detected when we used product ion scans to monitor for their fragments, even though they had not been detectable in DDA mode (Supplementary Figure S3). Both b and y ions

https://doi.org/10.1021/acs.jproteome.1c00463
J. Proteome Res. 2021, 20, 4507−4517

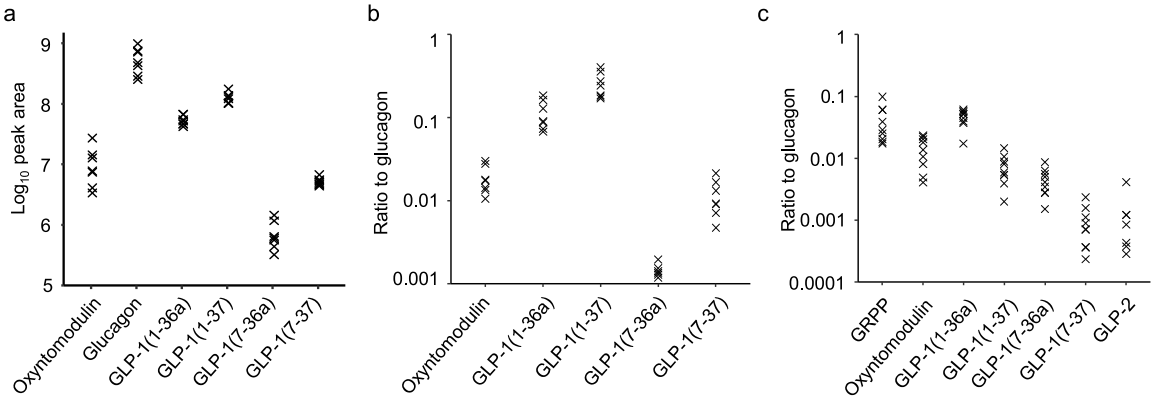

Figure 3. Proglucagon derived peptides. (a,b) Peptides in mouse islets quantified by monitoring for specific product ions after fragmenting precursor ions specific to each peptide. (a) Quantification of proglucagon derived peptides in islet lysates from 7 mice. Each sample contained 60 islets. (b) Ratios of proglucagon derived peptides to glucagon in mouse islets. (c) Ratios of proglucagon derived peptides to glucagon, monitored by DDA, in human islets.

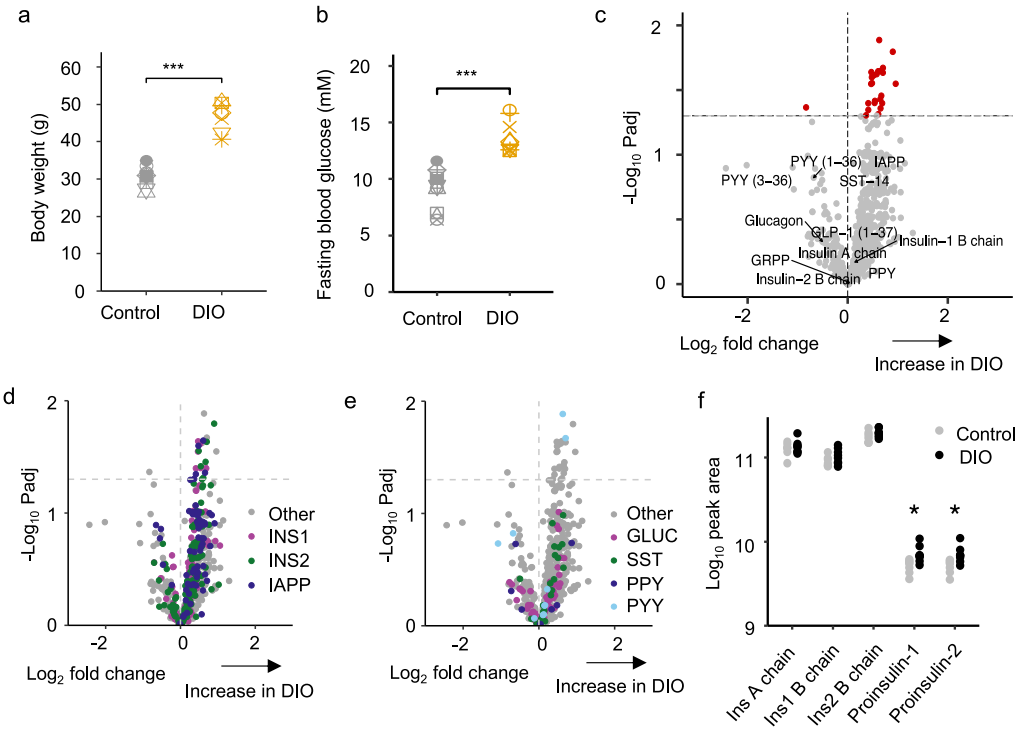

Figure 4. Peptidomic comparison of islets from DIO mice and to lean controls. Body weights (a) and fasting blood glucose levels (b) of DIO mice vs lean controls. (c–e) Volcano plots displaying log2 fold change vs −log10 of the adjusted p value for each peptide. Horizontal dotted line indicates significance threshold of $p = 0.05$. A positive log2 fold change indicates an increase in DIO mice. 718 *t* tests were performed to analyze for significant differences in peptides matched between the groups with a permeation-based method used to adjust for multiple comparisons. In (d,e), peptides from different prohormones are colored in each plot: IAPP and INS derived peptides in (d). GLUC, SMS, PPY, and PYY derived peptides in (e). (f) Peak area of processed insulin-1 and -2 chains in addition to proinsulin-1 and -2. Statistical comparison made using unpaired *t* test without adjustments for multiple comparisons. $^*p < 0.05$. $n = 7$ for control group and $n = 8$ for DIO group.

matching GLP-1 were identified from a peak that coeluted with a standard for GLP-1(7–36 amide), providing compelling evidence for the intraislet production of GLP-1(7–36 amide) in mouse as well as humans. Using the product ion scanning approach, we again estimated the relative abundance of different proglucagon-derived peptides (Figure 3a). Using standard curves, glucagon was quantifiable at 3900 ± 400 pg/islet (mean ± SEM, $n = 7$) whereas GLP-1(7–36 amide) and GLP-1(7–37) were below the lower limit of quantification, and likely therefore <0.8 pg/islet. Both the calibrated data and peak areas suggest a glucagon:GLP-1 ratio of >1000:1 in mouse islets (Figure 3b and Supplementary Figure S2).

Product ion monitoring was also used to search for proGIP derived peptides in mouse islets as none were detected using DDA. We were unable to detect GIP(1–42) (the intestinal form), C-terminally truncated GIP(1–30) (previously described in islets[12]), or a peptide from the N-terminus of proGIP (Gip_22–43) that we can identify robustly in homogenized mouse duodenal tissue (Supplementary Figure S4–S6). GIP was also not detectable in human islets by DDA analysis.

https://doi.org/10.1021/acs.jproteome.1c00463
J. Proteome Res. 2021, 20, 4507–4517

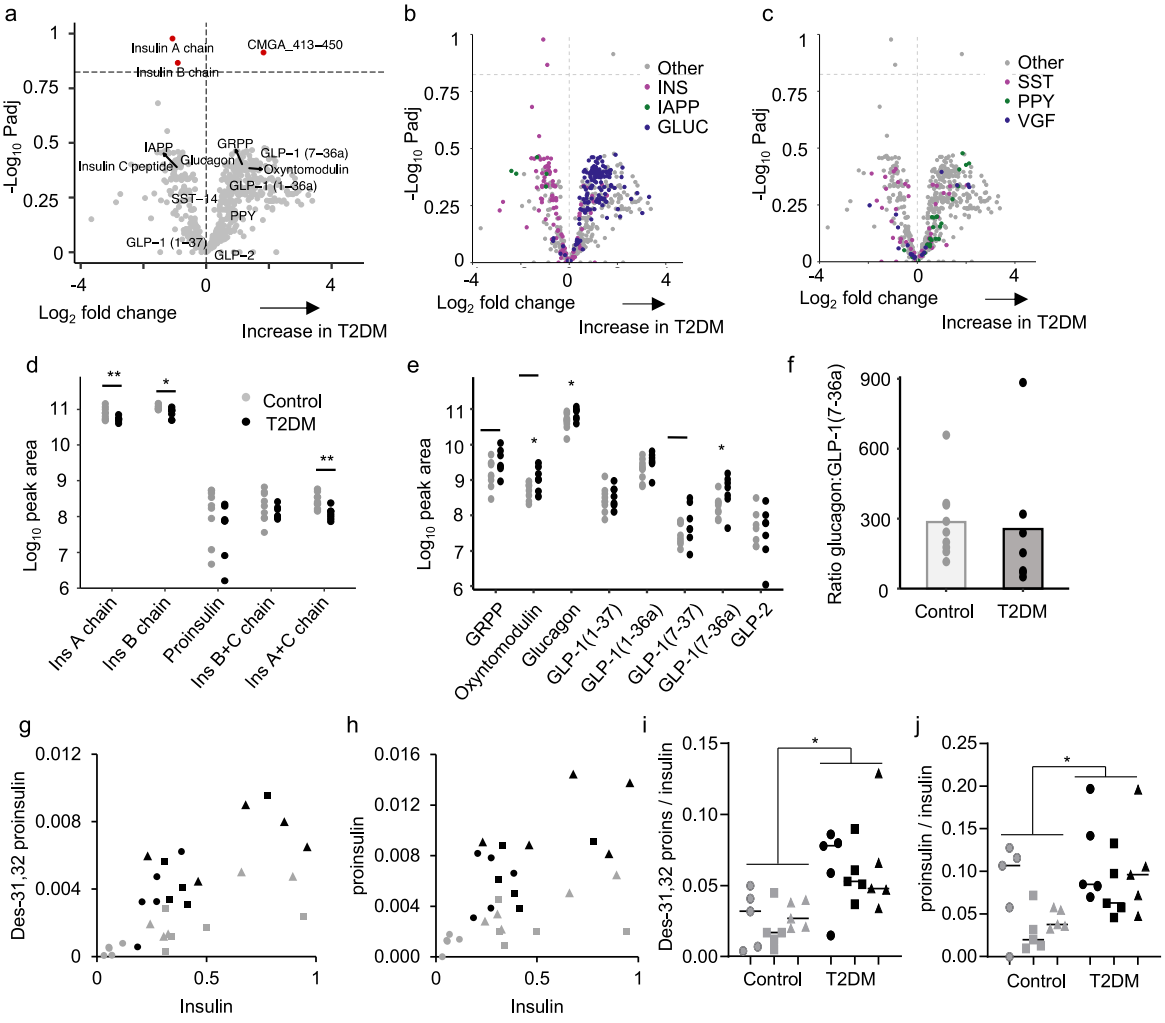

Figure 5. Peptidomic comparison of human islets from type 2 diabetic individuals compared to nondiabetic controls. (a) Volcano plot displaying log2 fold change vs −log10 of the adjusted *p* value for each peptide. Horizontal dotted lines indicates $p = 0.15$. A positive log2 fold change indicates an increase in T2DM. (b,c) Volcano plots displaying in different colors individual peptides derived from proIAPP, proinsulin, and proglucagon (b), and from prosomatostatin, proPPY, and proVGF (c). (d,e) Manually quantified peak areas of processed insulin chains and proinsulin (d), and products of proglucagon processing (e). (f) Ratio of peak area of glucagon:GLP-1(7−36amide) in all samples. Statistical comparison made using unpaired *t* test without adjustments for multiple comparisons. $*p < 0.05$. For a−f, $n = 9$ for the control group and $n = 7$ for T2DM group. Donors were excluded from the analysis if the samples failed to load properly onto the SPE sorbent. (g,h) Plasma des-31,32 proinsulin (g) and proinsulin (h) plotted against insulin for control (gray) and T2DM (black) subjects in the fasting state (circles), and 30 min (squares) or 90 min (triangles) after a 75 g oral glucose tolerance test. Values represent peak area ratios. (i,j) Ratios of data shown in (g,h). $*p < 0.05$ between controls and T2DM by 2-way ANOVA.

Peptidomics of Lean versus Diet-Induced Obese (DIO) Mouse Islets

To assess the effect of obesity on the islet peptidome, mice were fed a high-fat diet for 13 weeks, at the end of which they displayed higher body masses and fasting blood glucose than chow-fed controls (Figure 4a,b). Size-matched islets from both groups were compared by LC-MS/MS, with the results depicted in volcano plots (Figure 4c−e). Fully processed insulin-1, insulin-2, glucagon, SST, and PPY were not significantly different between the groups. However, a number of other fragments from proinsulin and proIAPP were significantly increased in the islets from DIO mice (Figure 4d), as well as 2 peptides from proPYY (Figure 4e). Peptides from granins and processing enzymes were largely unchanged (Supplementary Figure S7a−c and Supplementary Table S4). Manual quantification of proinsulins-1 and -2, which are too long to be matched automatically by the PEAKS software, revealed a significant increase in proinsulin-1 and -2 in the DIO islets (Figure 4f).

Peptidomics of Type 2 Diabetic Islets and Plasma

To investigate the effects of type 2 diabetes on the islet peptidome, we compared nondiabetic and diabetic islets (Figure 5a−c, Supplementary Figure S7d,e and Supplementary Table S5). No individual peptides were significantly altered in diabetes when *p*-values were adjusted for multiple comparisons. However, multiple peptides from proinsulin and IAPP clustered on the "reduced in T2DM" side of the volcano plot, whereas peptides from proglucagon clustered on the "increased in T2DM" side (Figure 5b). Somatostatin-derived peptides exhibited no clear divide, and peptides from PPY were mostly increased in diabetes (Figure 5c).

Manual quantification confirmed significant reductions in insulin A and B chains but not proinsulin in the T2DM group (Figure 5d) and increases in glucagon and GLP-1(7−36amide)

https://doi.org/10.1021/acs.jproteome.1c00463
J. Proteome Res. 2021, 20, 4507−4517

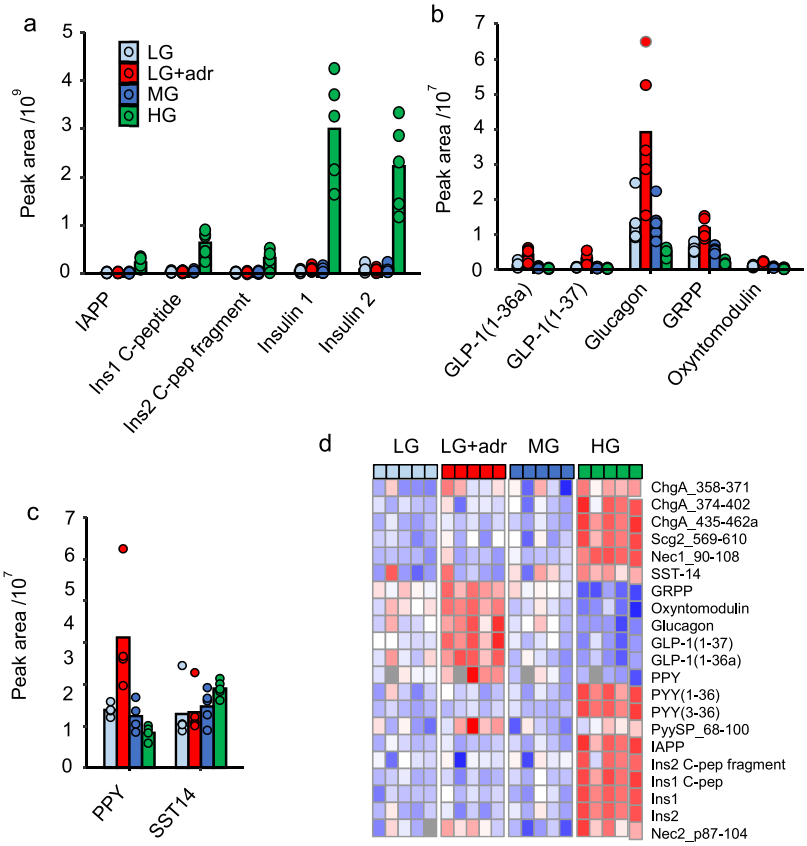

Figure 6. Peptidomics of secretions from mouse islets. (a–c) Peak areas of peptides in supernatants of islets cultured in low, medium, or high glucose, or low glucose + adrenaline. IAPP and insulin-derived peptides (a), proglucagon-derived peptides (b), PPY and SST-14 (c). Individual data points are displayed in each plot along with the mean. Conditions were as follows; LG = 1 mmol/L glucose, LG + Adr = 1 mmol/L glucose + 5 μmol/L adrenaline, MG = 6 mmol/L glucose, HG = 16.7 mmol/L glucose. n = 5 with each data point representing pooled supernatants from 9 tubes each containing 15 islets. Islets obtained from 15 mice. (d) Heatmap of mouse islet secretion peptidomics. Data presented as Z-score of each row. Gray squares within the heatmap indicate where peptides were not detectable. PyySP_68-100 is a peptide from a splice variant of *Pyy* which has 2 amino acids inserted into the C-terminus of the propeptide. It was quantified in lieu of Pyy_68-98 which was undetectable.

(Figure 5e). Using a calibration line, GLP-1(7–36amide) increased from 1.2 ± 0.4 pg/IEQ (mean ± SEM; n = 9 nondiabetic donors) to 3.6 ± 0.9 pg/IEQ (n = 7 diabetic donors, p = 0.025). However, although glucagon measurements were above the top calibration standard, the peak area ratio for glucagon increased in parallel, and the ratio of peak areas for glucagon:GLP-1 was not significantly different between the groups (Figure 5f), suggesting an overall increase in proglucagon biosynthesis (which could reflect either a change in alpha cell number, or proglucagon biosynthesis per cell) rather than a change in processing.

Proinsulin products were also measured by LC-MS/MS in the plasma of control and diabetic volunteers. Both before and after an oral glucose challenge, we observed elevated circulating levels of proinsulin and des-31,32 proinsulin in the diabetic group, which were proportionally increased following glucose ingestion, suggesting that incompletely processed proinsulin products exhibit glucose-sensitive secretion and are coreleased with insulin following glucose challenge (Figure 5g,h).

Secretory Patterns from Mouse Islets

Mouse islets were incubated with low (1 mmol/L), medium (6 mmol/L) or high (16.7 mmol/L) glucose, or low glucose + adrenaline (10 μmol/L), to trigger differential secretion from alpha, beta and delta cells. Proglucagon-derived peptides and PPY showed higher secretion in the low glucose + adrenaline condition, whereas proinsulin-derived peptides, IAPP and SST exhibited highest secretion in high glucose (Figure 6). Active GLP-1 and peptides from proenkephalin-B and urocortin 3 were not detectable in islet supernatants.

■ DISCUSSION

This study presents a detailed analysis of the human and mouse islet peptidome with a focus on peptides derived from secretory granules, together with corresponding measurements in murine obesity and human T2DM. Mostly we applied a semiquantitative approach that enabled comparisons between the same peptide in different specimens, but did not generate exact concentrations. For glucagon and GLP-1, the additional use of calibration standards allowed assessments of actual peptide contents. We are not able to draw conclusions about the presence or absence of peptides that were undetectable using this methodology and for which we did not include individual peptide standards, because different peptides are not uniform in their behavior during the extraction steps and LC-MS analysis.

In addition to peptides from proinsulin, proglucagon, and prosomatostatin, we identified some rarer peptides originating from VGF in human islets, and from PYY, prourocortin-3 and proenkephalin-B in mouse islets. Proenkephalin-B is primarily expressed in the brain[34] where it is processed to multiple

https://doi.org/10.1021/acs.jproteome.1c00463
J. Proteome Res. 2021, 20, 4507–4517

opioid receptor agonists such as α-neoendorphin and rimorphin,[32,33] but has not been described previously in islets. As opioid receptors were not detected in human or mouse islets by RNA sequencing,[10,11] it seems unlikely that proenkephalin-products are a key player in intraislet cross talk. Urocortin-3 was described previously in pancreatic beta cells[35] and confirmed here by LC-MS.

Mirroring reports that *Gip* mRNA is not detectable in islets[10,11] and absence of islet Cre-reporter activity in GIP-Cre mice,[36] we could not detect proGIP derived peptides in mouse or human islets despite using targeted product ion scans to monitor for 3 individual proGIP peptides that are readily detectable in duodenum.[25] We conclude it is highly unlikely that human or mouse islets produce GIP.

Estimates for islet glucagon content measured by LC-MS were similar to those measured previously by ELISA.[37−39] Active GLP-1(7−36 amide and 7−37) was detectable by LC-MS in mouse and human islets, but at 400 to 1000-fold lower levels than glucagon. Very low levels and secretion of active GLP-1 relative to glucagon were previously reported in mouse islets,[4,16] but other studies using antibody-based approaches that are less able to discriminate GLP-1(7−37/36amide) from GLP-1(1−37/36amide) have calculated islet GLP-1 production to be much higher.[2,4,40] Our LC-MS approach readily detected N-terminally extended GLP-1(1−37/1−36amide) in human and mouse islets, with peak areas ∼10-fold higher than corresponding GLP-1(7−37/36amide) forms. Despite the relatively low production of active GLP-1 by pancreatic alpha cells, a number of studies have concluded that intraislet production of proglucagon-derived peptides influences insulin secretion through beta cell GLP1R.[4,6,16,40] The difference in potency between GLP-1(7−36amide) and glucagon on GLP1R has been estimated at 50 to 400-fold,[16,19,41,42] so our finding of 300−1000 times more glucagon than active GLP-1 in islets would favor glucagon as the local dominant agonist on beta cell GLP1R. All detectable proglucagon fragments were released in parallel in secretion experiments, exhibiting lower release at high glucose, suggesting that signaling from alpha to beta cells via GLP1R might diminish in importance following a simple rise in plasma glucose concentration. However, GLP1R-dependent cross-talk between alpha and beta cells might be higher in situations when alpha cells are simultaneously activated, such as in the postprandial state when they are directly stimulated by amino acids and/or gut-derived GIP, as also suggested by a recent study.[43]

In islets from DIO mice we observed an increase in the abundance of proIAPP, proinsulin-1 and -2 derived peptides, consistent with reports of β-cell hyperplasia in similar models.[44−46] However, as we deliberately matched islet sizes between the control and DIO group, our analysis would have excluded larger islets with beta cell hyperplasia, reducing our ability to quantify differences in islet insulin content. No other significant peptidomic changes were seen in DIO mouse islets, supporting an RNA-sequencing based approach which similarly did not find major transcriptomic differences in alpha cells between DIO and lean mice.[47]

To our surprise, we detected only limited peptidomic changes in islets from diabetic human donors. However, as islets had a mean culture time of 43 h in 5.5 mmol/L glucose and cold ischemia time of 14 h prior to freezing, this may have been sufficient to reverse effects of hyperglycemic stress encountered in vivo. As we only analyzed samples from 9 control and 7 diabetic donors, across a spectrum of diabetes severity, this study is not powered to correlate peptidomic changes with patient phenotypes, or identify changes in specific subgroups. Overall, diabetic islets exhibited a global reduction in peptides from proinsulin and IAPP and a corresponding increase in peptides from proglucagon, with no evident change in SST. This mirrors results from a previous study measuring insulin, glucagon, and SST contents in pancreatic tissue from T2DM and nondiabetic donors, which reported lower insulin content per gram of tissue in the diabetic group and not significantly altered glucagon or SST, although reductions in the total pancreatic contents of insulin and SST content were evident when the smaller overall weight of T2DM pancreas was taken into account.[48] Contrary to our expectations, based on previous reports that T2DM is associated with increased circulating proinsulin levels[49,50] and increased islet GLP-1 production,[1] we found no evidence of substantially altered proinsulin or proglucagon processing in T2DM islets. Some studies have suggested that beta cells dedifferentiate in diabetes, taking on partial alpha cell phenotypes and expressing *GCG* together with *PC1/3*.[22,51] In theory, this could generate cells capable of producing GLP-1(7−36amide) from proglucagon, potentially explaining previous reports of increased islet GLP-1 generation in diabetes. Although manual quantification of our LC-MS data revealed a significant increase in active GLP-1 in diabetic islets, this was mirrored by an increase in glucagon with no change in the glucagon:GLP-1 ratio, arguing against a major alteration in proglucagon processing.

Despite detecting no shift in insulin processing in diabetic islets, in plasma from a separate group of diabetic volunteers, we noticed an increase in the ratio of proinsulin and des-31,32 proinsulin to mature insulin, compared with healthy controls, supporting a number of previous studies employing immunoassays.[49,50] Proinsulin and des-31,32 proinsulin increased proportionally with insulin following glucose ingestion, suggesting that both peptides are released in parallel in vivo. The finding of increased plasma proinsulin and des-31,32 proinsulin in plasma from the diabetic group, without corresponding increases in partially processed insulin fragments in the islets, is compatible with the idea that islets in type 2 diabetes release more immature vesicles containing incompletely processed proinsulin.

In conclusion, this analysis has identified the spectrum of peptides produced by human and mouse islets in health and metabolic disease, including post-translational modifications and exact peptide sequences. While we could detect active GLP-1 in both human and mouse islets, levels were 100−1000 fold lower than glucagon, suggesting that the activity of glucagon on beta cell GLP1R would overcome any effect of local GLP-1 production. Locally released GLP1R agonist peptides could contribute to postprandial insulin release, particularly when alpha cells are stimulated by elevated levels of intestinal GIP and amino acids.

■ ASSOCIATED CONTENT

Supporting Information

The Supporting Information is available free of charge at https://pubs.acs.org/doi/10.1021/acs.jproteome.1c00463.

Table S1: Precursor ions selected for product ion scans; Table S2: Product, precursor, collision energies, and dwell times for peptides monitored on triple quadrupole mass spectrometer; Figure S1: Nonclassical islet peptides detected in mouse and human islets; Figure

https://doi.org/10.1021/acs.jproteome.1c00463
J. Proteome Res. 2021, 20, 4507−4517

S2: Standard curves for GLP-1(7−36amide) and glucagon; Figure S3: GLP-1(7−36amide) in mouse islets; Figure S4: Searching for the N-terminal propeptide of proGip (Gip 22−43) in mouse islets; Figure S5: Searching for GIP (1−30) in mouse islets; Figure S6: Searching for GIP (1−42) in mouse islets; Figure S7: Peptidomic comparison of islets from DIO mice and humans with type 2 diabetes (PDF)

Table 3: Peptidomics of murine alpha, beta, and delta cells (XLSX)

Table 4: Peptidomic differences between islets from mice fed on chow or high fat diet (XLSX)

Table 5: Peptidomic differences between nondiabetic control and type 2 diabetic donor islets (XLSX)

AUTHOR INFORMATION

Corresponding Authors

Frank Reimann − *University of Cambridge Metabolic Research Laboratories, WT-MRC Institute of Metabolic Science, Addenbrooke's Hospital, Cambridge CB2 0QQ, U.K.*; Phone: 01223 746796; Email: fr222@cam.ac.uk

Fiona M. Gribble − *University of Cambridge Metabolic Research Laboratories, WT-MRC Institute of Metabolic Science, Addenbrooke's Hospital, Cambridge CB2 0QQ, U.K.*; orcid.org/0000-0002-4232-2898; Phone: 01223 746796; Email: fmg23@cam.ac.uk

Authors

Sam G. Galvin − *University of Cambridge Metabolic Research Laboratories, WT-MRC Institute of Metabolic Science, Addenbrooke's Hospital, Cambridge CB2 0QQ, U.K.*

Richard G. Kay − *University of Cambridge Metabolic Research Laboratories, WT-MRC Institute of Metabolic Science, Addenbrooke's Hospital, Cambridge CB2 0QQ, U.K.*

Rachel Foreman − *University of Cambridge Metabolic Research Laboratories, WT-MRC Institute of Metabolic Science, Addenbrooke's Hospital, Cambridge CB2 0QQ, U.K.*

Pierre Larraufie − *University of Cambridge Metabolic Research Laboratories, WT-MRC Institute of Metabolic Science, Addenbrooke's Hospital, Cambridge CB2 0QQ, U.K.*

Claire L. Meek − *University of Cambridge Metabolic Research Laboratories, WT-MRC Institute of Metabolic Science, Addenbrooke's Hospital, Cambridge CB2 0QQ, U.K.*

Emma Biggs − *University of Cambridge Metabolic Research Laboratories, WT-MRC Institute of Metabolic Science, Addenbrooke's Hospital, Cambridge CB2 0QQ, U.K.*

Peter Ravn − *Research and Early Development Cardiovascular, Renal and Metabolism (CVRM), BioPharmaceuticals R&D, AstraZeneca Ltd., Cambridge CB21 6GH, U.K.*

Lutz Jermutus − *Research and Early Development Cardiovascular, Renal and Metabolism (CVRM), BioPharmaceuticals R&D, AstraZeneca Ltd., Cambridge CB21 6GH, U.K.*

Complete contact information is available at: https://pubs.acs.org/10.1021/acs.jproteome.1c00463

Author Contributions

All authors contributed to study design, manuscript preparation and approval of the final manuscript version. SGG generated and analyzed most of the data. RF analyzed human plasma samples. RGK and PL optimized and supervised the LC-MS/MS data collection. CLM ran the study producing human plasma samples.

Funding

SGG is supported by an iCASE studentship from the BBSRC and AstraZeneca. RF is supported by an iCASE studentship from the BBSRC and LGC. Research in the laboratories of FMG and FR is supported by MRC (MRC_MC_UU_12012/3) and Wellcome Trust (220271/Z/20/Z). CLM is supported by the Diabetes UK Harry Keen Intermediate Clinical Fellowship (DUK-HKF 17/0005712) and the European Foundation for the Study of Diabetes − Novo Nordisk Foundation Future Leaders' Award (NNF19SA058974). Research was supported by the NIHR Cambridge BRC and the NIHR/Wellcome Trust clinical research facility. The views expressed are those of the author(s) and not necessarily those of the NIHR or the Department of Health and Social Care. The MS instrument was funded by the MRC "Enhancing UK clinical research" grant (MR/M009041/1). Support for the core facilities at the Metabolic Research Laboratories was provided by the Medical Research Council (MRC_MC_UU_12012/5) and Wellcome Trust (100574/Z/12/Z).

Notes

The authors declare the following competing financial interest(s): This work was supported by funding from Wellcome, MRC, BBSRC, NIHR and AstraZeneca. PR and LJ are employees of AstraZeneca.

The mass spectrometry proteomics data have been deposited to the ProteomeXchange Consortium via the PRIDE partner repository with the data set identifier PXD026095 and 10.6019/PXD026095.

ACKNOWLEDGMENTS

We would like to extend out thanks to the flow cytometry group at the Cambridge Institute for Metabolic Research for their help in performing the cell sorting experiments, and Dr. James Howard (LGC Ltd., Fordham) for the donation of the glucagon internal standard. We thank the IsletCore (University of Alberta, Canada) for providing human pancreatic islets.

ABBREVIATIONS

ACN, acetonitrile; DIO, diet-induced obese; GIP, glucose-dependent insulinotropic peptide; GLP-1, glucagon like peptide-1; GLP1R, GLP-1 receptor; GuHCl, guanidine hydrochloride; HFD, high fat diet; IAPP, islet amyloid polypeptide; LC-MS, liquid chromatography coupled to mass spectrometry; PC, prohormone convertase; PPY, pancreatic polypeptide; PYY, peptide YY; SST-14, somatostatin-14.

REFERENCES

(1) Marchetti, P.; Lupi, R.; Bugliani, M.; Kirkpatrick, C. L.; Sebastiani, G.; Grieco, F. A.; Del Guerra, S.; D'Aleo, V.; Piro, S.; Marselli, L.; Boggi, U.; Filipponi, F.; Tinti, L.; Salvini, L.; Wollheim, C. B.; Purrello, F.; Dotta, F. A local glucagon-like peptide 1 (GLP-1) system in human pancreatic islets. *Diabetologia* **2012**, *55* (12), 3262−72.

(2) O'Malley, T. J.; Fava, G. E.; Zhang, Y.; Fonseca, V. A.; Wu, H. Progressive change of intra-islet GLP-1 production during diabetes development. *Diabetes/Metab. Res. Rev.* **2014**, *30* (8), 661−8.

(3) Song, Y.; Koehler, J. A.; Baggio, L. L.; Powers, A. C.; Sandoval, D. A.; Drucker, D. J. Gut-Proglucagon-Derived Peptides Are Essential for Regulating Glucose Homeostasis in Mice. *Cell Metab.* **2019**, *30* (5), 976−986.

(4) Traub, S.; Meier, D. T.; Schulze, F.; Dror, E.; Nordmann, T. M.; Goetz, N.; Koch, N.; Dalmas, E.; Stawiski, M.; Makshana, V.; Thorel, F.; Herrera, P. L.; Böni-Schnetzler, M.; Donath, M. Y. Pancreatic α Cell-Derived Glucagon-Related Peptides Are Required for β Cell Adaptation and Glucose Homeostasis. *Cell Rep.* **2017**, *18* (13), 3192−3203.
(5) Whalley, N. M.; Pritchard, L. E.; Smith, D. M.; White, A. Processing of proglucagon to GLP-1 in pancreatic α-cells: is this a paracrine mechanism enabling GLP-1 to act on β-cells? *J. Endocrinol.* **2011**, *211* (1), 99−106.
(6) Hansen, A. M.; Bödvarsdottir, T. B.; Nordestgaard, D. N.; Heller, R. S.; Gotfredsen, C. F.; Maedler, K.; Fels, J. J.; Holst, J. J.; Karlsen, A. E. Upregulation of alpha cell glucagon-like peptide 1 (GLP-1) in Psammomys obesus–an adaptive response to hyperglycaemia? *Diabetologia* **2011**, *54* (6), 1379−87.
(7) Fujita, Y.; Wideman, R. D.; Asadi, A.; Yang, G. K.; Baker, R.; Webber, T.; Zhang, T.; Wang, R.; Ao, Z.; Warnock, G. L.; Kwok, Y. N.; Kieffer, T. J. Glucose-dependent insulinotropic polypeptide is expressed in pancreatic islet alpha-cells and promotes insulin secretion. *Gastroenterology* **2010**, *138* (5), 1966−75.
(8) Alumets, J.; Håkanson, R.; O'Dorisio, T.; Sjölund, K.; Sundler, F. Is GIP a glucagon cell constituent? *Histochemistry* **1978**, *58* (4), 253−7.
(9) Mastracci, T. L.; Sussel, L. The Endocrine Pancreas: insights into development, differentiation and diabetes. *Wiley Interdiscip Rev. Membr. Transp Signal* **2012**, *1* (5), 609−628.
(10) Baron, M.; Veres, A.; Wolock, S. L.; Faust, A. L.; Gaujoux, R.; Vetere, A.; Ryu, J. H.; Wagner, B. K.; Shen-Orr, S. S.; Klein, A. M.; Melton, D. A.; Yanai, I. A Single-Cell Transcriptomic Map of the Human and Mouse Pancreas Reveals Inter- and Intra-cell Population Structure. *Cell Syst* **2016**, *3* (4), 346−360.
(11) Adriaenssens, A. E.; Svendsen, B.; Lam, B. Y.; Yeo, G. S.; Holst, J. J.; Reimann, F.; Gribble, F. M. Transcriptomic profiling of pancreatic alpha, beta and delta cell populations identifies delta cells as a principal target for ghrelin in mouse islets. *Diabetologia* **2016**, *59* (10), 2156−65.
(12) Fujita, Y.; Yanagimachi, T.; Takeda, Y.; Honjo, J.; Takiyama, Y.; Abiko, A.; Makino, Y.; Haneda, M. Alternative form of glucose-dependent insulinotropic polypepide and its physiology. *J. Diabetes Invest.* **2016**, *7*, 33−37.
(13) Larsson, L. I.; Moody, A. J. Glicentin and gastric inhibitory polypeptide immunoreactivity in endocrine cells of the gut and pancreas. *J. Histochem. Cytochem.* **1980**, *28* (9), 925−33.
(14) Buchan, A. M.; Ingman-Baker, J.; Levy, J.; Brown, J. C. A comparison of the ability of serum and monoclonal antibodies to gastric inhibitory polypeptide to detect immunoreactive cells in the gastroenteropancreatic system of mammals and reptiles. *Histochemistry* **1982**, *76* (3), 341−9.
(15) Orskov, C.; Rabenhøj, L.; Wettergren, A.; Kofod, H.; Holst, J. J. Tissue and plasma concentrations of amidated and glycine-extended glucagon-like peptide I in humans. *Diabetes* **1994**, *43* (4), 535−539.
(16) Svendsen, B.; Larsen, O.; Gabe, M. B. N.; Christiansen, C. B.; Rosenkilde, M. M.; Drucker, D. J.; Holst, J. J. Insulin Secretion Depends on Intra-islet Glucagon Signaling. *Cell Rep.* **2018**, *25* (5), 1127−1134.
(17) Capozzi, M. E.; Svendsen, B.; Encisco, S. E.; Lewandowski, S. L.; Martin, M. D.; Lin, H.; Jaffe, J. L.; Coch, R. W.; Haldeman, J. M.; MacDonald, P. E.; Merrins, M. J.; D'Alessio, D. A.; Campbell, J. E. β Cell tone is defined by proglucagon peptides through cAMP signaling. *JCI Insight* **2019**, DOI: 10.1172/jci.insight.126742.
(18) Chepurny, O. G.; Matsoukas, M. T.; Liapakis, G.; Leech, C. A.; Milliken, B. T.; Doyle, R. P.; Holz, G. G. Nonconventional glucagon and GLP-1 receptor agonist and antagonist interplay at the GLP-1 receptor revealed in high-throughput FRET assays for cAMP. *J. Biol. Chem.* **2019**, *294* (10), 3514−3531.
(19) Day, J. W.; Li, P.; Patterson, J. T.; Chabenne, J.; Chabenne, M. D.; Gelfanov, V. M.; Dimarchi, R. D. Charge inversion at position 68 of the glucagon and glucagon-like peptide-1 receptors supports selectivity in hormone action. *J. Pept. Sci.* **2011**, *17* (3), 218−25.
(20) Taylor, S. W.; Nikoulina, S. E.; Andon, N. L.; Lowe, C. Peptidomic profiling of secreted products from pancreatic islet culture results in a higher yield of full-length peptide hormones than found using cell lysis procedures. *J. Proteome Res.* **2013**, *12* (8), 3610−9.
(21) Linnemann, A. K.; Baan, M.; Davis, D. B. Pancreatic β-cell proliferation in obesity. *Adv. Nutr.* **2014**, *5* (3), 278−88.
(22) Cinti, F.; Bouchi, R.; Kim-Muller, J. Y.; Ohmura, Y.; Sandoval, P. R.; Masini, M.; Marselli, L.; Suleiman, M.; Ratner, L. E.; Marchetti, P.; Accili, D. Evidence of β-Cell Dedifferentiation in Human Type 2 Diabetes. *J. Clin. Endocrinol. Metab.* **2016**, *101* (3), 1044−54.
(23) Talchai, C.; Xuan, S.; Lin, H. V.; Sussel, L.; Accili, D. Pancreatic β cell dedifferentiation as a mechanism of diabetic β cell failure. *Cell* **2012**, *150* (6), 1223−34.
(24) Wang, Z.; York, N. W.; Nichols, C. G.; Remedi, M. S. Pancreatic β cell dedifferentiation in diabetes and redifferentiation following insulin therapy. *Cell Metab.* **2014**, *19* (5), 872−82.
(25) Galvin, S. G.; Larraufie, P.; Kay, R. G.; Pitt, H.; Bernard, E.; McGavigan, A. K.; Brandt, H.; Hood, J.; Sheldrake, L.; Conder, S.; Atherton-Kemp, D.; Lu, V. B.; O'Flaherty, E. A. A.; Roberts, G. P.; Ämmälä, C.; Jermutus, L.; Baker, D.; Gribble, F. M.; Reimann, F. Peptidomics of enteroendocrine cells and characterisation of potential effects of a novel preprogastrin derived-peptide on glucose tolerance in lean mice. *Peptides* **2021**, *140*, 170532.
(26) Church, D.; Cardoso, L.; Kay, R. G.; Williams, C. L.; Freudenthal, B.; Clarke, C.; Harris, J.; Moorthy, M.; Karra, E.; Gribble, F. M.; Reimann, F.; Burling, K.; Williams, A. J. K.; Munir, A.; Jones, T. H.; Führer, D.; Moeller, L. C.; Cohen, M.; Khoo, B.; Halsall, D.; Semple, R. K. Assessment and Management of Anti-Insulin Autoantibodies in Varying Presentations of Insulin Autoimmune Syndrome. *J. Clin. Endocrinol. Metab.* **2018**, *103* (10), 3845−3855.
(27) Goldspink, D. A.; Lu, V. B.; Miedzybrodzka, E. L.; Smith, C. A.; Foreman, R. E.; Billing, L. J.; Kay, R. G.; Reimann, F.; Gribble, F. M. Labeling and Characterization of Human GLP-1-Secreting L-cells in Primary Ileal Organoid Culture. *Cell Rep.* **2020**, *31* (13), 107833.
(28) Biggs, E. K.; Liang, L.; Naylor, J.; Madalli, S.; Collier, R.; Coghlan, M. P.; Baker, D. J.; Hornigold, D. C.; Ravn, P.; Reimann, F.; Gribble, F. M. Development and characterisation of a novel glucagon like peptide-1 receptor antibody. *Diabetologia* **2018**, *61* (3), 711−721.
(29) Kay, R. G.; Galvin, S.; Larraufie, P.; Reimann, F.; Gribble, F. M. Liquid chromatography/mass spectrometry based detection and semi-quantitative analysis of INSL5 in human and murine tissues. *Rapid Commun. Mass Spectrom.* **2017**, *31* (23), 1963−1973.
(30) Meek, C. L.; Lewis, H. B.; Vergese, B.; Park, A.; Reimann, F.; Gribble, F. The effect of encapsulated glutamine on gut peptide secretion in human volunteers. *Peptides* **2016**, *77*, 38−46.
(31) Kay, R. G.; Foreman, R. E.; Roberts, G. P.; Hardwick, R.; Reimann, F.; Gribble, F. M. Mass spectrometric characterisation of the circulating peptidome following oral glucose ingestion in control and gastrectomised patients. *Rapid Commun. Mass Spectrom.* **2020**, *34* (18), No. e8849.
(32) Li, S.; Zhu, J.; Chen, C.; Chen, Y. W.; Deriel, J. K.; Ashby, B.; Liu-Chen, L. Y. Molecular cloning and expression of a rat kappa opioid receptor. *Biochem. J.* **1993**, *295* (3), 629−633.
(33) Zhu, J.; Chen, C.; Xue, J. C.; Kunapuli, S.; DeRiel, J. K.; Liu-Chen, L. Y. Cloning of a human kappa opioid receptor from the brain. *Life Sci.* **1995**, *56* (9), PL201−7.
(34) The Human Protein Atlas: PDYN expression. https://www.proteinatlas.org/ENSG00000101327-PDYN/tissue accessed on 19/08/2021.
(35) Li, C.; Chen, P.; Vaughan, J.; Blount, A.; Chen, A.; Jamieson, P. M.; Rivier, J.; Smith, M. S.; Vale, W. Urocortin III is expressed in pancreatic beta-cells and stimulates insulin and glucagon secretion. *Endocrinology* **2003**, *144* (7), 3216−24.
(36) Svendsen, B.; Pais, R.; Engelstoft, M. S.; Milev, N. B.; Richards, P.; Christiansen, C. B.; Egerod, K. L.; Jensen, S. M.; Habib, A. M.; Gribble, F. M.; Schwartz, T. W.; Reimann, F.; Holst, J. J. GLP1- and GIP-producing cells rarely overlap and differ by bombesin receptor-2 expression and responsiveness. *J. Endocrinol.* **2016**, *228* (1), 39−48.

(37) Collins, S. C.; Salehi, A.; Eliasson, L.; Olofsson, C. S.; Rorsman, P. Long-term exposure of mouse pancreatic islets to oleate or palmitate results in reduced glucose-induced somatostatin and oversecretion of glucagon. *Diabetologia* **2008**, *51* (9), 1689−93.
(38) Guillo, C.; Roper, M. G. Two-color electrophoretic immunoassay for simultaneous measurement of insulin and glucagon content in islets of Langerhans. *Electrophoresis* **2008**, *29* (2), 410−6.
(39) Henquin, J. C. The challenge of correctly reporting hormones content and secretion in isolated human islets. *Mol. Metab.* **2019**, *30*, 230−239.
(40) Campbell, S. A.; Golec, D. P.; Hubert, M.; Johnson, J.; Salamon, N.; Barr, A.; MacDonald, P. E.; Philippaert, K.; Light, P. E. Human islets contain a subpopulation of glucagon-like peptide-1 secreting α cells that is increased in type 2 diabetes. *Mol. Metab.* **2020**, *39*, 101014.
(41) Chepurny, O. G.; Matsuokas, M. T.; Liapakis, G.; Leech, C. A.; Milliken, B. T.; Doyle, R. P.; Holz, G. G. Correction: Nonconventional glucagon and GLP-1 receptor agonist and antagonist interplay at the GLP-1 receptor revealed in high-throughput FRET assays for cAMP. *J. Biol. Chem.* **2019**, *294* (22), 8714.
(42) Runge, S.; Wulff, B. S.; Madsen, K.; Bräuner-Osborne, H.; Knudsen, L. B. Different domains of the glucagon and glucagon-like peptide-1 receptors provide the critical determinants of ligand selectivity. *Br. J. Pharmacol.* **2003**, *138* (5), 787−94.
(43) El, K.; Gray, S. M.; Capozzi, M. E.; Knuth, E. R.; Jin, E.; Svendsen, B.; Clifford, A.; Brown, J. L.; Encisco, S. E.; Chazotte, B. M.; Sloop, K. W.; Nunez, D. J.; Merrins, M. J.; D'Alessio, D. A.; Campbell, J. E. GIP mediates the incretin effect and glucose tolerance by dual actions on α cells and β cells. *Sci. Adv.* **2021**, *7* (11), eabf1948.
(44) Dor, Y.; Brown, J.; Martinez, O. I.; Melton, D. A. Adult pancreatic beta-cells are formed by self-duplication rather than stem-cell differentiation. *Nature* **2004**, *429* (6987), 41−6.
(45) Georgia, S.; Bhushan, A. Beta cell replication is the primary mechanism for maintaining postnatal beta cell mass. *J. Clin. Invest.* **2004**, *114* (7), 963−8.
(46) Burke, S. J.; Batdorf, H. M.; Burk, D. H.; Noland, R. C.; Eder, A. E.; Boulos, M. S.; Karlstad, M. D.; Collier, J. J. db/db Mice Exhibit Features of Human Type 2 Diabetes That Are Not Present in Weight-Matched C57BL/6J Mice Fed a Western Diet. *J. Diabetes Res.* **2017**, *2017*, 8503754.
(47) Dusaulcy, R.; Handgraaf, S.; Visentin, F.; Howald, C.; Dermitzakis, E. T.; Philippe, J.; Gosmain, Y. High-fat diet impacts more changes in beta-cell compared to alpha-cell transcriptome. *PLoS One* **2019**, *14* (3), No. e0213299.
(48) Henquin, J. C.; Ibrahim, M. M.; Rahier, J. Insulin, glucagon and somatostatin stores in the pancreas of subjects with type-2 diabetes and their lean and obese non-diabetic controls. *Sci. Rep.* **2017**, *7* (1), 11015.
(49) Clark, P. M.; Levy, J. C.; Cox, L.; Burnett, M.; Turner, R. C.; Hales, C. N. Immunoradiometric assay of insulin, intact proinsulin and 32−33 split proinsulin and radioimmunoassay of insulin in diet-treated type 2 (non-insulin-dependent) diabetic subjects. *Diabetologia* **1992**, *35* (5), 469−74.
(50) Kahn, S. E.; Halban, P. A. Release of incompletely processed proinsulin is the cause of the disproportionate proinsulinemia of NIDDM. *Diabetes* **1997**, *46* (11), 1725−1732.
(51) Mezza, T.; Cinti, F.; Cefalo, C. M. A.; Pontecorvi, A.; Kulkarni, R. N.; Giaccari, A. β-Cell Fate in Human Insulin Resistance and Type 2 Diabetes: A Perspective on Islet Plasticity. *Diabetes* **2019**, *68* (6), 1121−1129.

https://doi.org/10.1021/acs.jproteome.1c00463
J. Proteome Res. 2021, 20, 4507−4517

APPENDIX 3

EXTRACTS FROM PUBLISHED RESEARCH PAPERS

1. **<u>Footnote 11:</u> Factors That Can Influence Animal Research, David G Baker DVM, PhD, MS, MPA, DACLAMa and Neil S. Lipman, VMD, DACLAM, Laboratory Animal Medicine, Third Edv (referring to Dallman et al., 1999; Raff et al., 2011; Rasmussen et al., 2009).**

   "laboratories have described construction-associated research effects caused by vibra-tion, noise, or both, including alteration of energy bal-ance, i.e., decreased food consumption and body weight; increased stillbirths and pup mortality; and a marked stress response resulting in elevation of plasma ACTH, corticosterone, and aldosterone"

2. **<u>Footnote 15</u>: Characterization of Train-Induced Vibration and its Effect on Fecal Corticosterone Metabolites in Mice Nicholas A Atanasov, Jennifer L Sargent, John P Parmigiani,1 Rupert Palme,3 and Helen E Diggs, Journal of the American Association for Laboratory Animal Science Vol 54, No 6 November 2015 Pages 737–744**

   "Analysis of the fecal samples revealed that vibrations similar to those produced by a passing train can increase the levels of fecal corticosterone metabolites in female mice. These increases warrant attention to the effects of vibration on mice and, consequently, on reproduction and experimental outcomes";

   "The preliminary data we gathered indicate that vibrations from passing trains create significant increases in the FCM levels of female mice. Fluctuations in stress may be disruptive to research studies and breeding colonies. Elevated corticosterone levels can induce a variety of negative effects in rodents"

3. **<u>Footnotes 16 and 17</u>: Construction Noise Decreases Reproductive Efficiency in Mice Skye Rasmussen, Gary Glickman, Rada Norinsky, Fred W Quimby, and Ravi J Tolwani Journal of the American Association for Laboratory Animal Science Vol 48, No 4 July 2009 Pages 363–370**

   "groups of mice with litters were exposed to noise at 70, 80, or 90 dBA for 1 h daily during the first week after parturition. Litter size, birth weight, incidence of stillborn

pups, and rate of neonatal weight gain were analyzed. Noise decreased reproductive efficiency by decreasing live birth rates and increasing the number of stillborn pups."

4. **<u>Footnote 18</u>: Comparative Vibration Levels Perceived Among Species in a Laboratory Animal Facility John N Norton, Will L Kinard, and Randall P Reynolds, Journal of the American Association for Laboratory Animal Science Vol 50, No 5 September 2011 Pages 653–659**

   "Noise and vibration in a laboratory animal facility are cited as factors that can induce stress in animals and alter research results…. *Vibration and noise have long been known to have potentially detrimental effects in rodents, but the relative contribution of each to these adverse effects is unknown.*"

5. **<u>Footnote 19</u>: Are Investigators Aware of Environmental Noise in Animal Facilities and That This Noise May Affect Experimental Data? Ann L Baldwin, Gary E Schwartz,2 and Douglas H Hopp, Journal of the American Association for Laboratory Animal Science Vol 46, No 1 January 2007 Pages 45–51**

   "because faculty are the least aware of noise as a potential problem but are primarily responsible for designing experiments, research involving animals may be confounded by noise as an unknown variable. This effect may lead to unnecessary numbers of animals being required to achieve statistical significance and possibly to erroneous interpretation of results".

APPENDIX 4
CORRESPONDENCE FROM CURRENT ACAMEDIC USERS OF THE AMB

Dear Keith,

We are performing doppler measurements of cerebral blood flow during stroke in mice. These measurements are very fine and sensitive and could very well be influenced by vibrations.

Noise will most likely not be a problem.

Hope this helps. Happy to provide more detail if necessary.

Best wishes,
Thomas

Thomas Krieg
Associate Professor/Honorary Consultant Physician
Department of Medicine
University of Cambridge
Addenbrooke's Hospital
Cambridge, CB2 0QQ
www.krieglab.com

Dear Keith

We have significant concerns that any increase in noise and vibration could have on our animals/experiments housed in the AMB.

We conduct animal experiments to understand the mechanisms underlying heart attacks and to develop new treatments for patients. These experiments require the generation and use of mice that mimic the human disease, specifically they get atherosclerotic plaques in their large arteries when fed a high fat diet. These mice and other genetically modified mice we use generally breed poorly, and any increased disturbance reduces their breeding and litter sizes, and also results in the mother eating the litters. Successful experiments also require long term fat feeding (>6m), and increased disturbance reduces the extent of atherosclerosis they develop. In short, any increased disturbance will delay experiments, cause established experiments to be curtailed early thus losing data, and increased number of mice (and therefore costs) that need to be used.

Regards

Martin

Professor Martin Bennett
BHF Professor of Cardiovascular Sciences
mrb24@medschl.cam.ac.uk

Dear Keith,

Thanks for your message.

I am concerned that noise and vibration will negatively impact on mouse reproductive efficiency. Our research at the Department of Obs & Gynae depends on mice mating and reproducing. According to research from the Rockefeller University in 2009 (one reference provided below), it is to be expected that reproductive efficiency will be decreased

From Rasmussen et al, 2009: "Noise decreased reproductive efficiency by decreasing live birth rates and increasing the number of stillborn pups"

Should this happen, it might significantly slow down or even stop much of our research

Thanks and best wishes
Francesco

Professor Francesco Colucci, MD PhD
Wellcome Investigator | Clinical School University of Cambridge
Fellow, Director of Studies in Medicine and Graduate Tutor | King's College
https://twitter.com/DrFran_Colucci
http://orcid.org/0000-0001-5193-6376

Dear Keith

Our research relies on us being able to breed mice that are able to accept human cancers so that we can perform studies to analyse responses to new drugs. The mice are especially sensitive to any environmental disturbances whereby they cease to breed. We know this as colleagues in both Vienna and Gothenburg conducting similar research have had to suspend their animal work due to building projects that created vibrations. This has had very obvious implications towards their research whereby they have been unable to achieve their objectives - these are time-sensitive as projects receive funding that generally lasts for 1-3 years and a building project can significantly impact progress meaning that little is achieved with the research funding awarded. This not only impacts our ability to make progress in our understanding of cancer, but also has a knock-on effect on the careers of the scientists and technicians we employ, who are all largely on fixed-term contracts aligning with the funding period.

BW
Suzanne

Professor Suzanne D Turner
Division of Cellular and Molecular Pathology
Lab Block Level 3
Box 231
Addenbrooke's Hospital
Cambridge
CB2 0QQ